DEGRADATION OF BIFACIAL & MONOFACIAL, DOUBLE GLASS & GLASS-BACKSHEET, PHOTOVOLTAIC MODULES WITH MULTIPLE PACKAGING COMBINATIONS

by

JIQI LIU

Submitted in partial fulfillment of the requirements

For the degree of Doctor of Philosophy

Thesis Adviser: Dr. Roger H. French

Department of Materials Science and Engineering

CASE WESTERN RESERVE UNIVERSITY

August, 2022

Degradation of Bifacial & Monofacial, Double Glass & Glass-backsheet, Photovoltaic Modules with Multiple Packaging Combinations

We hereby approve the thesis[1] of

JIQI LIU

for the degree of

Doctor of Philosophy

Dr. Roger H. French

Committee Chair, Advisor — 05/26/2022
Department of Materials Science and Engineering

Dr. Alp Sehirlioglu

Committee Member — 05/26/2022
Department of Materials Science and Engineering

Dr. Laura S. Bruckman

Committee Member — 05/26/2022
Department of Materials Science and Engineering

Dr. Yinghui Wu

Committee Member — 05/26/2022
Computer & Data Science Department

Dr. Jennifer L. Braid

Committee Member — 05/26/2022
Department of Materials Science and Engineering

Dr. Xuanji Yu

Committee Member — 05/26/2022
Department of Materials Science and Engineering

[1] We certify that written approval has been obtained for any proprietary material contained therein.

Table of Contents

List of Tables v

List of Figures viii

Glossary xiv

Acknowledgements xv

Abstract xvi

Chapter 1. Introduction 1

Chapter 2. Literature Review 4

Packaging Strategies of PV Modules 4

Outdoor PV Reliability Study with Timeseries Electrical Data 16

Machine Learning Methods Applied in PV Reliability Study 21

Correlate Lab Reliability Results to Real World Performance 26

Chapter 3. Experimental and Analytical Methods 30

Fabrication of Minimodules 31

Indoor Accelerated Exposures and Stepwise Evaluations 36

Outdoor Real-world Exposures and Timeseries Evaluations 43

Chapter 4. Indoor, Stepwise, Accelerated Exposure Study of PERC Module Variants 45

Introduction 46

Methods 49

Results 52

Discussion 61

Conclusions 71

Chapter 5. Outdoor Exposure Study of Module Variants using Timeseries Data 73

Introduction 74

Methods 76

Results 80

Discussion 87

Conclusions 99

Chapter 6. Indoor/outdoor Cross-correlation for PV Degradation Studies 101

Introduction 102

Methods 104

Results 110

Discussion 113

Conclusions 119

Chapter 7. Regression CNN & RNN of Degradation of Power and Series Resistance 121

Introduction 122

Methods 125

Results 133

Discussion 142

Conclusions 150

Chapter 8. Conclusion 152

Appendix A. Preparation of this document 156

Appendix. Complete Bibliography 157

List of Tables

3.1 Detailed quantities and specifications of the minimodules that were fabricated and tested. mDH represents modified damp heat, and mDH+FSL represents the sequential exposure of modified damp heat with full-spectrum light. These are the two accelerated exposures used in this study. 34

3.2 The extracted global feature values for the $EL@I_o$ image of one cell before and after mDH accelerated exposure. 43

4.1 The average and standard error (SE) of the change in the four normalized electrical features, including ${}^{n}P_{mp,IV}$, ${}^{n}I_{sc,IV}$, ${}^{n}R_{s,IV}$, and ${}^{n}P_{mp,PIV}$, for brands A and B under each accelerated exposure. 56

4.2 The number of observations for each cluster under different subsetting conditions, including encapsulant materials, module architectures, and cell types after each accelerated exposure for brand A. 59

4.3 The number of observations for each cluster under different subsetting conditions, including encapsulant materials, module architectures, and cell types after each accelerated exposure for brand B. 60

4.4 The medium value of selected features of each cluster for brands A and B. 60

4.5 The correlation coefficient between ${}^{n}F_{sd,EL@I_o}$ and ${}^{n}F_{sd,PL@OC}$ for each brand, each cell type, and under each accelerated exposure. 70

5.1 Specifications of the five regression models used to predict the module temperature readings. 79

6.1 The five models considered for the $< S|R >$ and $< S|M|$ pathway model. 108

6.2 The average percent change of the three normalized degradation mechanism features for each exposure of all of the modules. 112

6.3 The number of module variants for each model format that performed best under each model format and the average adj R^2 for each pathway of each accelerated exposure. 112

6.4 The number of module variants for each model format that performed best under each model format and the average adj R^2 for each pathway of the outdoor exposure. 113

6.5 The results of $CCSF^*$ and CCC comparing the models for each module variant between mDH and the outdoor exposure. 114

6.6 The results of $CCSF^*$ and CCC comparing the models for each module variant between mDH+FSL and the outdoor exposure. 114

7.1 Camera exposure times of different EL images for modules with monofacial cells and bifacial cells. 129

7.2 The specification of each modeling experiment and its resulting testing RMSE. 135

7.3 The number of parameters in each layer for CNN#1. 136

7.4 The model expressions for the convolution parts in CNN#1 to CNN#10. 139

7.5 The number of parameters in each layer for RNN#1. 141

List of Figures

2.1 Multilayer structure of the PV module. 6

3.1 The front and back side appearance of one DG minimodule. 32

3.2 Possible material choices for each layer within the sixteen module variants. 34

3.3 The three layouts used for minimodules. Layout 2 and 3 were only used for minimodules under mDH+FSL. The units are millimeters. 35

3.4 The Eternalsunspire solar simulation for the I-V measurement and the three curves measured from a cell in one laminated minimodule. 38

3.5 The Sinton stage for the $Suns$-V_{oc} measurement and the $Suns$-V_{oc} and Pseudo I-V curves results of a cell in one laminated minimodule. 39

3.6 The imaging room for the system designed by Tau-Sci used to measure EL and PL images. 40

3.7 The resulting eight images from one GB minimodule measurement. (a), (b), and (c) are the EL images measured with injected currents of 9.4 A, 4.7 A and 2.4 A respectively while (e), (f), and (g) are their corresponding dark images. (d) and (h) are the open-circuit and short-circuit PL images. 41

3.8 The $EL@I_o$ images for one cell before and after the mDH accelerated exposure with and without the Otsu threshold. 42

3.9 The 32 outdoor minimodules installed on a fixed rack, arranged into three rows and eleven columns. 44

4.1 ${}^{n}P_{mp,IV}$ for brand A minimodules after each accelerated exposure. 53

4.2 ${}^{n}R_{s,IV}$ for brand A minimodules after each accelerated exposure. 54

4.3 ${}^{n}I_{sc,IV}$ for brand A minimodules after each accelerated exposure. 55

4.4 ${}^{n}P_{mp,PIV}$ for brand A minimodules after each accelerated exposure. 55

4.5 Normalized electrical feature results, including ${}^{n}P_{mp,IV}$, ${}^{n}R_{s,IV}$, ${}^{n}I_{sc,IV}$, and ${}^{n}P_{mp,PIV}$, for brand B minimodules after each accelerated exposure. 56

4.6 The pairwise correlation for the six selected normalized features after each accelerated exposure. 57

4.7 $r({}^{n}P_{mp,IV}, {}^{n}R_{s,IV})$ using different subsetting conditions. 57

4.8 $r({}^{n}F_{sd,EL@I_o}, {}^{n}F_{sd,PL@OC})$ using different subsetting conditions. 58

4.9 The proportion of data variance explained by each principal component for brands A and B. 59

4.10 The hierarchical clustering dendrograms for brands A and B. Three clusters are obtained for each brand by cutting at the height of 19.5. 59

4.11 Principal component scores for brand A of each input observations, colored by the clusters identified by the hierarchical clustering result. The arrow displays the loading of each variable, of which the projected length can be understood as the weight for each original variable when calculating the principal component. 60

4.12 Principal component scores for brand B of each input observations, colored by the clusters identified by the hierarchical clustering result. The arrow displays the loading of each variable, of which the projected length can be understood as the weight for each original variable when calculating the principal component. 61

5.1 Percentage of outliers in each day for module temperature readings of the outdoor module sa43070. 81

5.2 Percentage of abnormal module temperature readings for two outdoor modules: sa43001 and sa43057. 81

5.3 Percentage of abnormal module temperature readings for each outdoor minimodule. 82

5.4 Boxplots of the adj R^2 and the testing MAE evaluated from the normal readings for the five models predicting the module temperature. 82

5.5 The normalized electrical features obtained from the $SunsVoc$ package for outdoor module sa43099, including ${}^{n}P_{mp,IV}$, ${}^{n}I_{sc,IV}$, ${}^{n}R_{s,IV}$, and ${}^{n}V_{mp,PIV}$. 83

5.6 The four power loss factors obtained from the $SunsVoc$ package for outdoor module sa43099, including ΔP_{Isc}, ΔP_{Voc}, ΔP_{Rs}, and ΔP_{Imis}. 84

5.7 The average value, 83.4% CI, and 95% CI of the four normalized electrical features, including ${}^{n}P_{mp,IV}$, ${}^{n}I_{sc,IV}$, ${}^{n}R_{s,IV}$, and ${}^{n}V_{mp,PIV}$, from the final three months for each module variant. 85

5.8 The average value, 83.4% CI, and 95% CI of ${}^{n}R_{s,IV}$ from the final three months for each module. 86

5.9 The average value, 83.4% CI, and 95% CI of ${}^{n}P_{mp,IV}$ of the four packaging combinations considering only the encapsulant materials and module architectures using data from the final three months. 86

5.10 The average value, 83.4% CI, and 95% CI of the normalized uniform current power loss (${}^{n}\Delta P_{Isc}$) from the final three months of exposure for each module variant and each module, respectively. 88

5.11 The average value, 83.4% CI, and 95% CI of the normalized recombination power loss (${}^{n}\Delta P_{Voc}$) from the final three months of exposure for each module variant and each module, respectively. 89

5.12 The average value, 83.4% CI, and 95% CI of the normalized power loss due to series resistance (${}^{n}\Delta P_{Rs}$) from the final three months of exposure for each module variant and each module, respectively. 90

5.13 The average value, 83.4% CI, and 95% CI of the normalized current mismatch power loss (${}^{n}\Delta P_{Imis}$) from the final three months of exposure for each module variant and each module, respectively. 91

5.14 The average value, 83.4% CI, and 95% CI of the four normalized power loss factors for the four packaging combinations from the final three months of exposure. 92

6.1 Illustration of the process for obtaining the optimal cross-correlation scale factor ($CCSF^{*}$) by comparing the scaled indoor model to the outdoor model in their overlapping exposure time. 109

6.2 The normalized electrical features over time for module variant 8 under mDH and the outdoor exposure. 111

7.1 Extracted cell images from an $EL@I_o$ module image obtained from a glass-backsheet (GB) module measured at baseline. 127

7.2 The raw $EL@I_o$ image (a), the baseline subtraction image (b), and the enhanced S/N EL image (c) for a solar cell in a laminated module after five steps of mDH exposure. 129

7.3 The model architecture for the simplest and most complex CNN models. 131

7.4 Comparison of the testing RMSEs for adding dropout layers and modifying dense layers and max-pooling layers in CNN#1. 136

7.5 Comparison of the testing RMSEs for adopting kernel regularization, activation regularization, and batch normalization in CNN#1. 137

7.6 Comparison of the testing RMSEs by scaling the output feature using three models. 138

7.7 The learning curves after adopting batch normalization and the minimum-maximum scaler to CNN#1+0.5D. 138

7.8 Comparison of the testing RMSEs for CNN models with different convolution structures. 139

7.9 Comparison of the testing RMSEs for different kinds of images as the input using CNN#1+0.5D model returned at the latest checkpoint during 50 epochs of training. 140

7.10 Comparison of the testing RMSEs of RNN models with differences in the number and the output dimension of GRU layers using the raw $EL@I_o$ images as the input. 141

7.11 The learning curves for RNN#1 and CNN#1+0.5D+RNN#1 up to 50 epochs of training using the raw $EL@I_o$ image as the input. 142

7.12 Comparison of the testing RMSEs of CNN, RNN and CNN+RNN model examples with three kinds of input images, including the raw $EL@I_o$ images, the baseline subtraction $EL@I_o$ images, and the enhanced S/N EL images. 143

Glossary

I_{sc}**:** The short-circuit current. 9, 13, 16, 17, 20, 21, 37, 38, 44, 50, 62, 64, 77, 79, 95, 96, 105, 106, 115

MMS**:** The minimum-maximum scaler.. 130, 134, 135, 137, 138, 142, 143, 144

PLR**:** Performance loss rate.. 17, 18, 19, 20, 74, 75, 94, 99, 113

P_{mp}**:** The maximum power. 13, 16, 17, 20, 21, 26, 36, 37, 38, 44, 50, 61, 77, 79, 94, 96, 97, 105, 123, 126, 129, 142, 149

R_s**:** The series resistance. 13, 17, 20, 26, 37, 38, 44, 50, 62, 77, 79, 87, 96, 100, 105, 106, 123, 126, 129, 142, 149, 153

R_{sh}**:** The shunting resistance. 9, 16, 17, 20, 37, 77, 79, 80

STS**:** The standard scaler.. 130, 134, 135, 142, 143, 144

V_{oc}**:** The open-circuit voltage. 9, 16, 17, 20, 21, 37, 44, 77, 79, 115

DG: Double glass. viii, xvi, 5, 6, 9, 11, 12, 13, 14, 15, 27, 31, 32, 33, 34, 36, 45, 46, 47, 48, 49, 50, 62, 65, 67, 68, 71, 72, 73, 74, 76, 85, 87, 98, 99, 104, 125, 152, 153

GB: Glass-backsheet. viii, xi, 5, 6, 9, 10, 11, 12, 13, 14, 15, 31, 32, 33, 34, 35, 36, 40, 41, 45, 46, 47, 48, 49, 50, 62, 65, 66, 67, 68, 71, 72, 74, 75, 76, 85, 87, 98, 99, 104, 125, 127, 152, 153

PERC: Passivated emitter and rear contact. 8, 14, 31, 76, 99, 105

RH: relative humidity. 10, 12, 13, 19, 36, 105, 126, 152

Acknowledgements

This material is based upon work supported by the U.S. Department of Energy's Office of Energy Efficiency and Renewable Energy (EERE) under Solar Energy Technologies Office (SETO) Agreement Number DE-EE-0008550. The views expressed herein do not necessarily represent the views of the U.S. Department of Energy or the United States Government.

First and foremost, I am incredibly grateful to my supervisor, Dr. Roger H. French, for his invaluable advice, continuous support, and patience during my Ph.D. study. His immense knowledge and plentiful experience have encouraged me all the time in my academic research and daily life. I would also like to thank Prof. Yinghui Wu and Prof. Jennifer Braid for their guidance and suggestions on my research. I would like to acknowledge all my other committee members, Prof. Laura Bruckman, Prof. Alp Sehirlioglu, and Dr. Xuanji Yu, for valuable instructions during my work.

I would like to thank Richard Tomazin, who miraculously repaired many instruments like Doraemon. I want to thank many members of my research group, Sameera Nalin Venkat, William Oltjen, and Raymond Wieser, for helping me complete many experiments. I would like to express gratitude to former members of my research group, Dr. Menghong Wang, Dr. Yu Wang, and Xuan Ma. Their kind help and support made my study and life here a wonderful time.

Finally, I want to thank my parents. Without their tremendous understanding and encouragement over the past five years, it would be impossible for me to maintain my studies abroad without any worries behind.

Abstract

Degradation of Bifacial & Monofacial, Double Glass & Glass-backsheet, Photovoltaic Modules with Multiple Packaging Combinations

Abstract

by

JIQI LIU

The annual installed capacity of solar energy has grown rapidly in recent years and reached 773.3 GW at the end of 2020, providing 3.1% of global electricity demand. The levelized cost of electricity (LCOE) of solar energy has been continuously decreasing since 2009 and reached $0.037/kWh in 2020. Improving the reliability of photovoltaic (PV) modules and reducing their degradation rates are critical for further decreasing the LCOE and maintaining market competitiveness. The degradation of PV modules depends on their interaction with exposure conditions and is strongly influenced by their packaging materials and combinations. In recent years, modules using polyolefin elastomer (POE), double glass (DG) module architecture, or transparent backsheet have been gaining market share and have become strong competitors to conventional monofacial ethylene-vinyl acetate (EVA) glass-backsheet (GB) modules. However, the reliability performance data of these emerging packaging strategies were lacking. This work used statistical analysis to compare the degradation behaviors of sixteen module variants under two indoor accelerated exposures and 1.6 years of outdoor exposure. The

two indoor accelerated exposures included modified damp heat (80 °C, 85% relative humidity) and modified damp heat with full-spectrum light, for up to 2,520 hours. The EVA+GB modules with opaque rear encapsulant exhibited a significantly greater power loss, and the dominant degradation mechanism was identified as interconnection corrosion. The outdoor exposure location was in the Dfa climate zone (continental, no dry season, hot summer). Significant differences in the average power loss were identified between three module variants and the other two. The dominant power loss factor for most module variants was uniform current power loss, followed by power loss due to increased series resistance. This work developed a cross-correlation algorithm to quantify the similarity of degradation behaviors under different exposures, considering the power loss rates and the similarity in trends for various electrical features over time. Enabled by extensive characterization data collected, various neural network models were explored to predict the change in electrical features based on images. Recurrent neural network (RNN) models outperformed convolution neural network (CNN) models, emphasizing the importance of utilizing measurements for the same sample taken at different exposure times to improve prediction accuracy.

1 Introduction

The annual installed capacity of solar energy has grown rapidly in recent years. The accumulated capacity has reached 773.2 GW at the end of 2020, providing 3.1% of global electricity demand and accounting for 10.7% of the total energy from renewable sources. The levelized cost of electricity (LCOE) of solar energy has been continuously decreasing since 2009 and reached $0.037/kWh in 2020, which is lower than that of wind, combined cycle gas turbine (CCGT), coal, and nuclear[1]. Improving the reliability and decreasing the degradation rate of solar energy are critical for further reducing its LCOE and maintaining its competitiveness.

The degradation of photovoltaic (PV) modules depends on their interaction with exposure conditions. Commercial PV modules contain several layers to protect internal solar cells. Most PV modules in the market are monofacial and use ethylene-vinyl acetate (EVA) encapsulant and a polymer backsheet for nearly 40 years[2]. However, modules using polyolefin elastomer (POE) encapsulant, glass[3] or transparent backsheet[4] for the rear cover have been gaining market share and have become strong competitors of conventional PV modules, due to the rise of bifacial modules[3] and the higher requirement for resistance to potential induced degradation (PID)[5]. Therefore, the packaging strategies in the current PV market exhibit more diversity. However, the reliability performance data of modules with these emerging packaging materials and combinations are lacking. Moreover, studies examining samples under indoor accelerated exposures often fail to report the statistical significance of results or to use identical materials and fabrication processes for different studied samples. Outdoor data are even rarer for these new products. Therefore, whether these different packaging strategies lead to differences in PV modules' reliability performance under certain environmental conditions is unknown. Comparing PV modules with these different packaging strategies using statistical analysis to identify performance differences is significant in guiding the packaging selection and predicting the lifetime of commercial PV modules.

This work examined the degradation behaviors of sixteen module variants under two indoor accelerated exposures or 1.6 years of outdoor exposure, evaluated by the confidence intervals of different characteristic features. A cross-correlation algorithm was developed to compare the module degradation behaviors under different exposures considering both the power loss rate and similarity in trends of both power and other degradation mechanism features. Enabled by the extensive characterization data collected in this work, the ability of neural network models to predict the change in electrical features based on images was explored.

Chapter 2 reviewed the literature for four scientific topics related to this work. Chapter 3 introduced details of the module fabrication, indoor accelerated exposures with stepwise characterizations, and outdoor exposure with timeseries data acquisition. Chapter 4 analyzed the degradation behaviors of sixteen module variants of two brands under the two accelerated exposures for 2,520 hours, with the comparison of the percentage of change for different mechanism features, pairwise correlation coefficients, and unsupervised clustering to study the activated degradation mechanism and dependency on packaging components. Chapter 5 introduced the timeseries data processing procedure and compared the degradation behaviors of the sixteen module variants and four packaging combinations after 1.6 years of outdoor exposure. Chapter 6 developed a cross-correlation algorithm and introduced its working principle and results' interpretation using the dataset from this work as an example. Chapter 7 explored the ability of neural network models to predict the change in electrical features using image input. From chapters 4 to 7, each one contained descriptions of its specific research significance, study objects, characterizations, and analytical methods.

2 Literature Review

In this chapter, a basic introduction of the photovoltaic (PV) module and its reliability study is given, and recent relevant research progress and literature are reviewed. The content is divided into four major sections: packaging of PV module, the outdoor reliability study using timeseries electrical data, the application of machine learning models in the PV reliability study, and methods to correlate degradation behaviors under indoor accelerated and outdoor exposures. The content about common accelerated exposures and module-level characterizations is added to the section 2.1 due to many related experimental results.

2.1 Packaging Strategies of PV Modules

The lifetime of a commercial PV module is usually between 20 to 30 years. Within the warranty, the reduction of power output is usually assumed as linear, and by the warranty deadline, the retained power output should be around 80%[6]. The working environment of PV modules contains complex outdoor conditions that change based on location and time. The outdoor stressors that lead to the degradation of PV modules include light, especially ultraviolet (UV) light, extreme temperatures, temperature cycling, humidity, hail, wind, sand, dust, and a potential difference. The PV module needs a suitable packaging design with proper materials to achieve the warranty target under such conditions, so solar cells, which generate electricity converted from light through photovoltaic effect and are dominated by the crystalline silicon (Si) material, can maintain their performance.

There are five layers in a commercial PV module shown in Fig. 2.1, including the front glass, the front encapsulant layer, solar cells, the rear encapsulant layer, and the substrate layer. The substrate layer can be divided into two major categories, glass and polymer backsheets, which are practically referred to as backsheets. The PV module using a polymer backsheet is usually mentioned as in the glass-backsheet (GB) module architecture, and that using glass is described as in the double glass (DG) module architecture. Besides these five layers, a commercial PV module also contains several other components, including an edge seal, a junction box, and sometimes a frame[7]. The degraded performance in PV modules results from the interaction between the exposing environment and the PV module itself. So similar PV modules could have different degradation performance or activated mechanisms when exposed to different conditions, such as installed in locations of different climates[8]. PV modules using different materials, module architectures, and fabrication processes could also have very different degradation performance[9]. All of them complicate requirements for the reliability of PV modules.

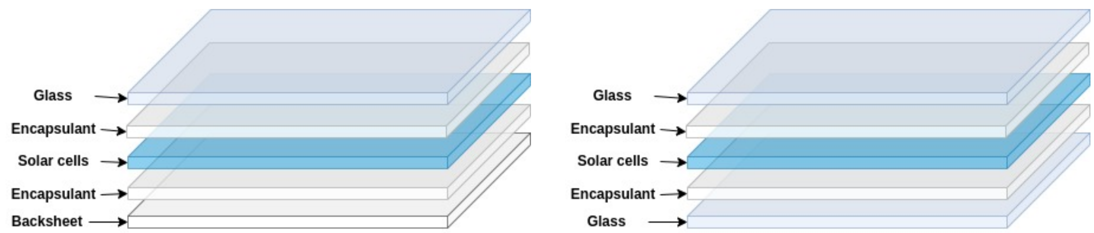

(a) Glass backsheet (GB) (b) Double glass (DG)

Figure 2.1. Multilayer structure of the PV module.

2.1.1 PV Encapsulants: EVA vs. POE

The encapsulant materials need to hold the electrical components such as solar cells in place, provide electrical insulation, and reduce or prevent the ingress of harmful substances. They also need a high transmittance and to be optically coupled at the interface and protect solar cells from corrosion and mechanical stress[10, 11]. These targets request the encapsulant to adhere well to all surfaces in the lifetime of PV modules and maintain stable properties. There were many materials considered in the early stage of development, such as polydimethyl silicone (PDMS), ethylene-vinyl acetate (EVA), polyvinyl butyral (PVB), polyolefin elastomer (POE), thermoplastic polyolefine (TPO), and ionomer[10]. EVA has been the dominant encapsulant material for almost four decades, considering the cost and properties[2].

The cost of EVA has played an essential role in using it instead of other materials. In the initial stage of commercializing PV modules around 1960 to 1970, most encapsulant materials were based on PDMS, due to their outstanding stability against UV and heat[10]. EVA has a backbone consisting of carbon-carbon (C-C) bonds, while PDMS has a backbone consisting of silicon-oxygen (Si-O) bonds. Their dissociation energies are about 83 kcal/mol and 108 kcal/mol, respectively, resulting in enhanced durability of silicon encapsulants like PDMS over hydrocarbon-based materials like EVA[10]. EVA is a copolymer of ethylene and vinyl acetate (VA), and its properties can be tailored by adjusting the VA content. Typically, a 27 wt% to 33 wt% VA content is used as the PV encapsulant. Polyethylene (PE) is a cheap and simple polymer, but it is opaque semi-crystalline, and its modulus is too high to protect the solar cell mechanically. VA is a transparent and amorphous polymer with a glass transition temperature (T_g) around 35 °C, which is too high that can cause it to transform to the brittle glassy state in the range of PV modules' operating temperatures. Therefore, some VA is added to PE to decompose the crystals and make the copolymer a semi-crystalline and highly transparent material. Meanwhile the T_g get reduced to -15 °C[12]. In order to shorten the manufacturing time, delay and hinder the degradation of EVA, various additives of a small amount are added, including peroxides as curing agents in lamination, UV absorbers, UV stabilizers, antioxidants, and adhesion promoters[7, 10].

Based on observations of PV modules aged in the field, most problems related to the encapsulant itself were delamination and discoloration. Delamination is due to the breakage of interfacial bonds, which is related to high humidity and not simply proportional to the dose of UV light[13]. When delamination occurs at the edge of a PV module, it can develop faster due to much easier water ingress, bringing safety concerns due to the current leakage. When it happens to the middle area of the PV module with a size that is not likely to grow further, it could cause a transmittance decrease depending on whether it is located above the cell[11]. Discoloration not only leads to the decrease of transmittance, which further causes a power loss, but is also an important indicator of polymer aging. There were two mechanisms proposed to explain EVA discoloration. The preferred mechanism is the degradation of additives. The peroxide reacts with the UV absorber and phosphite, leading to the discoloration of EVA[11]. Another popular mechanism is the degradation of EVA itself through the Norrish I, II, and III reactions. These reactions generate products containing polyenes with unsaturated conjugated double bonds, ketones, aldehydes, acetic acids, free radicals, and some gas molecules, such as CH_4, CO, and CO_2. Free radicals can further aggravate the chain scission as well as crosslinking[2, 11]. The VA group is the main culprit behind the degradation of EVA since the PE group is much more stable[2, 14]. If oxygen exists and oxides the unsaturated polyene, the rate of yellowing can be slowed down due to photo-bleaching. One EVA degradation product that brings lots of concern is acetic acid. It not only leads to corrosion of the metal contact but also has a self-catalytic effect of accelerating the degradation of EVA[7]. In addition, acetic acid could also promote the diffusion of Na^+ from the glass to the cell layer leading to more power loss due to potential induced degradation (PID)[11].

It is generally believed that the generation of the PID problem is due to the long-term exposure to a high voltage. With an increasing scale of PV power plants, a higher system voltage is desired to increase the number of PV modules connected in a string and reduce the number of inverters, which can lower the cost of the overall system[15]. There were three types of PID identified, namely shunting (PID-s), polarization (PID-p), and metallization or cell-stack corrosion (PID-c). The last one was discovered on the backside of bifacial passivated emitter and rear contact (PERC) monocrystalline Si cells in 2019. Research showing that it is a common problem for bifacial PERC cells was limited currently, and the theory was still in a hypothetical stage[16]. On the other hand, PID-s and PID-p were well understood. The PID-s is due to the accumulation of

Na^+, which decorates Si crystalline defects like stacking faults and results in conductive shorts through the emitter layer in the solar cell. Therefore, it usually leads to a lower shunting resistance (R_{sh}) and power output[17]. The PID-p is mainly because of the concentrated charge in the silicon nitride, which is the anti-reflect layer in the solar cell. The accumulated charge weakens the field-effect passivation. It thus increases the chance of recombination, leading to a lower short-circuit current (I_{sc}) and open-circuit voltage (V_{oc}) besides a lower power output[18].

Volume resistance is an indicator of anti-PID performance. Generally, the larger the volume resistance, the better anti-PID performance is. The volume resistance of commercial POE is usually higher than that of EVA in one to two orders of magnitude[10]. A study showed that using EVA and POE films with similar volume resistance (8.5×10^{13} $\Omega \cdot$ cm for POE and 1.3×10^{13} $\Omega \cdot$ cm for EVA), the module made by such EVA reached the saturation of power loss around 10% to 15% in several minutes, while the module made by such POE needed around five hours in the dark PID test. Therefore, the anti-PID performance is not directly proportional to the volume resistance and maybe also related to the properties of the ion channel in the polymer[5]. Water permeability could also lead to a difference in anti-PID performance when exposed to a high humidity environment since it is easier for the ion to diffuse with more moisture contained. The water vapor transmission rate (WVTR) of POE is an order magnitude smaller than that of EVA[10]. Multiple studies showed that using POE as the encapsulant can bring a significant improvement for anti-PID, regardless of GB or DG module architectures[5, 15, 18].

Although the anti-PID performance can be improved for EVA to a certain extent by adjusting the composition and additives, it has been shown difficulties reaching the increased requirement with the base material EVA itself unchanged[15]. The rising trend of using glass as the substrate highlighted the concern of PID since the rear glass acted as another sodium source. Therefore, POE has begun to occupy a considerable market share and become the major competitor for EVA. POE is a copolymer of PE and octene[19]. A significant advantage is the absence of acetic acid when degrading by replacing the VA side group with alkanes[20].

The transmittance of POE and EVA are very similar[10, 21]. A study showed that EVA and POE laminated film samples had no apparent changes after 3,300-hour damp heat exposure of 85 °C and 85% relative humidity (RH)[21] using the results of Fourier Transform Infrared Spectroscopy (FTIR) and Thermogravimetric Analysis (TGA). However, the UV transmittance dropped in POE samples, which might be related to the formation of chromophores or the migration of additives. After 200 kWh/m^2 UV exposure, the transmittance in the visible light range decreased by 1.7% and 4.0% in the EVA and POE samples, respectively. The temperature corresponding to a 95% retained weight decreased by 21 °C (the first stage maximum decomposing temperature is about 350 °C) for EVA and 29 °C (the maximum decomposing temperature is about 474 °C) for POE, respectively. Therefore, the authors believed the stabilities of EVA and POE were very similar[21]. It is worth noting that the EVA sample in this study most likely contains much more UV absorbers than POE, speculating from the initial transmittance curves. Therefore, the comparison is not entirely determined by different base materials. Another study showed that the GB PV module with EVA or POE as encapsulant both presented slight yellowing after 3,000 hours of the damp heat exposure. However, only the EVA module had corrosion on the silver grid and ribbons[20]. Based on the current published studies, EVA and POE have performed very similarly regarding stability, and

POE has established a better anti-PID performance. It has no acetic acid as a degradation byproduct, relieving the concern of aggressive corrosion. No unique problems have been identified for POE so far. However, there were still limited publications about POE and its degradation. Research comparing POE and EVA commercial PV modules under outdoor exposures was very rare in recent years.

2.1.2 Module Architecture: GB vs. DG

The front glass is generally the low-Fe tempered glass for the GB PV module with a thickness of 3.2 mm. DG modules now reduce the glass thickness to 2 mm or 2.5 mm to lower the weight to be competitive with GB modules and still able to pass the standard mechanical test. Their glass could be tempered or heat-strengthened[22]. Generally, the glass used in PV modules has an anti-reflect coating and some textures to increase the contact area to the encapsulant layer.

The substrate of PV modules could be made of glass or a polymer sheet, usually referred to as a backsheet. According to the ITRPV 2021, DG modules had an 18% market share in 2020 and were expected to continuously grow over years to reach a 55% market share in 2031[1]. Conventional PV modules are monofacial, so the backsheet is usually opaque to protect encapsulant layers from reflected light. The backsheet typically has three layers. The inner layer, which is contacted with the encapsulant layer, needs to offer durable adhesion and chemical compatibility and be stable under direct sunlight filtered through glass and front encapsulant layers. Materials such as fluoropolymers, polyamide (PA), PE, or EVA are commonly used. The core layer is thicker and provides the mechanical and electrical properties required for the overall backsheet. This layer is usually polyethylene terephthalate (PET), while few backsheet types use PA or polyolefine. The outer layer needs to be highly durable, as it provides environmental protection for the other layers and gets directly exposed to the environment, such as the reflected light. It is typically made of PET, polyvinylidene fluoride (PVDF), or polyvinyl fluoride (PVF)[11].

The identified degradation modes for backsheet include delamination, cracking, chalking, burns, blister, and discoloration. The WVTR and the permeability of acetic acid and oxygen of backsheet are much higher than glass, so the small molecular of such species could enter or leave the module[11]. Therefore, backsheets are usually described as breathable as compared to glass. The DG architecture is also used for monofacial PV modules with an opaque rear encapsulant layer to gain more reflected light for a similar power output to GB modules[23].

For commercial monofacial modules, EVA is often used for both DG and GB PV modules. In a study published in 2009, 204 PV modules were investigated after about 20 years of outdoor exposure in a moderate subtropical climate (-10 °C to +35 °C, with less than 90% RH). The average power loss was 23% for DG modules, while that of GB modules was 14%. So the DG modules showed a more significant power loss than the GB modules. However, the sample size for DG modules was relatively small, constituting about 10% of all studied modules, and their power losses distributed very dispersedly. Since most PV modules in this study were manufactured around 1980 to 1990, the encapsulant of PV modules had various options such as EVA, PVB, and silicone, especially for DG modules[6]. Another study compared DG and GB modules using three commercial PV modules after 10 to 21 years of outdoor exposure in a dry and hot climate. The DG module got exposed for ten years, and the two GB modules got exposed for 18 and

21 years, respectively. The degradation rate for the DG module was higher as 1.46%/a. and 2.28%/a. for the maximum power (P_{mp}) and I_{sc}, respectively. The two GB modules had degradation rates as 1.01%/a. and 0.44%/a. for P_{mp}, and 0.41%/a. and 0.29%/a. for I_{sc}[2]. Such differences were possibly caused by the higher operating temperature in DG modules, higher chances of thermomechanical fatigue of cell interconnects, and the accelerated EVA degradation due to the impermeability of glass[22].

While DG modules performed worse in the field, the studies comparing DG and GB modules under indoor accelerated exposures have shown that the performance was comparable, and DG modules even more often presented a better performance. A study compared DG and GB modules with EVA as the encapsulant under damp heat test using various temperatures and RH settings and found that the finger interruption happened earlier in DG modules under drier conditions than GB modules. GB modules showed an increase in series resistance (R_s) more severe in more humid conditions, indicating the occurrence of corrosion. It was found that DG modules lost power faster under a drier condition due to mechanical failures, and GB modules lost power faster under a more humid condition due to more corrosion[24]. Zhang et al. selected several commercial DG and GB modules and compared their performance under several accelerated exposures, including 600 cycles of temperature cycling, 3,000 hours of damp heat, 600 hours of PID test, and 50 hours of humidity freeze test[25]. DG modules outperformed the GB modules under all tests. The maximum difference happened in the humidity freeze test, which is a 2.72% and 33.73% power loss for the DG module and the GB module, respectively. Another study showed that DG modules could delaminate earlier than GB modules. This study first applied 1,000 hours of UVA exposure and then 1,000 cycles of dynamic mechanical loading (DML) of 1,500 psi at 1/6 Hz, followed by another 1,000

DML cycles of 1,500 psi at 1 Hz. The DG module was found to delaminate on the module edge at the second DML, while the GB module did not show the same problem[4]. Tang et al. compared the DG modules to the conventional GB modules using a sequential accelerated exposure. The sequential exposure consisted of 200 hours of damp heat, 60 hours of UV, 10 hours of humidity freeze, another 129 hours of UV test, the second 20 hours of humidity freeze, and 1,000 DML cycles. The power loss for the DG modules was 3.35%, while that for the GB modules was 4.14%[23]. These variances in comparing DG and GB modules are likely caused by differences in product manufacturing, materials selection, and exposure conditions. For such a comparison, the sample should follow strict variable control and be similar to the commercial product, or enough samples are needed to represent the population. However, DG modules attracted less attention with a minor market share for monofacial modules. There were limited publications about DG modules, and their reported performance varied a lot.

As bifacial PV modules emerged and occupied more market share, the market share of DG modules has increased due to their bifacial nature. The rear side of bifacial solar cells also can convert electricity from light, reducing the cost by increasing the power output by 5% to 30%[3]. The cost of bifacial PERC cells is very similar to monofacial PERC cells[3]. A backsheet product named transparent backsheet arose to compete with the glass as the substrate. Just like the conventional backsheet, the properties of the transparent backsheet also vary with the selected materials[26]. A study showed that the PVF-based transparent backsheet was very durable[27]. After 500 hours of UV exposure, the UV absorption decreased by 18%, the elongation at break decreased by 30%, and the transmittance in the visible range was unchanged. Gu et al. found that GB modules outperformed DG modules using POE as the encapsulant under PID test at -1500 V with damp heat conditions[3]. However, another study, which also used a PVF based transparent backsheet with POE as the encapsulant, found the DG module outperformed the GB module under ± 1000 V PID test with damp heat conditions[5].

Some other factors were also usually discussed for comparing DG and GB modules. The DG module was heavier than the GB module, and the increasing module size enlarged the weight difference. Reducing the glass thickness could lower the weight difference, but it also reduced the maximum impact strength against hail weather for the front cover. Due to the symmetry structure of DG modules, they usually performed better under DML, indicating a lower risk in windy weather. The transparent backsheet could block more UV light with the UV transmittance of about 1% initially, compared to around 40% to 50% for glass. The transparent backsheet is also more resistant to alkali corrosion and easier to clean due to the hydrophobic surface. Although the wear resistance is no doubt better in glass, the transparent backsheet could withstand a 50 L sand falling test, so the difference regarding the wear resistance within the lifetime of the PV module could be minor in sandy weather[28]. It is important to note that most commercial PV modules are still monofacial. Although bifacial modules were predicted to have a 70% market share in 2030, there are currently many challenges, such as solving the current mismatch sourced from the rear irradiance, optimization of the PV system, and an accurate performance estimation[22]. The widely used testing standard IEC 61215 has not yet differentiated between monofacial and bifacial modules.

2.1.3 Accelerated Exposures & Module-level Characterizations

Many accelerated exposures mentioned above originate from the IEC 61215, which is mainly designed to detect infant failure due to improper design instead of studying the wear-out failure around the product warranty[29]. In many studies that focused on the long-term reliability of PV modules, the exposure conditions are derived from the standard with significantly increased exposure time or cycles. Some identified failure modes from the field survey were hard to reproduce under single stressor exposure, such as the formation of cracks in the co-extruded PA backsheet. Such failure mode could be activated under sequential test or multi-stressor test[11].

P_{mp} is generally used as an overall performance indicator to evaluate module performance under different accelerated exposures. However, it provides limited insights into the degradation mechanisms. Other I-V features that are extracted from current-voltage (I-V) curves are more helpful in identifying the activated degradation mechanisms. For example, under the PID test, the mechanism can be concluded as PID-s or PID-p through whether the change presented on R_{sh} or I_{sc} and V_{oc}[18]. If spatial information is also desired to identify defects and their properties, imaging technologies are needed, such as electroluminescence (EL), photoluminescence (PL), and dark lock-in thermography (DLIT).

2.2 Outdoor PV Reliability Study with Timeseries Electrical Data

Studying the performance of PV modules under real-world operating conditions is essential for monitoring power plants' health, evaluating the PV module's reliability, and improving the design of future products. As more and more PV power plants were built with advanced data acquisition systems, more timeseries electrical data with an operating time long enough for reliability study became available[30]. These timeseries electrical data can be mainly divided into two categories: the timeseries P_{mp} and other timeseries electrical variables such as I_{sc}, V_{oc}, R_s, and R_{sh}. The former is much more abundant and is often used to calculate the performance loss rate (PLR) and further predict or forecast the lifetime of installed PV modules.

2.2.1 Time-series Power: *PLR* Calculation

PLR, which is referred to as the degradation rate sometimes, was shown as the third most important factor influencing the levelized cost of electricity (LCOE)[31]. It is not practical to use the outdoor environmental conditions to examine the warranty of PV modules which is about 20 to 30 years[32]. The lifetime and PLR that can be found in the datasheet of a commercial PV module are predicted or estimated values rather than measured ground truth. Lots of studies have proved that PLR varied with climates of installed locations[8, 33, 34]. Therefore, the real PLR of an installed PV module usually differs from the value provided by the datasheet. While lots of PLR results were reported in the last twenty years, there was no standard on how it should be calculated. The PLR calculation commonly follows three steps. The first step is the data filtering, such as removal of observations with extreme irradiance values, clear-sky filter, and timeseries outlier detection for soiling and snowing[30, 32]. Next, a performance matrix is selected to calculate a performance-rating parameter for the PV system. The choices can be categorized into three groups: electrical parameters corrected to standard testing conditions (STC), predicted P_{mp} at a specified condition from empirical models such as XbX[35], PVUSA[32], and corrected performance ratio, which is the ratio of the actual energy yield over that under the reference conditions[32]. The last step is to apply a model to extract the rate of change, like the slope in a linear model. These models fall into two major categories: statistical and analytical models.

The statistical models were more widely used. A simple linear model, also referred to as ordinary least squared regression (OLS), is applied to the timeseries performance matrix with or without a trend extraction which removes seasonality and noise. Several options were often compared together for extracting the trend, such as classical seasonal decompose (CSD), Holt-Winters (HW) exponential smoothing, season and trend decompose using LOESS (STL), autoregressive integrated moving average (ARIMA)[32], and robust principal component analysis (RPCA)[36]. A study showed that ARIMA and STL performed relatively better, especially compared to a directly applied OLS, considering the smaller uncertainty in the calculated PLR due to their robustness in different filtering conditions and outlier handling and less sensitiveness to seasonality[32]. However, some studies also showed that the uncertainty difference was not significant, and a directly applied OLS could offer very comparable results for high-quality data[33, 37]. Another method called year-on-year (YoY) was also often used for determining PLR. This method applies the simple linear model (OLS) to points of the same time (such as the same day, the same month) across multiple years or every two subsequent years to obtain a PLR distribution, from which the expectation and uncertainty can be evaluated. YoY was also proved to be more robust against outliers and less sensitive to seasonality compared to OLS [38, 39].

The performance loss is not always linear, especially in the early installation and in the wear-out stage[40]. The pattern of the performance loss depends on the degradation mechanisms. Degradation modes such as light-induced degradation (LID) and light and elevated temperature induced degradation (LETID) were observed to have non-linear power loss, while encapsulant discoloration, which was the most widely reported problem for the installed module, caused approximately linear power loss[40]. Some studies applied the piece-wise linear regression[40, 41] or reported the PLR using different numbers of years to account for non-linearities.

Another model category to calculate PLR is the analytical model, like the Arrhenius model, which usually has exponential terms[32, 42–44]. The independent variables were environmental stressors such as RH, average temperature, light dose for the pure physics-based model[32, 41] and the exposure time for the hybrid model[42, 44]. In the pure physical model, many parameters such as different activation energies were estimated from laboratory accelerated exposures applied to similar modules. Additional field observations were also requested to validate the dominant degradation mechanism for choosing the proper model corresponding to different reactions[32]. The published hybrid model suggested using data with at least 3% degradation for the fitting[42].

Besides the model selection, data quality and imputation methods for missingness also have influences on the PLR result. With more timeseries data becoming available, data quality, imputation, and their influence on the PLR determination captured attention in the recent three years. Many visualization methods were suggested to investigate the existence of specific data problems, such as data synchronization, data gap, and data shift[30]. Moreover, both the latest IEA Task 13 report[35] and a publication of Livera et al.[45] proposed some data processing and data quality verification frameworks. The latter also compared the uncertainty in the performance ratio using different models to impute the missing irradiance, power, module temperature with different percentages of missingness.

2.2.2 Utilization of Other Timeseries *I*-*V* Features

While timeseries P_{mp} is useful to obtain PLR, it offers limited insights into the cause of power loss. Other I-V characteristic features such as I_{sc}, V_{oc}, R_s, and R_{sh} can provide more information regarding the activated degradation mechanisms[40, 46, 47]. For example, the drop in I_{sc} was often associated with the encapsulant discoloration, and the increase in R_s indicated corrosion or solder bond fatigue[40]. However, tracking I-V features requests additional equipment, so timeseries I-V data were less available than the timeseries P_{mp}. Some tracking equipment record the timeseries I-V curves and directly measure all I-V features, while others only measure several features. The I-V features can be extracted from the I-V curves using a physical diode model[48] or a data-driven model[49]. The former has less bias but is computationally expensive due to the iteration algorithm to solve the Lambert W equation. On the other hand, the latter may contain some bias in the resistance features extracted, it requests fewer computational sources and has better repeatability and is inherently comparable[50].

The approach to quantify the rate of change for these I-V features is similar to that of PLR. The percentage of change in power associated with different features is not directly proportional to that in different I-V features due to their physical relationship to power. Several studies proposed methods to construct the outdoor I_{sc}-V_{oc} curve[51, 52] and further correct the curve and decompose the total power loss into several power loss factors[51, 53]. Wang et al. also published a corresponding open-source R package on CRAN[54], so the developed algorithm could be easily implemented to other data[46]. Moreover, the outdoor I_{sc}-V_{oc} curves and similar curves such as $Suns$-V_{oc}, $Suns$-V_{mp} can be used for monitoring the operation of PV power plants and irradiance sensors[15, 52].

2.3 Machine Learning Methods Applied in PV Reliability Study

Machine learning models have been applied to various research and applications in solar energy. The major applied research fields include operational fault detection of PV power plants, power forecasting, and solar cell defect classification. The implemented models can be categorized into three classes, including supervised, semi-supervised and unsupervised, based on whether the input data have labels or dependent variables. They can also be classified into regression or classification based on the targeting problem. This section introduces study frameworks and machine learning models frequently used for different research topics.

2.3.1 PV Array Operational Fault Detection

The safety and health of a PV power plant are inseparable from timely and effective problem diagnosis and elimination. Common operation faults include temporary or permanent shading, anomalies or errors on either alternating current (AC) or direct current (DC) side of the inverter, connection errors in the solar arrays such as open circuits, line-line fault, and damaged PV modules[55]. Such operational faults are challenging to troubleshoot with visual inspection. Many troubleshooting characterizations such as I-V scanning require at least a part of the PV array to be disconnected, reducing generated energy. Therefore, it has become an important research topic to identify faults without interrupting the regular operations of power plants. Most input data for fault detection could be divided into two categories: thermographic images and electrical parameters such as P_{mp}, I_{sc}, V_{oc}, I_{mp}, and V_{mp}[56]. Environment-related variables sometimes are added, such as module temperatures, plane of array irradiance (POA), and global horizontal irradiance (GHI)[56, 57].

The thermographic image can be used directly as the input or can undergo some image processing to highlight hot spots and then be input to classification models[58]. Several image processing methods include gamma correction, masking, and edge detection[58]. The classification model types that directly use images as the input are convolution neural networks (CNNs)[59, 60], extreme gradient boosting (XGBoost), random forests (RFs), and support vector machines (SVMs)[58]. Feature vectors also can be extracted from images and used as the input. Such feature vectors contain results from both local and global feature extractors, such as contrast, energy, homogeneity, and correlation obtained from the Gray Level Co-Occurrence Matrix (GLCM) and the histogram of gradient features[61, 62]. Then an artificial neural network or a simple classifier like Naive Bayes can replace the CNN to achieve comparable performance, like achieving an accuracy above 90%[61, 62]. It is known that CNN is a feed-forward neural network where each neuron affects the other neurons in the adjacent layer to preserve the spatial correlation of images so that CNN can capture local image characteristics. The trained convolution kernel in CNN models plays a role of an image feature extractor. Besides model structure and parameters' settings, the CNN performance depends on the sample size. A study showed that when the input images were less than 5400, the model had a testing classification accuracy much lower than that of the model trained with more images[60]. When input images were limited, like less than one thousand, using feature vectors as the input delivered a considerably better result[61]. At present, models proposed in this area have generally achieved more than 95% accuracy[60–62]. However, there was a lack of public image datasets for a model competition. It was challenging to identify the best model across different datasets, especially when their performances were very similar[58].

Models for fault detection using electrical data as the input have the same problem with more complexity due to simulation. Since electrical data for a specific operational fault is difficult to collect naturally, the data used in some studies were simulated by inputting actual weather data to some PV array circuit simulation algorithms. However, such data did not contain errors and noises in the measured electrical data. So the actual performance in the real application was very likely to be different from the reported value[55]. Most classification machine learning models have already been tested in this area[56, 63]. Some studies proposed semi-supervised classification methods to make the model learn from both labeled and unlabeled data through graph shifting[57] or conditional probability[64].

2.3.2 Power Forecasting

Power forecasting is a typical problem of regression through time. Some studies structured the input data as observations of the same time point (like a month or a day) across different years to forecast the corresponding time in the following year. Then multiple machine learning algorithms such as RF[65], Gradient Boosting Regressor (GBR)[65], Decision Tree (DT)[65], ANN[66] were tested in different studies. However, structuring input data in such a way is not necessary. The recurrent neural network (RNN) is a typical machine learning model that processes timeseries data for prediction or forecast[67]. It can process variable-length input sequences using its internal state. Because the depth of an RNN neuron is decided by the length of the input sequence, which could be relatively long in some cases, a plain RNN neuron is likely to encounter a gradient vanishing problem through backpropagation. It could form a short-term memory and hinder performance improvement through training with more input data. Therefore, some special RNN neurons are more popular used for RNN models such as long short-term memory (LSTM)[68] and gated recurrent unit (GRU)[69]. Both of them have gates using a sigmoid function to control the balance between long-term memory and the current updated state so that the information obtained from the very early input can also reach the recent output[68, 69]. Karimi et al. utilized the temporal coherence in the power output for an individual power plant and the spatial coherence of the power plants located in different places[70]. A graph layer decided by the geometric distance was added in between RNN temporal layers to form several spatiotemporal blocks in the model structure. Such a model was proved to have a better performance than the model using the RNN temporal layer only.

2.3.3 Solar Cell Defect Detection

EL is commonly used to identify solar cell defects within a PV module. It has a much higher resolution than the thermographic image. Thermographic images are more often used in diagnosing operational faults in a large-scale PV power plant to identify whether or not a PV module has abnormal hot spots and the location of such a problematic PV module in a PV array. So the input images are for PV modules or arrays. EL images are generally taken from each module to identify the damaged solar cell inside. Therefore the EL image for each cell is generally extracted from the module EL image and used as the input for modeling. Al-Mashhadani showed examples of defects that were detectable in the EL cell image, such as cracks, finger interruptions, and contact failures[71]. Many studies applied CNN models for the solar cell defect classification. These models were usually customized to have about five convolution layers [72, 73] or modified from published popular CNN models like the VGG series[74, 75].

The targeting predicted classes could be binary, such as defective and defect-free[74], or multiple depending on types of defects, such as cracked, corroded, and finger interrupted[72, 73]. The image data used for model development generally were unbalanced due to fewer defective cell images. Image argumentation such as rotation and flipping has been shown to make the model more general and to improve the model performance[72, 74]. Using a CNN for classification is supervised learning, which requires data pre-labeling. Each category needs to have enough images to be included in the designed model, which makes some defects be ignored due to limited observations or physical understanding.

Unsupervised learning has the advantage of learning patterns from unlabeled data. Pierce et al. first extracted features from three aspects to form the feature vector and then applied hierarchical clustering to identify clusters through a dendrogram[76]. K-means and hierarchical clustering are both popular unsupervised classification algorithms. Hierarchical clustering builds a hierarchy of clusters through merging or splitting depending on the direction of growth. K-means algorithm aims to partition n observations into k clusters. Each observation belongs to the nearest cluster decided by the distance to centers or centroids, serving as cluster prototypes. Compared to K-means, the hierarchical model has the advantage of a more flexible distance matrix, more stable results without random initialization, and no need to define the number of clusters in advance. However, it is computationally more expensive than K-means, making it less popular to apply to large datasets. The quantitative results using EL images primarily focus on classification, with very little work linking EL images to the overall electrical performance. Karimi et al. defined four image features as the median intensity, the fraction of dark pixels after thresholding, the normalized busbar width, and a corrosion degree[77]. Then the normalized P_{mp} and R_s were predicted by polynomial fitting from the defined image features. Such artificial features may not be applicable for different image datasets. While most solar cells in this study had degrees of corrosion, the major problem presented in another image dataset could be something else, such as cracking or area isolation. Although the images used in this study were obtained from step-wise characterizations of modules under indoor accelerated exposures, the correlation between features of the same cell at different exposure steps was not exploited in the prediction of performance parameters.

2.4 Correlate Lab Reliability Results to Real World Performance

PV modules operate under complex and varying environmental conditions. It is not practical to examine PV module lifetime using field conditions due to the long duration. Therefore, indoor accelerated exposures are commonly applied to study reliability with more aggressive conditions. It is essential to match results from indoor accelerated exposures with field performance for lifetime prediction or evaluation of conditions and duration needed for aging samples in the lab to satisfy specific outdoor performance requirements.

There are generally two ways to correlate results from indoor accelerated exposures and outdoor exposures. One is to match the exposure conditions using accumulated values or the average of environmental variables. The other is to match the degradation performance of samples under different conditions and further estimate an accelerated factor. Here are several examples of the first approach of matching the exposure conditions. Miller et al. used the maximum shear stress of glass|EVA|glass samples to study the adhesion at the interface[13]. Cumulative radiant was used to visualize the stress reduction for samples under different exposures. Another study used finite element method (FEM) models to study the water ingress into the DG module[78]. After obtaining several parameters related to the encapsulant through measurements of water vapor transmission rate (WVTR), a FEM model was built to estimate the water ingress with temperature and humidity conditions varying over time. The total mass of absorbed water calculated for a sample after one hour of the standard damp heat exposure was roughly equal to the one calculated for 584 hours in Miami, Florida. If the interested area was changed as a 1.5 cm wide strip close to the edge, then one hour of the standard damp heat led to the same total mass of absorbed water in the interested area as the mass estimated for 21.6 hours in Miami. Bheemreddy et al. used the Hallberg-Peck Model, which is a corrosion rate model to compare PV module performance under different exposure conditions[79]. In addition to environmental variables such as temperature and humidity, the model contained parameters such as activation energy, time exponent, and relative humidity exponent. Those parameters were obtained by fitting experimental data under various conditions. Kaaya et al. used three empirical kinetics models describing the degradation rate through hydrolysis, photo-degradation, and thermo-mechanical degradation, respectively[80]. Then the degradation rate considering the synthetic effect of different reactions was assumed to be equal to the product of that in each reaction[80]. The major difficulty of matching exposure conditions for such comparison is considering influences from multiple environmental variables and their variation over time. The FEM model can simulate influences propagating to the PV module from different exposure conditions. However, material and interface properties that are critical for simulations are usually unknown for various commercial PV modules, and simulations are computationally expensive. Using a single environmental variable creates the problem of ignoring the effects of the others. Such neglect sometimes is inappropriate, depending on how determinant the role of the selected environmental variable is. For example, Miller et al. found humidity and the hygrometric (combined temperature and humidity) instead of the cumulative UV dose heavily reduced the adhesion[13]. These studies sometimes ignored changes in environmental variables over time and made assumptions about activated degradation mechanisms and their synthetic relationships[79, 80].

The other way is to match the characterization results of the exposed samples. Gu et al. first confirmed that the kinetic behavior of samples under an outdoor exposure was similar to that under UV + 75% RH + 55 °C accelerated exposure by analyzing the surface morphology through the atomic force microscopy (AFM) and identifying changes in the functional groups through FTIR[81]. Then the authors decided an acceleration factor between outdoor and this indoor accelerated exposure by comparing the amount of chemical changes. Kersten et al. used the ratio of power loss from PV modules installed in Cyprus and those under the current injection around maximum power status at 75 °C[82]. It found that installing the PV modules in Cyprus for one year led to a power loss equal to 290 hours under the designed accelerated exposure. A similar approach was also taken by another study, which investigated the acceleration factor between outdoor exposure and multiple PID tests at different temperatures[83]. An essential premise of using such an approach is to assume or prove that the dominant degradation mode is consistent between results from different exposures. For example, if a PV sample under outdoor exposure experiences power loss because of encapsulant discoloration, and another sample under indoor accelerated experiences power loss due to interconnect corrosion, the acceleration factor obtained by matching their power losses has no practical meaning. Therefore, in most cases, studies confirmed that the activated degradation mechanisms are identical through multiple characterizations[81] or made assumptions based on exposure conditions and observed degradation behaviors[82, 83]. For PV modules without access to further inspections, Liu et al. proposed an algorithm to evaluate the similarity in rates and trends by comparing models describing how power and electrical mechanism features change over time[84]. If the trends of degradation mechanism features were more similar, the scale factor is more likely to be accepted.

3 Experimental and Analytical Methods

This study aims to quantitatively analyze and compare the degradation behaviors of PV modules with different packaging strategies under different exposure conditions. The power loss was quantified, and the activated degradation mechanism was identified. In order to accomplish this goal, a four-part study was devised. The first part is the fabrication of PV modules. Secondly, the indoor accelerated exposures are applied with multiple characterizations at specific exposure steps. The third step consists of outdoor exposure with electrical features and weather variables tracked over time. The aforementioned three parts are experimental and introduced in this section since they were used in more than an individual result section. The last part is for the data analysis. This includes the processing of lab characterization results and outdoor timeseries data and creating models. The modeling aspect incorporates regression, hierarchical clustering, neural networks, and an algorithm developed specifically in this study to compare module degradation behaviors under different exposures. Each analysis method is introduced in a separate chapter under the related research topic.

3.1 Fabrication of Minimodules

The type of PV module used in this study is a minimodule that contains four solar cells connected in series. Fig. 3.1 shows the front and backside of a DG minimodule. Five junction boxes were installed on the backside and labeled from A to E to enable electrical measurements for each cell. In total, there are 192 minimodules produced. Half of the minimodules, labeled as brand A, were fabricated by a PV company using its standard commercial process. Our Solar Durability and Lifetime Extension Center (SDLE) at CWRU fabricated the remaining minimodules labeled as brand B. However, it should be noted that the solar cells used to make brand B minimodules were supplied by the same company that fabricated the brand A minimodules. All these solar cells are P-type multicrystalline silicon PERC cells, doped with boron. The production duration for brand A minimodules was very short, which was about one month, while brand B minimodules were made in batches based on sets, and it took about three months to make one set. There was roughly a three-month gap between the fabrication of each set of brand B minimodules. Some cell discoloration was observed during the fabrication of set #3 and set #4 minimodules despite proper containment within a box accompanied by nitrogen flow. Three different types of encapsulant materials were supplied by a company: transparent, UV-Cutoff, and opaque with differences in additives. Some literature also refers to the opaque encapsulant as "white encapsulant" instead. This company also supplied the KPf backsheets used for sets #1, #2, and #3. The KPf backsheet has three layers. The inner layer is a fluorine coating, the core layer is PET, and the outer layer is PVDF. Despite different compositions, the KPf backsheets appear white on both sides. Another company supplied the transparent backsheets used for the GB minimodules in set #4. The transparent backsheet also has three layers: the inner layer is the transparent fluoroethylene vinyl ether (FEVE), the core layer is PET, and the outer layer is PVF. The frontal glass for GB minimodules is tempered and 3.2 mm thick, while the glass for DG minimodules is heat-strengthened and 2.5 mm thick.

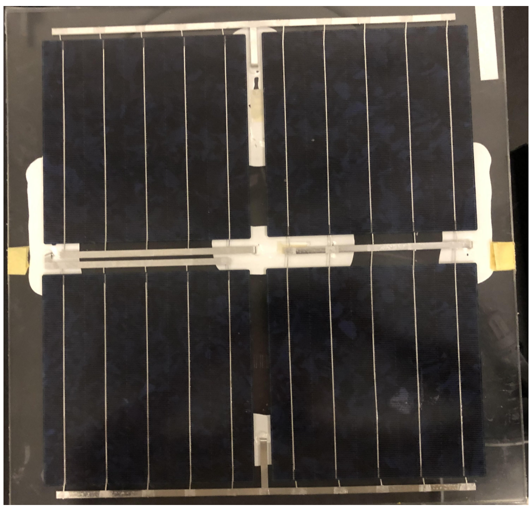

(a) Front side.

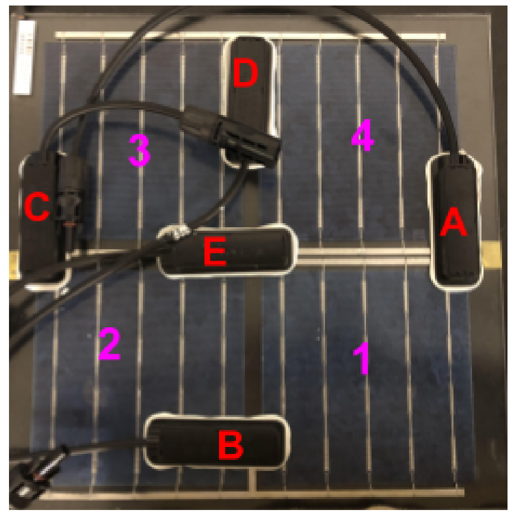

(b) Backside.

Figure 3.1. The front and back side appearance of one DG minimodule.

There are three steps in the module fabrication process, including soldering, lamination, and junction box installation. The busbar and tape that are used to connect the four cells together in a module were manually soldered for all brand B minimodules. When soldering a busbar, a cell was put on a small hot plate to maintain a constant temperature of 55 °C. The temperature of the soldering tip was set to 315 °C. Then the soldered cells were stacked with the other layers of material, and everything was laminated using a P.Energy L036A laminator. Lamination involves two steps: evacuation and crosslinking. The evacuation step took six minutes. Crosslinking took 10 minutes per minimodule using EVA and 20 minutes per minimodule using POE. The crosslinking temperature for both kinds of modules was 145 °C. Both the lamination time and temperature were suggested by the company supplied encapsulant materials. Next, electroluminescence (EL) imaging was applied to inspect the laminated minimodule in order to detect and remove samples with severe damage like a penetrating crack. The final step was the installation of junction boxes. This fabrication procedure detailed above is for all brand B minimodules. Brand A minimodules were fabricated using a similar process with the main difference being that the equipment utilized is for commercial PV module production. Their soldering was automated which means that it was less likely to have cracking before and during exposure due to less local concentrated stresses. Furthermore, due to the difference in the laminator, the position of solar cells in brand A minimodules had less movement during lamination and followed the designed layout better than in brand B minimodules.

Table 3.1 lists the quantity and specifications of all minimodules within this study. There are sixteen module variants, divided into four sets, that have different PV components, as shown in Fig. 3.2. Within each set, there are four module variants to keep the comparison of EVA versus POE, and DG versus GB. There are differences in cell types and rear encapsulant types between minimodules of distinct sets. Set #1 and set #3 use monofacial solar cells, while set #2 and set #4 use bifacial solar cells. The rear encapsulant in set #1 is the UV-Cutoff type, set #2 and set #3 use the opaque type. Set #4 is an exception; the rear encapsulant is the UV-Cutoff type for the GB minimodules and the transparent type for the DG minimodules in order to demonstrate the configuration of commercial bifacial PV modules. If only considering the packaging materials, set #4 is more similar to set #1. It is worth mentioning that, regardless of the type of solar cells used, only set #4 is for bifacial modules. The others are all monofacial since the rear side of the module is not sensitive to light.

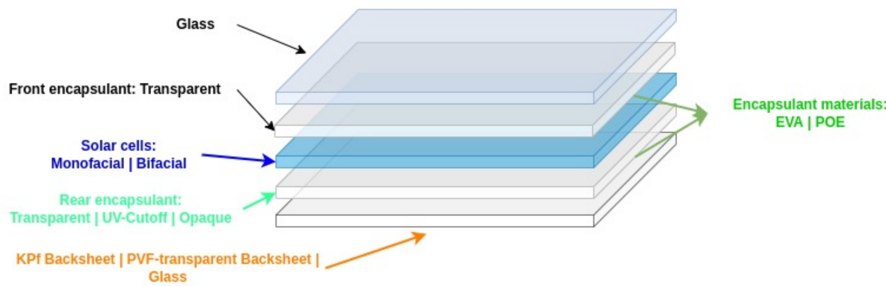

Figure 3.2. Possible material choices for each layer within the sixteen module variants.

Table 3.1. Detailed quantities and specifications of the minimodules that were fabricated and tested. mDH represents modified damp heat, and mDH+FSL represents the sequential exposure of modified damp heat with full-spectrum light. These are the two accelerated exposures used in this study.

Set #	Module Variant	# of modules Brand A	Brand B	# Retained	# Outdoor	# mDH	# mDH+FSL	Cell Type	Encap. Material	Rear Encap.	Architecture	Module Type
1	1	6	6	2	2	4	4	monofacial	EVA	UV-Cut	GB	monofacial
1	2	6	6	2	2	4	4	monofacial	EVA	UV-Cut	DG	monofacial
1	3	6	6	2	2	4	4	monofacial	POE	UV-Cut	GB	monofacial
1	4	6	6	2	2	4	4	monofacial	POE	UV-Cut	DG	monofacial
2	5	6	6	2	2	4	4	bifacial	EVA	Opaque	GB	monofacial
2	6	6	6	2	2	4	4	bifacial	EVA	Opaque	DG	monofacial
2	7	6	6	2	2	4	4	bifacial	POE	Opaque	GB	monofacial
2	8	6	6	2	2	4	4	bifacial	POE	Opaque	DG	monofacial
3	9	6	6	2	2	4	4	monofacial	EVA	Opaque	GB	monofacial
3	10	6	6	2	2	4	4	monofacial	EVA	Opaque	DG	monofacial
3	11	6	6	2	2	4	4	monofacial	POE	Opaque	GB	monofacial
3	12	6	6	2	2	4	4	monofacial	POE	Opaque	DG	monofacial
4	13	6	6	2	2	4	4	bifacial	EVA	UV-Cut	GB	bifacial
4	14	6	6	2	2	4	4	bifacial	EVA	Transparent	DG	bifacial
4	15	6	6	2	2	4	4	bifacial	POE	UV-Cut	GB	bifacial
4	16	6	6	2	2	4	4	bifacial	POE	Transparent	DG	bifacial

Each of the 16 module variants includes six minimodules from each brand. The six minimodules of brand A were partitioned to the outdoor exposure and the two indoor accelerated exposures with two minimodules for each. The six minimodules of brand B were partitioned to the retained group and the two indoor accelerated exposures with two minimodules for each. So there are two minimodules counting for eight cell samples under each accelerated exposure from each brand. Due to the dimensional restrictions of a mechanical loading test applied to all GB minimodules exposed to modified damp heat with full-spectrum light exposure (mDH+FSL), the size of these minimodules is larger in one dimension than that of the other minimodules. As shown in Fig. 3.3, for each brand of minimodules under mDH+FSL, one minimodule follows layout 2, and the other follows layout 3. All the other minimodules follow layout 1. The four cells always occupy a centralized square area no matter which layout is used. Layout 2 can be described as layout 1 with an extended area in the length direction and no change in cell position. The solar cells, as an entire unit, rotate 90 ° between layout 3 and layout 2.

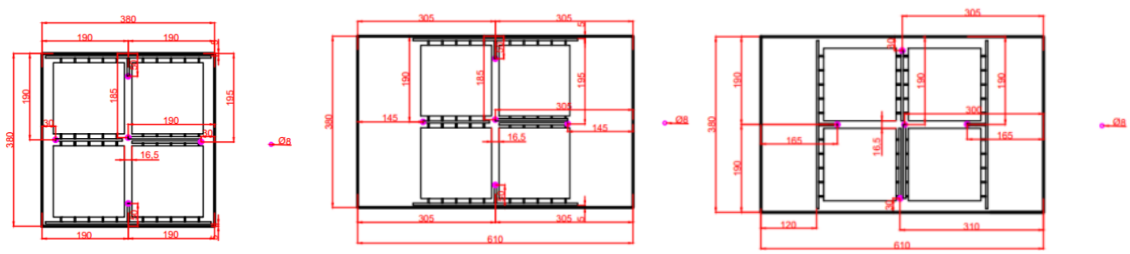

(a) Layout 1. (b) Layout 2. (c) Layout 3.

Figure 3.3. The three layouts used for minimodules. Layout 2 and 3 were only used for minimodules under mDH+FSL. The units are millimeters.

All minimodules were pre-conditioned before being exposed to different exposures. The pre-conditioning process consisted of two steps: light soaking as the first step, and boron-oxygen stabilization with current injection as the second step. However, there were some differences in how the pre-conditioning was conducted for the minimodules between the two brands. For brand A, minimodules were initially electrically shorted and placed outdoors to obtain a light dose as high as 40 kWh. Then, they were connected in series with a power supply to inject current around the current at maximum power (8.8 A) for 48 hours at room temperature. For brand B, minimodules were first put in the full-spectrum light chamber with a 0.5 Ω load resistor connected to have them operate around maximum power status. Their total light dose was also 40 kWh. Next, they were connected in series to a power supply that injected a current of 8.8 A. It should be noted that these modules were put into a climate chamber to make their temperature to about 80 °C. During the pre-conditioning, several minimodules from both brands were selected for current-voltage (I-V) measurements. Furthermore, it was observed that they reached the stable level specified in IEC 61215: the difference between the maximum and minimum P_{mp} should be less than 1% of the average P_{mp} in three consecutive measurements with a light dose interval more than 5 kWh.

3.2 Indoor Accelerated Exposures and Stepwise Evaluations

There were two kinds of accelerated exposures in this study. One was the modified damp heat (mDH), where the temperature was adjusted to be 80 °C with relative humidity (RH) of 85%. The temperature was lowered 5 °C below that of the standard damp heat to avoid overemphasizing the hydrolysis of PET which is the core layer material in the backsheet and has a T_g of 80 °C. This will result in a more fair comparison between GB and DG modules. In addition, most outdoor PV modules also do not operate at such high temperatures very often. The total exposure time, 2,520 hours, was divided into five exposure steps meaning each step spanned 504 hours (21 days). The other was a sequential accelerated exposure of modified damp heat with full-spectrum light (mDH+FSL). The total exposure time was also 2,520 hours, divided into five exposure steps. Each step's 21-day exposure was divided between two different tests: mDH for 14 days and FSL for seven days. The full spectrum light exposure (FSL) was conducted with a class C solar simulator based on specialized HID lamps from Iwasaki Electric. The average light intensity on the front and back sides of the exposed minimodule (due to reflection from the walls of the chamber) was 420.4 W/m^2 and 85.1 W/m^2, respectively. The FSL light source emitted minimal UV light. The light intensity for the range from 300 nm to 400 nm was only 6.68 W/m^2 and 5.52 W/m^2 for the front and back sides of the minimodule. Such light intensities are only about 10% of the practical UV exposure intensity for aging backsheets[85]. A 0.5 Ω load resistor was connected to each minimodule to make it operate around P_{mp}. The module temperature was below 70 °C under FSL. The primary purpose of the FSL exposure was to make the module fully operational, with the PV module likely containing degradation products initiated from mDH.

There were six measurement steps, including the baseline. At each step, there were four kinds of non-destructive characterizations, including current-voltage (I-V) curves, $Suns$-V_{oc}, electroluminescence (EL) images, and photoluminescence (PL) images. The I-V curves were measured at three different illumination levels: 1000 W/m^2, 500 W/m^2, and 250 W/m^2 at room temperature. Fig. 3.4 shows the Eternalsunspire solar simulator used for measurements and the curves for the three illumination levels measured from one cell in a laminated minimodule. Temperature corrections and the extraction of series resistance (R_s) using these three curves were performed based on IEC 60891. Other I-V features including P_{mp}, the current at P_{mp} (I_{mp}), the voltage at P_{mp} (V_{mp}), I_{sc}, V_{oc}, R_{sh} were extracted from the I-V curve measured at 1000 W/m^2 using the $ddiv$ package published on CRAN[49].

$Suns$-V_{oc} measures V_{oc} under varying illumination. It can be converted to a Pseudo I-V curve using I_{sc}. For individual cell-level measurements, changes in the Pseudo I-V curve (PIV) for aging solar cells reflect a change in the recombination behavior, and

(a) Instrument for I-V measurement.

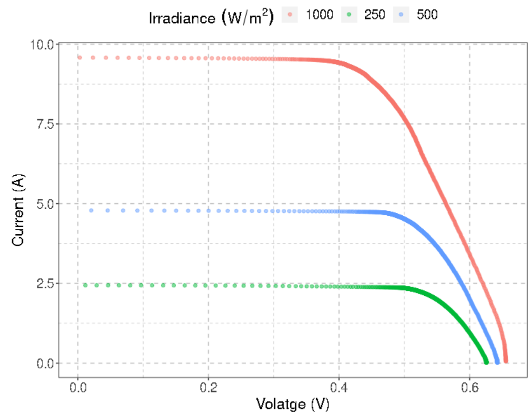

(b) I-V curves.

Figure 3.4. The Eternalsunspire solar simulation for the I-V measurement and the three curves measured from a cell in one laminated minimodule.

the curve is not affected by a change in series resistance (R_s)[86]. Fig. 3.5 shows the Sinton stage for performing the $Suns$-V_{oc} measurement and the $Suns$-V_{oc} and Pseudo I-V curves for a cell in one laminated minimodule. In our study, the Pseudo I-V curve (PIV) was converted from the $Suns$-V_{oc} curve using a constant I_{sc}, which was the nameplate value of 9.465 A, rather than the measured I_{sc} obtained from the I-V curve. This was done in order to eliminate the influence of a varied I_{sc} due to uncertainties in I-V measurements or the degradation of the encapsulant layer. From the PIV, some features such as P_{mp}, I_{mp}, and V_{mp}, are extracted similarly to I-V features.

EL and PL images were taken with a Tau Science PixEL system, using a 20.2 megapixel (5496 x 3672 pixels) ZWO ASI183MM Pro monochrome camera with a Peltier cooled Sony IMX183CLK J back-illuminated CMOS sensor, and green LED illuminators for PL measurements[87]. Fig. 3.6 shows the appearance of the room where images for a minimodule were captured. Eight images were taken per measurement. Three of them were

(a) Instrument for Sun-V_{oc} measurement.

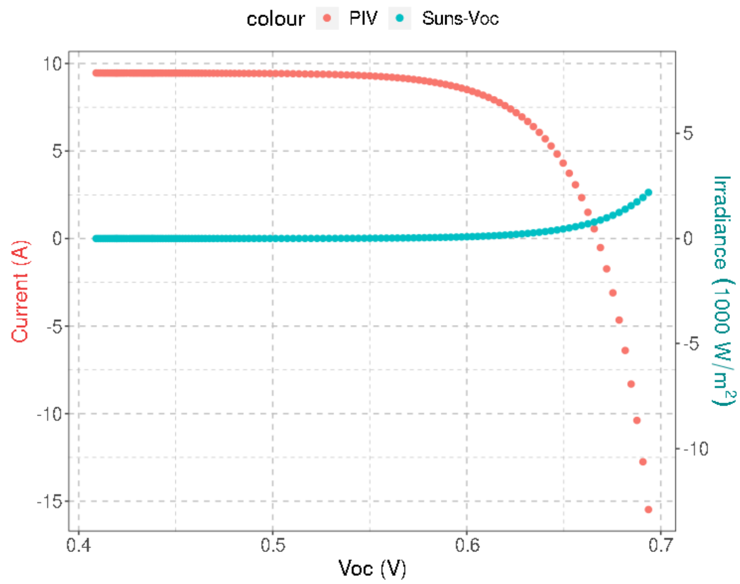

(b) the Sun-V_{oc} (cyan) and Pseudo IV curve (red).

Figure 3.5. The Sinton stage for the $Suns\text{-}V_{oc}$ measurement and the $Suns\text{-}V_{oc}$ and Pseudo I-V curves results of a cell in one laminated mini-module.

EL with different injected currents of 9.4 A (I_o), 4.7 A (0.5 I_o), or 2.4 A (0.25 I_o). The camera's exposure time for taking each image was adjusted to reasonably utilize the range of the allowed intensity in obtained images. Therefore, the lower the current is, the longer the camera exposure time is.

Three EL dark images were taken using the same camera parameter settings as their corresponding EL images without current being injected into the module. After dark subtraction, we denoted the three EL images as $EL@I_o$, $EL@0.5I_o$, and $EL@0.25I_o$. Two PL images were captured using the same illumination but different settings for the electrical status of the testing minimodule. Illumination was provided by ten green LEDs arranged in two columns. The intensity was about two times stronger than that in the corresponding band in the solar spectrum. One PL was performed with the module's current set to 0 A which is the open-circuit status. This image was labeled as $PL@OC$.

Another PL denoted as $PL@SC$ was performed with the voltage set to 0 V which is the short-circuit status. This image was then subtracted from the $PL@OC$ in order to obtain the third PL image, $PL@OC-SC$.

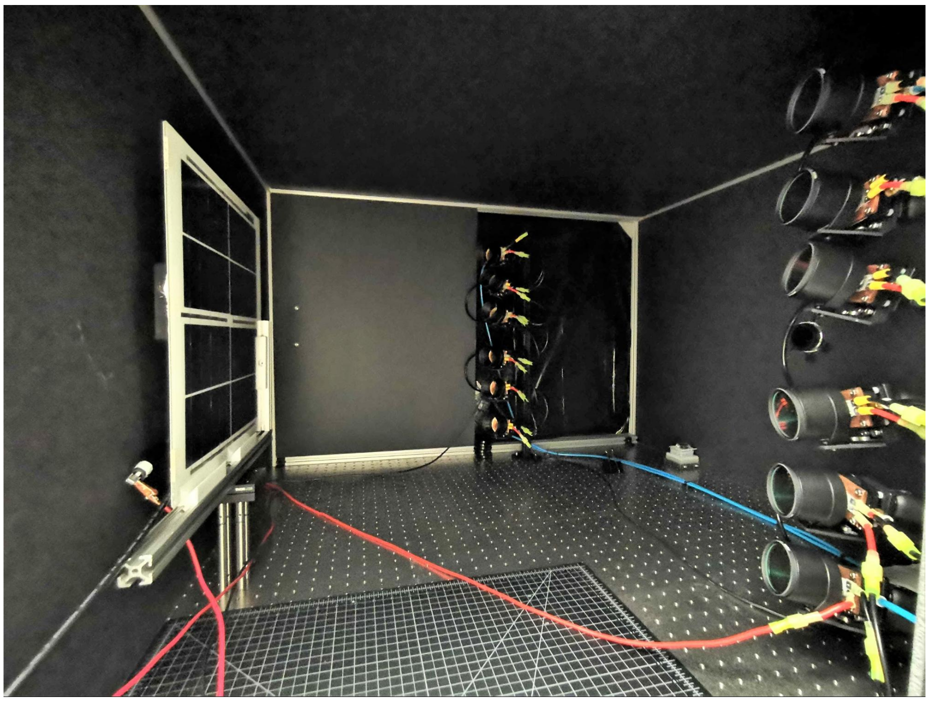

Figure 3.6. The imaging room for the system designed by Tau-Sci used to measure EL and PL images.

Fig. 3.7 shows the eight images obtained for one GB minimodule at baseline. The power supply to control electrical status of the testing sample is connected to the whole module when taking pictures. Next, each cell image was extracted from the module image using a published cell extraction Python pipeline from $pvimage$ package developed by SDLE[88]. Therefore, our $PL@SC$ is brighter than such images with electrical control applied to individual cells in other published literature due to the current mismatch effect resulting from cells connected in series.

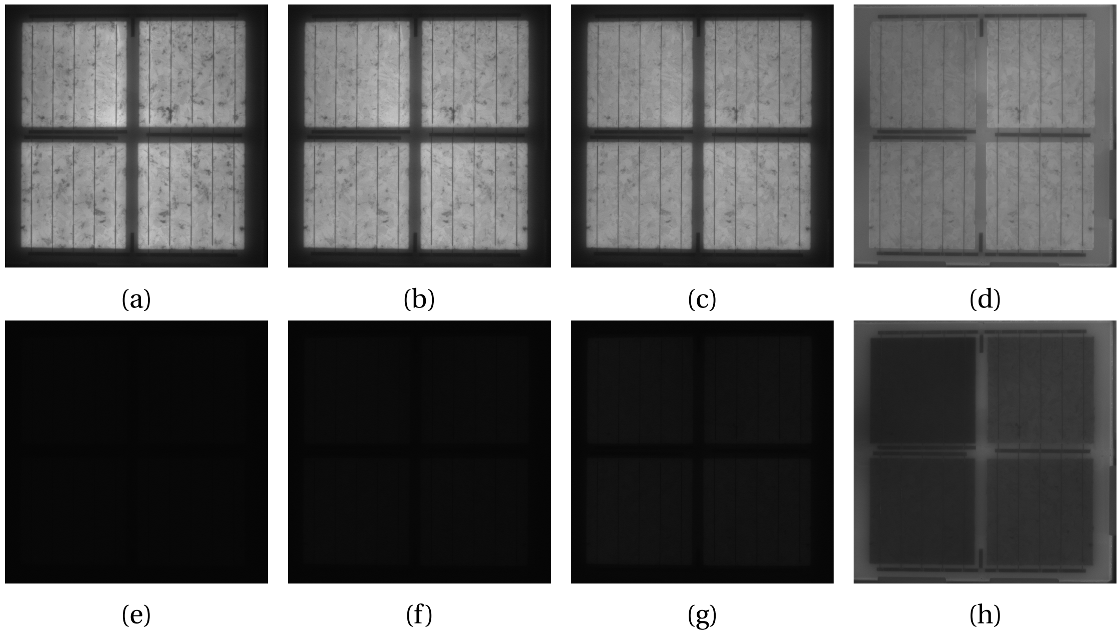

Figure 3.7. The resulting eight images from one GB minimodule measurement. (a), (b), and (c) are the EL images measured with injected currents of 9.4 A, 4.7 A and 2.4 A respectively while (e), (f), and (g) are their corresponding dark images. (d) and (h) are the open-circuit and short-circuit PL images.

$$F_{sd} = \sqrt{\frac{\sum (x_i - \mu)^2}{N}} \tag{3.1}$$

Despite an accurate signal control, there was still a small amount of signal drift during each measurement resulting in the average (F_{mean}) and median (F_{med}) intensities of the image being less useful to track the cell degradation. While it is not visible to the human eye, there is a uniformity issue in the images. The cell area closer to the camera is brighter which causes the fraction of dark pixel (F_{FDP}) after thresholding to no longer accurately reflect the size of a degraded area. However, we found that the standard deviation (F_{sd}) is not strongly influenced by these two problems, and the change of it can still indicate whether or not the image became more non-uniform due to degradation.

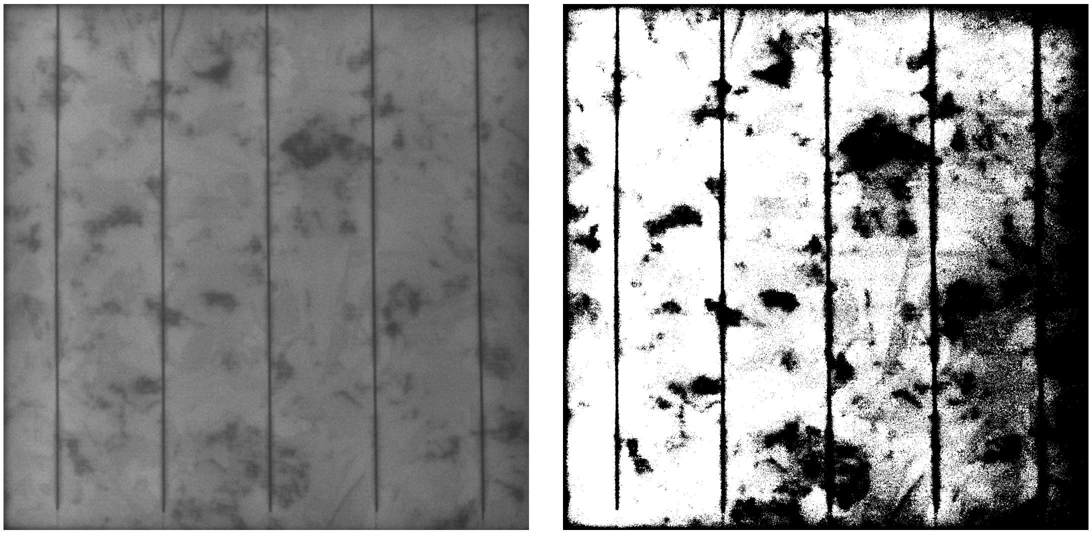

(a) $EL@I_o$ before exposure. (b) Thresholded $EL@I_o$ before exposure.

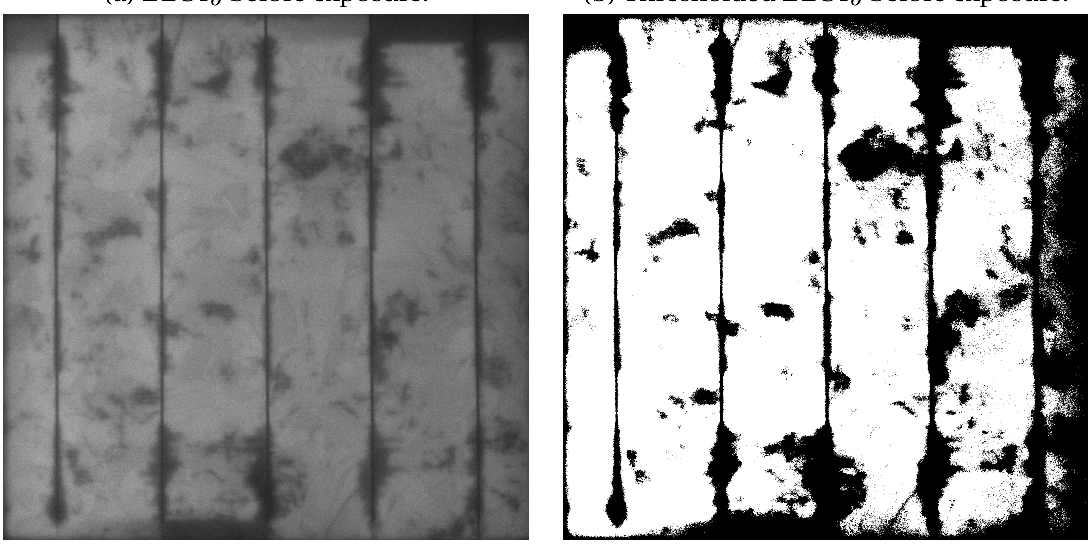

(c) $EL@I_o$ after exposure exposure. (d) Thresholded $EL@I_o$ after exposure.

Figure 3.8. The $EL@I_o$ images for one cell before and after the mDH accelerated exposure with and without the Otsu threshold.

The F_{sd} is calculated as Eq. 3.1 where μ is the average image intensity, N is the total number of pixels, and x_i is the intensity value of each pixel in the image. Fig. 3.8 shows the $EL@I_o$ for one cell before and after the mDH accelerated exposure with and without Otsu threshold[89], and Table 3.2 lists the F_{mean}, F_{med}, F_{FDP}, and F_{sd} for these two images without threshold. While comparing these two images without threshold, we can see busbar corrosion and some areas on the edge becoming inactive after the exposure; only F_{sd} changes as the expected direction.

Table 3.2. The extracted global feature values for the $EL@I_o$ image of one cell before and after mDH accelerated exposure.

Extracted Global Feature	Before Exposure	After Exposure
F_{mean}	0.4480	0.4492
F_{med}	0.4552	0.4694
F_{FDP}	0.3846	0.3143
F_{sd}	0.0750	0.1062

3.3 Outdoor Real-world Exposures and Timeseries Evaluations

There were 32 minimodules installed outdoors, with two minimodules for each module variant. They were located at the SDLE solar farm: 243 Mt Sinai Dr, Cleveland, OH 44106. The longitude and latitude of the site are -81.616° and 41.511°. According to the Köppen-Geiger climate classification system implemented by the kgc package[90], this installation site is in the Dfa climate zone, where the letter "D" stands for continental, the letter "f" represents no dry season, and the letter "a" stands for hot summer. The Dfa climate is generally not considered a very aggressive climate that leads to the degradation of PV modules due to a long winter period. The levels of aggressiveness in climates for PV degradation are generally thought of in the following order: hot and dry > hot and humid > moderate > snow and polar[11]. The Dfa climate is considered moderate. As shown in Fig. 3.9, the outdoor minimodules were mounted on a fixed rack in three rows and 11 columns with heights varying from 25 to 100 cm. The outdoor exposure started in May 2020, and data acquisition finished in December 2021, meaning that the analyzed service lifetime was 1.61 years. However, the exposure and data collection continued for future analysis.

Figure 3.9. The 32 outdoor minimodules installed on a fixed rack, arranged into three rows and eleven columns.

The electrical data from the minimodule were collected by a Daystar MT5 Multi-Tracer. The accuracies for both current and voltage are within 0.1% of the full scale (5 V, 15 A). The time interval for collecting I-V curves was ten minutes. I-V characteristic features such as P_{mp}, I_{sc}, V_{oc}, and R_s were extracted from the timeseries I-V curves. In addition, a T-type thermocouple was attached to the rear side of each minimodule around the cell center position in order to measure the module temperature T_{mod}. The measured temperature's accuracy was ± 0.5 °C. A Kipp Zonen CMP6 pyranometer was installed at the same location to measure the plane of array irradiance (POA). The pyranometer was installed three meters above the ground to avoid ground activities such as mowing the grass. The pyranometer and 32 thermocouples were connected to a Campbell Sci data logger for programming measurement and regular data collection. The time interval was set to one minute. The timeseries electrical data and sensor data were joined by the closest time.

4 Indoor, Stepwise, Accelerated Exposure Study of PERC Module Variants

Title to submit: **Statistically-informed, Stepwise, Degradation Study of the Impact of Differing Encapsulants and Double Glass vs. Glass-Backsheet Architecture of Mono- and Bi-facial PERC Minimodules**

In recent years, with the rise in popularity of bifacial PV modules, the market share of double glass (DG) modules has increased compared to that of conventional glass-backsheet (GB) modules, thus further increasing the need to replace ethylene-vinyl acetate (EVA) by polyolefin elastomer (POE) as the encapsulant material. The reliability of PV modules depends on materials, module architectures, and exposure conditions. This study compared the degradation behaviors of sixteen module variants from two brands with varying encapsulant materials (EVA or POE), encapsulant types, module architectures (GB or DG), and cell types (monofacial or bifacial) under accelerated exposures and applied hypothesis tests to determine statistical significance. The modules were exposed for 2,520 hours under two accelerated exposures: modified damp heat (mDH) and modified damp heat with full-spectrum light (mDH+FSL). The characterization methods used include current-voltage (I-V) curves, $Suns$-V_{oc}, electroluminescence (EL) images, and photoluminescence (PL) images. For both brands, two DG module variants with UV-Cutoff rear encapsulant have an average power loss of less than 5%, while the module variants of EVA+GB with opaque rear encapsulant have a significantly greater average power loss after each accelerated exposure. Interconnection corrosion is identified as the primary degradation mechanism contributing to power loss. Unsupervised hierarchical clustering finds that the degradation behaviors of modules from one brand with a more strict manufacturing control in soldering, lamination, and cell storage, strongly depend on module architectures only. However, the degradation behaviors of modules from the other brand show more complex dependency, including module architectures, encapsulant materials, and cell types.

4.1 Introduction

Thanks to rapidly advancing technology, newly installed PV systems in 2020 have a larger power generation capacity than any other renewable energy sources[1]. Since the degradation of PV modules depends on the design of module packaging and their exposure conditions, various indoor accelerated exposures have been designed to quantify the degradation of PV modules under specific environmental stressors. According to the type of rear sheet or cover, commercial PV modules can be categorized into two different module architectures: double glass (DG) and glass-backsheet (GB). With the rising popularity of bifacial PV modules, DG modules have an increased market share[1] due to their bifacial nature. At the same time, a new product called transparent backsheet was commercialized to compete with glass used as the rear cover of PV modules, and PVF-based transparent backsheet was found to be very durable. W. Gambogi et al. studied PVF-based transparent backsheet using 500 hours of UV exposure[27]. The UV absorption decreased by 18%, the elongation at break decreased by 30%, and the transmittance in the visible range was unchanged[27].

The market growth of DG modules motivates the replacement of EVA encapsulant. PV encapsulants need to hold electrical components like solar cells in place, and provide electrical insulation. They also need high transmittance and to be optically coupled at the interface, and protect solar cells from corrosion and mechanical stress[10, 11]. Therefore, the encapsulant needs to adhere properly to all interfaces during the lifetime of PV modules and maintain stable properties. EVA has been the dominant encapsulant for nearly four decades with over 80% market share due to a balanced property with cost ratio. However, its degradation product contains acetic acid, which can diffuse outside through backsheets but be sealed inside by glass[11]. Recently, another encapsulant material POE, which does not generate acetic acid, has risen to be the competitor of EVA. POE is a copolymer of polyethylene and octene[19] and the significant advantage of POE is the absence of acetic acid when degrading due to the replacement of vinyl acetate side group with alkanes[20]. Multiple studies have shown that PV modules using POE have a better resistance against potential induced degradation (PID) than EVA[5, 15, 18]. In addition, Barretta et al. found that the cross-linked film of EVA and POE had very similar stability under damp heat and UV accelerated exposures[21]. In recent years, the changes to packaging materials and module architectures brought challenges to reliability studies of PV modules. A few recent studies have compared DG and GB modules using different encapsulant materials. In outdoor studies, there are fewer DG modules than GB modules, and their reliability performance differs from that of recent DG modules due to changes in manufacturing and materials[2, 6]. Recent laboratory studies are also generally observational and lack statistically significant results. Therefore, no firm conclusion could be made on whether the degradation performance has a significant difference for modules with different encapsulant materials or module architectures[4, 20, 23–25].

In this study, the degradation behaviors of sixteen variants of DG and GB modules using different types of EVA or POE encapsulants were investigated under two indoor accelerated exposures: mDH and mDH+FSL. Our study objects are minimodules with four solar cells connected in series with five junction boxes. Each cell's electrical properties can be measured separately. The characterization methods include current-voltage (I-V) curves, $Suns$-V_{oc}, EL, and PL. The statistical significance from hypothesis tests[91] was reported in comparing average power loss and degradation mechanism features across different module variants to identify stable and relatively unstable module variants. Pairwise correlation[92] and principal component analysis[93] were also applied to identify activated degradation mechanisms. Furthermore, the dependencies of degradation performance on the choice of materials, module architectures, cell types, and manufacturing process were explored through unsupervised hierarchical clustering.

4.2 Methods

This section introduces the study object, accelerated exposure conditions, characterization methods with corresponding feature extraction, and the data analysis methods used, including principal component analysis (PCA) and unsupervised hierarchical clustering.

4.2.1 The Study Object: Research Minimodules

The study has sixteen module variants from two brands: A and B. Brand A minimodules are fabricated by a solar company using its manufacturing pipeline for commercial PV modules, while brand B minimodules are fabricated in labs of the CWRU SDLE Research Center. Two minimodules from each brand are put under each accelerated exposure, contributing to measurements from eight cells at each measurement step. The sixteen module variants, with differences shown in Fig. 3.2, are divided into four sets. Each set includes four different combinations: EVA+GB, EVA+DG, POE+GB, and POE+DG. Across the sets, cell type (monofacial or bifacial) and rear encapsulant type (transparent, UV-Cutoff, and opaque) differ. The first three sets are monofacial modules with the polymeric backsheet of GB minimodules being a KPf backsheet. Set #4 modules are bifacial modules with the backsheet for GB minimodules as a PVF transparent backsheet. The glass is made of 3.2 mm tempered glass or 2.5 mm heat-strengthened glass for GB and DG minimodules, respectively. Detailed specifications and quantities for the minimodules under indoor accelerated exposures are listed in Table 3.1.

4.2.2 Accelerated Exposures and Characterizations

Two accelerated exposures, mDH and mDH+FSL, were conducted in this study. Compared to the standard damp heat accelerated exposure, the temperature was lowered by 5 °C to avoid overemphasis on hydrolysis in PET, which is the material of the core layer of backsheet[11], to bring a more fair comparison between GB and DG modules. The total exposure time was 2,520 hours for each accelerated exposure, and each exposure step took 504 hours (21 days). Under mDH+FSL, a sequential exposure was conducted with mDH taking 2/3 of the time (14 days) and FSL taking the remaining 1/3 of the time (7 days) at each exposure step. The average irradiance intensity for the front and rear sides of the module under FSL were 420.4 W/m^2 and 85.1 W/m^2, respectively. In addition, a 0.5 Ω resistor was connected to each module in order to make it operate around maximum power (P_{mp}). The module temperature was below 70°C.

At each step, current-voltage (I-V) curves of three irradiance levels (1000 W/m^2, 500 W/m^2, and 250 W/m^2), $Suns$-V_{oc} curves, electroluminescence (EL) images at three current levels (9.4 A (I_o), 4.7 A (0.5 I_o), and 2.4 A (0.25 I_o)), and open-circuit (OC) and short-circuit (SC) photoluminescence (PL) images were collected. Another PL image denoted by $PL@OC-SC$ was obtained by subtracting the short-circuit PL image from the open-circuit PL image. The corresponding dark images were subtracted from each EL image, and the cell extraction pipeline from $pvimage$ Python package[88] was applied to extract individual cell images from module images. The R_s was extracted using all three I-V curves following IEC 60891. The P_{mp} and I_{sc} were extracted from the 1000 W/m^2 I-V curve using the $ddiv$ package[49]. Another P_{mp} was obtained from the Pseudo I-V curve (PIV) converted from the $Suns$-V_{oc} curve [86] using a constant I_{sc} as 9.465 A, which was the nameplate value for the cell. In addition, the standard deviation

(F_{sd}) from cell images, including the three EL images for different current levels ($EL@I_o$, $EL@0.5I_o$, and $EL@0.25I_o$), the open-circuit PL image ($PL@OC$), and the $PL@OC-SC$ was calculated. Features extracted from multiple characterization methods were further normalized by the value measured at baseline from the same cell. Outliers were removed separately by checking the observations of each module variant from each brand at each measurement step under each exposure using Eq. 4.1, where k was set as 3, and Q_1 and Q_3 were the lower and upper quartiles, respectively.

$$[Q_1 - k(Q_3 - Q_1), Q_3 + k(Q_3 - Q_1)] \tag{4.1}$$

4.2.3 Correlation Coefficient

Pearson correlation coefficient (PCC) measures the statistical linear relationship or association between two continuous variables[92]. It is the ratio between the covariance of two variables and the product of their standard deviations, as shown in Eq. 4.2. Therefore, it is a normalized measurement of the covariance. PCC always has a value between minus one and one, and the higher the absolute value, the higher the correlation. An absolute value higher or equal to 0.5 is recognized as a strong correlation, and an absolute value between 0.3 and 0.5 is a medium correlation.

$$PCC = \frac{\sum(x_i - \bar{x})(y_i - \bar{y})}{\sqrt{\sum(x_i - \bar{x})^2 \sum(y_i - \bar{y})^2}} \tag{4.2}$$

4.2.4 Unsupervised Hierarchical Clustering

Principal component analysis (PCA) is a process of computing the principal components to perform a basis transformation on the data while retaining as much information as possible in a lower dimension[93, 94]. Its computation relies on the singular value decomposition, and the resulting principal components are orthogonal to each other. Nine normalized features for each brand of minimodules after exposures were selected for PCA, including ${}^{n}I_{sc,IV}$, ${}^{n}P_{mp,IV}$, ${}^{n}R_{s,IV}$, ${}^{n}P_{mp,PIV}$, ${}^{n}F_{sd,EL@I_o}$, ${}^{n}F_{sd,EL@0.5I_o}$, ${}^{n}F_{sd,EL@0.25I_o}$, ${}^{n}F_{sd,PL@OC}$, and ${}^{n}F_{sd,PL@OC-SC}$.

The data were scaled and centered before using as the input for PCA. The first three principal components were taken for the agglomerative hierarchical clustering using Ward's linkage method. Ward's method, also called the minimal increase of sum-of-squares (MISSQ) method, evaluates the proximity between two clusters as the quantity by which the summed square in their joint cluster minus the combined summed square in the two clusters[95]. Intuitively, this method aims at finding compact, spherical clusters. It was chosen because it is better at avoiding making outliers as individual clusters.

4.3 Results

4.3.1 Performance and Degradation Mechanisms for Module Variants under Two Exposures

The normalized maximum power extracted from I-V curves (${}^{n}P_{mp,IV}$) for brand A minimodules after each accelerated exposure is shown in Fig. 4.1. The x-axis is the ${}^{n}P_{mp,IV}$ at the last exposure step, and the y-axis is the module variant. The two blue dashed lines mark 1 ± 0.005. The red circles mark the average value for each module variant, and the purple bar is the 95% confidence interval (CI). In the case that a value is not within the range indicated by the purple bar, the average value of the corresponding module variant is said to have a statistically significant difference from the compared value at the significance level of 0.05. The black bar indicates the 83.4% confidence interval (CI). If two of such bars have no overlap, then their corresponding averages have a statistically significant difference at the significance level of 0.05. Comparing these black bars provides a way to visualize the null hypothesis two-sample t-test results of comparing the average values of two groups[96–98].

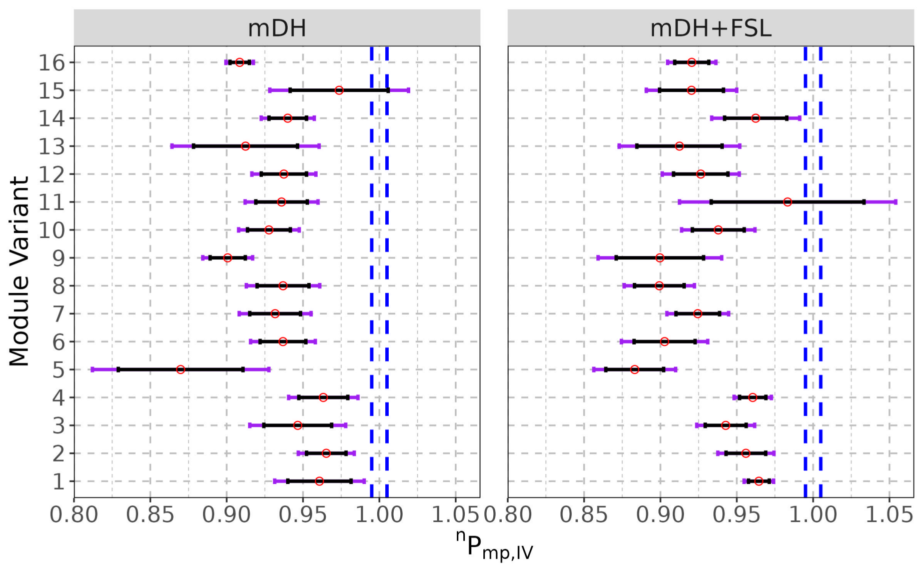

Figure 4.1. $^{n}P_{mp,IV}$ for brand A minimodules after each accelerated exposure.

The results of $^{n}R_{s,IV}$, $^{n}I_{sc,IV}$, and $^{n}P_{mp,PIV}$ for brand A minimodules after each accelerated exposure are presented in Fig. 4.2, Fig. 4.3, and Fig. 4.4, respectively. These three electrical features are not only overall electrical parameters, but they are also closely related to specific degradation mechanisms. The increase in $^{n}R_{s,IV}$ indicates interconnection corrosion, the decrease in $^{n}I_{sc,IV}$ correlates to encapsulant discoloration, and the reduction of $^{n}P_{mp,PIV}$ reveals easier recombination after exposure. The association of these features to their degradation mechanisms is also based on understanding how PV modules should degrade under our specific accelerated exposure conditions. While the amount of change in each mechanism feature is not linearly proportional to its contributed power loss, a significant change generally indicates the activated degradation mechanism. The normalized electrical feature results of ${}^{n}P_{mp,IV}$, ${}^{n}R_{s,IV}$, ${}^{n}I_{sc}, IV$, and ${}^{n}P_{mp,PIV}$ for brand B minimodules after each accelerated exposure are presented in Fig. 4.5. The average and standard error (SE) of the change in each normalized electrical feature for both brands under each accelerated exposure are listed in Table 4.1.

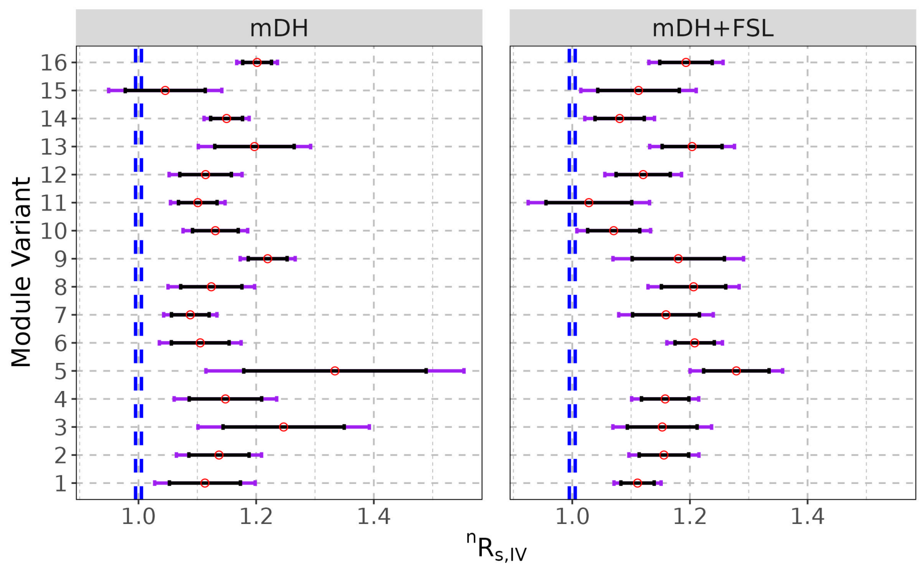

Figure 4.2. ${}^{n}R_{s,IV}$ for brand A minimodules after each accelerated exposure.

4.3.2 Pairwise Features Correlation across Module Variants and Exposures

The pairwise Pearson correlation coefficient (PCC) was calculated using six selected normalized features after each accelerated exposure for different data subsets. Fig. 4.6 shows the pairwise correlation information, including the raw data, the distribution, and the pairwise correlation coefficients using the data containing all observations and

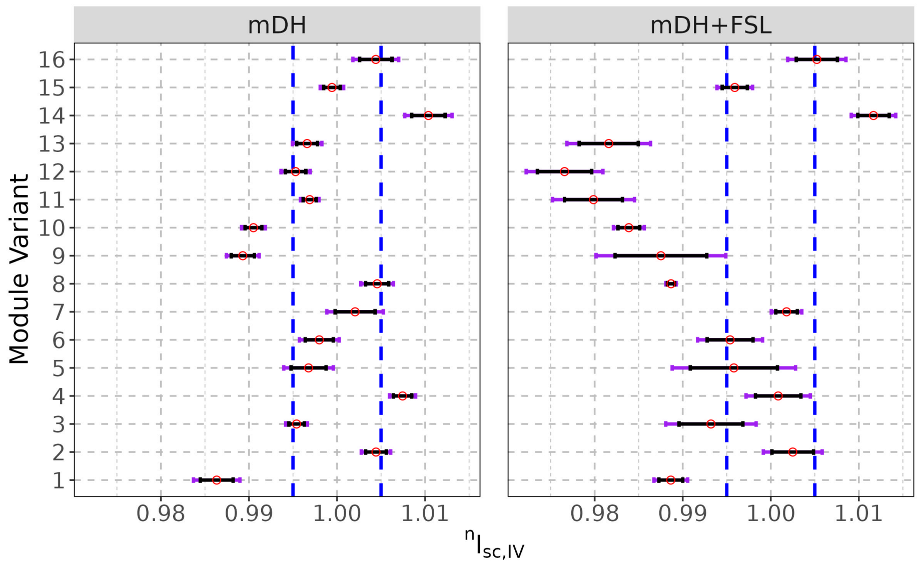

Figure 4.3. $^{n}I_{sc,IV}$ for brand A minimodules after each accelerated exposure.

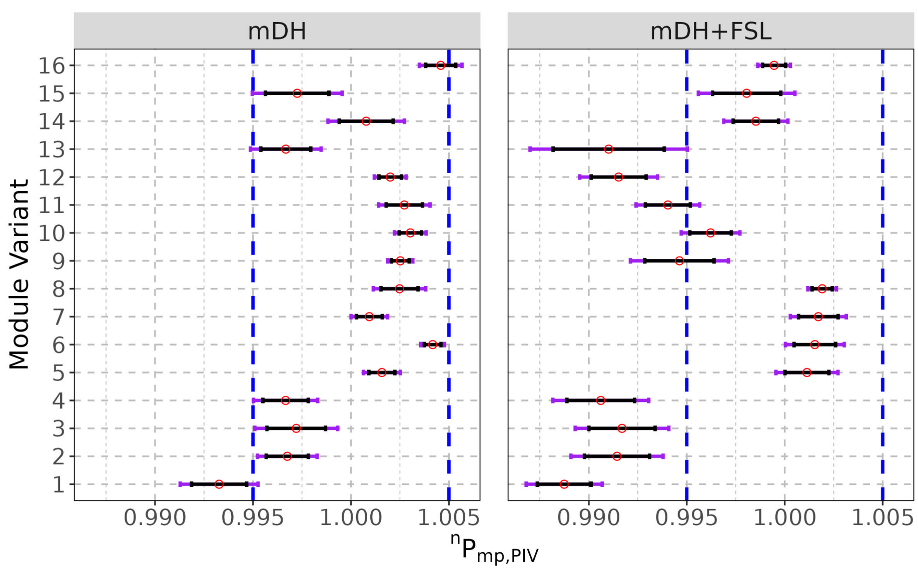

Figure 4.4. $^{n}P_{mp,PIV}$ for brand A minimodules after each accelerated exposure.

observations of each accelerated exposure. We denote the correlation coefficient between $^{n}P_{mp,IV}$ and $^{n}R_{s,IV}$ as $r(^{n}P_{mp,IV}, ^{n}R_{s,IV})$, and the correlation coefficient between $^{n}F_{sd,EL@I_o}$ and $^{n}F_{sd,PL@OC}$ as $r(^{n}F_{sd,EL@I_o}, ^{n}F_{sd,PL@OC})$. Fig. 4.7 and Fig. 4.8 show the $r(^{n}P_{mp,IV}, ^{n}R_{s,IV})$ and $r(^{n}F_{sd,EL@I_o}, ^{n}F_{sd,PL@OC})$ under different subsetting conditions,

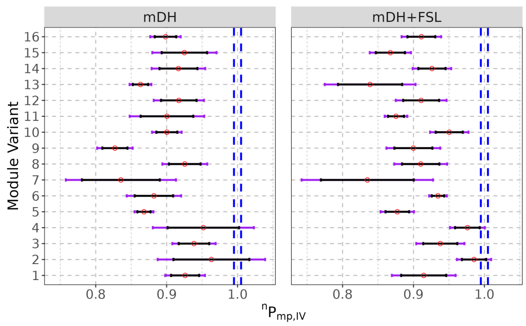

(a) $^{n}P_{mp,IV}$.

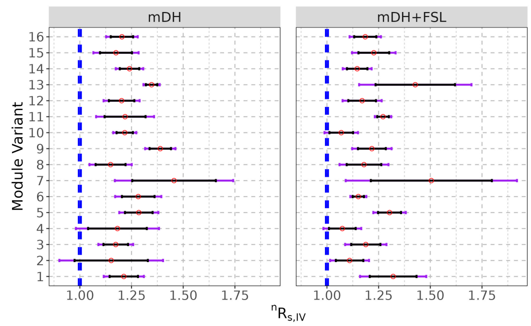

(b) $^{n}R_{s,IV}$.

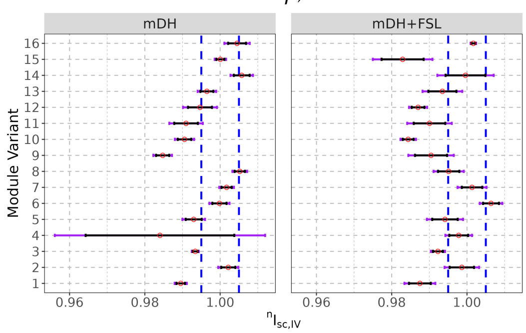

(c) $^{n}I_{sc,IV}$.

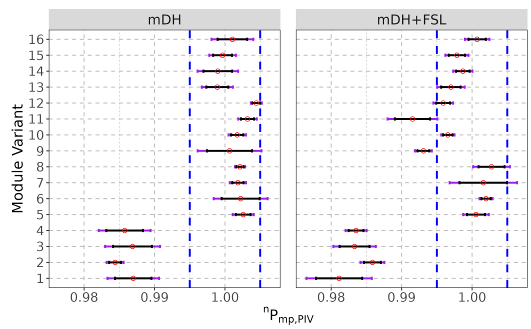

(d) $^{n}P_{mp,PIV}$.

Figure 4.5. Normalized electrical feature results, including $^{n}P_{mp,IV}$, $^{n}R_{s,IV}$, $^{n}I_{sc,IV}$, and $^{n}P_{mp,PIV}$, for brand B minimodules after each accelerated exposure.

Table 4.1. The average and standard error (SE) of the change in the four normalized electrical features, including $^{n}P_{mp,IV}$, $^{n}I_{sc,IV}$, $^{n}R_{s,IV}$, and $^{n}P_{mp,PIV}$, for brands A and B under each accelerated exposure.

Brand	Exposure	Average ± SE (%)			
		$^{n}P_{mp,IV}$	$^{n}I_{sc,IV}$	$^{n}R_{s,IV}$	$^{n}P_{mp,PIV}$
A	mDH	-6.59 ± 0.42	-0.14 ± 0.06	+15.46 ± 1.30	+0.02 ± 0.03
A	mDH+FSL	-6.93 ± 0.47	-0.72 ± 0.10	+14.82 ± 1.10	-0.41 ± 0.05
B	mDH	-9.78 ± 0.64	-0.42 ± 0.11	+24.49 ± 1.85	-0.23 ± 0.07
B	mDH+FSL	-8.87 ± 0.59	-0.60 ± 0.08	+21.32 ± 1.87	-0.58 ± 0.07

including exposures, encapsulant materials, module architectures, cell types, and module brands, respectively.

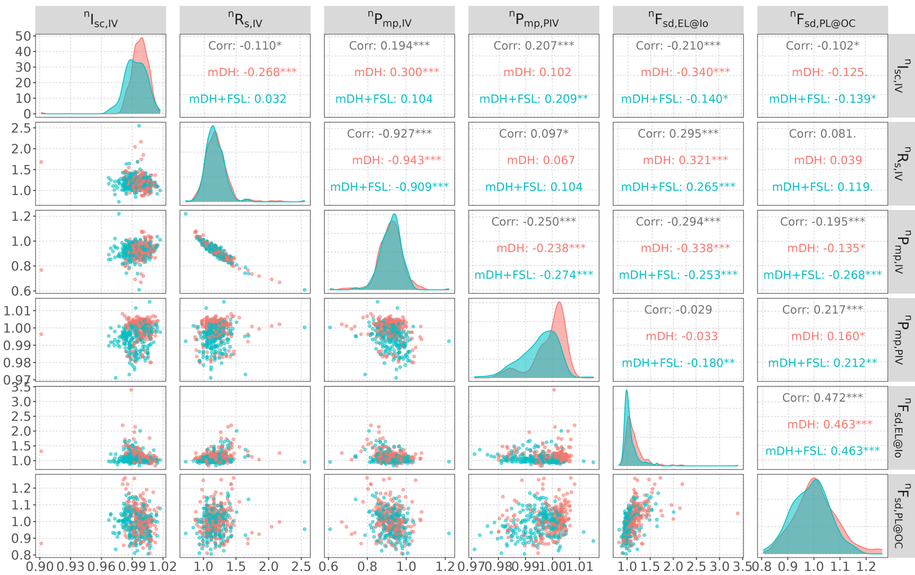

Figure 4.6. The pairwise correlation for the six selected normalized features after each accelerated exposure.

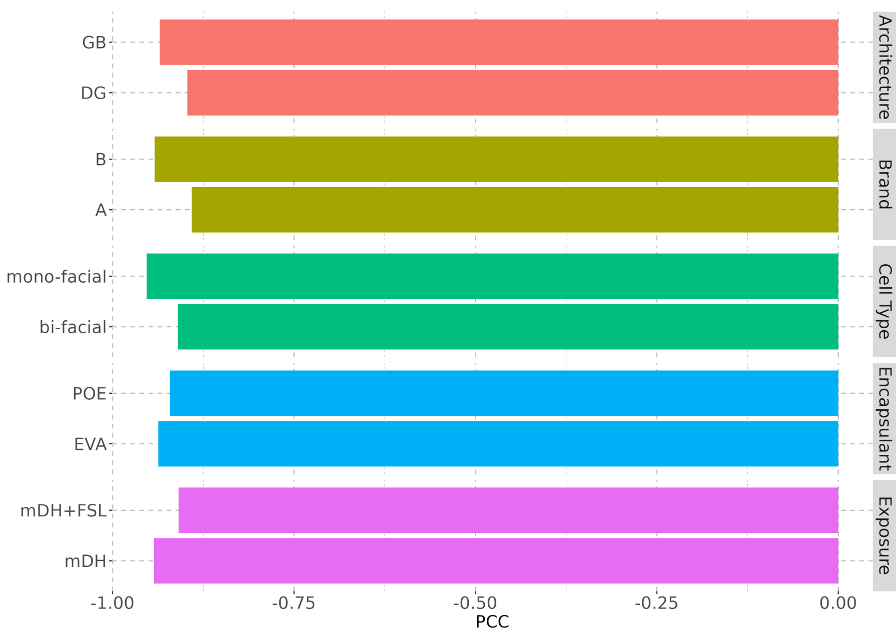

Figure 4.7. $r({}^{n}P_{mp,IV}, {}^{n}R_{s,IV})$ using different subsetting conditions.

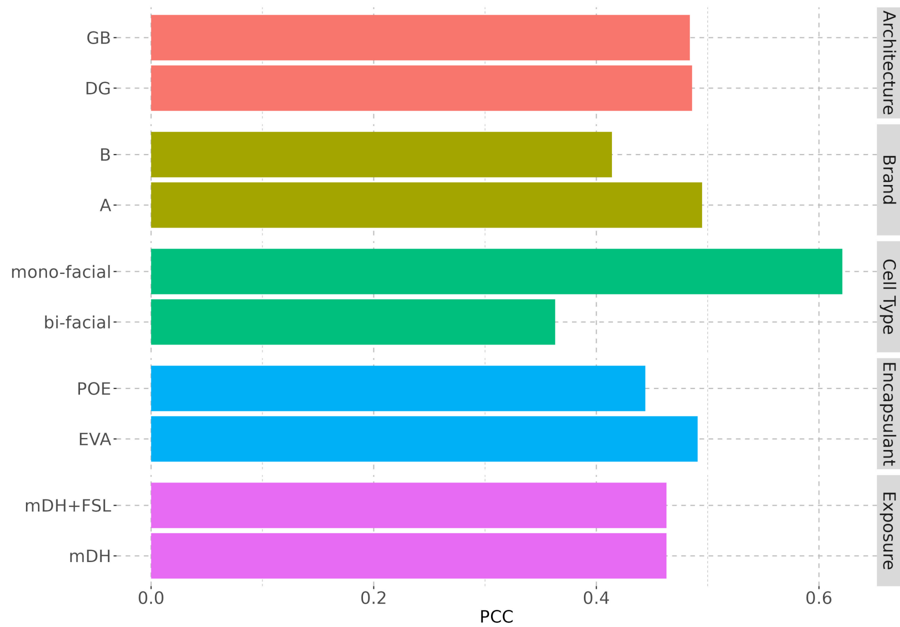

Figure 4.8. $r({}^{n}F_{sd,EL@I_o}, {}^{n}F_{sd,PL@OC})$ using different subsetting conditions.

4.3.3 Hierarchical Clustering of Principal Components to Study Dependency

The proportion of data variance explained by each principal component is shown in Fig. 4.9 for brands A and B. The first three principal components explain 80.0% data variance for brands A and B. They were used as input for the hierarchical clustering algorithm. The resulting dendrograms for brands A and B are shown in Fig. 4.10. Cutting the dendrogram at the height of 19.5 for both brands resulted in three clusters.

For the result of brand A minimodules, Fig. 4.11 shows the clustered points using the principal component basis with the variable vector. Table 4.2 lists the number of observations in each cluster under different subsetting conditions. Fig. 4.12 and Table 4.3 show corresponding results for brand B minimodules. Table 4.4 lists the medium value for ${}^{n}F_{sd,EL@I_o}$, ${}^{n}P_{mp,IV}$, and ${}^{n}I_{sc,IV}$ for each cluster of each brand to associate the degree of degradation to each cluster. These three features are selected based on the importance of the variable to each principal component.

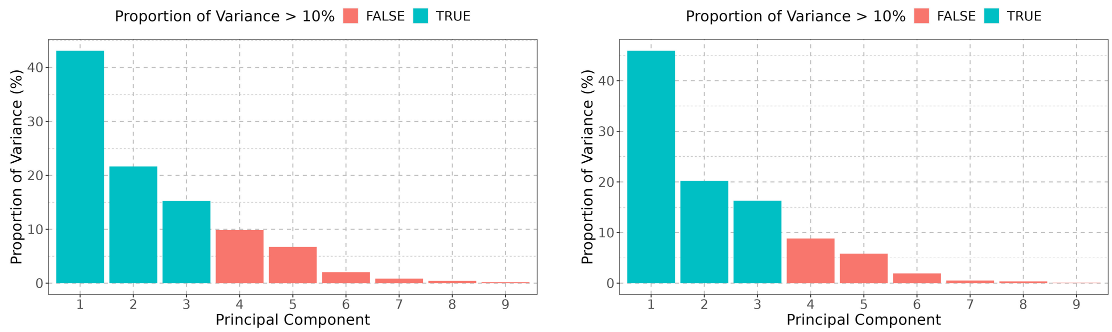

(a) Brand A. (b) Brand B.

Figure 4.9. The proportion of data variance explained by each principal component for brands A and B.

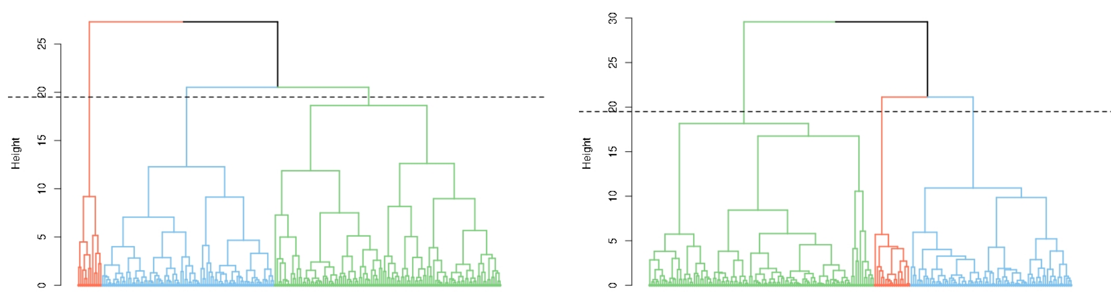

(a) Brand A. (b) Brand B.

Figure 4.10. The hierarchical clustering dendrograms for brands A and B. Three clusters are obtained for each brand by cutting at the height of 19.5.

Table 4.2. The number of observations for each cluster under different subsetting conditions, including encapsulant materials, module architectures, and cell types after each accelerated exposure for brand A.

Cluster ID	mDH						mDH+FSL					
	Encapsulant		Architecture		Cell Type		Encapsulant		Architecture		Cell Type	
	EVA	POE	DG	GB	Monofacial	Bifacial	EVA	POE	DG	GB	Monofacial	Bifacial
1	28	31	28	31	24	35	29	25	17	37	30	24
2	15	19	25	9	20	14	26	26	38	14	23	29
3	9	3	3	9	7	5	0	0	0	0	0	0

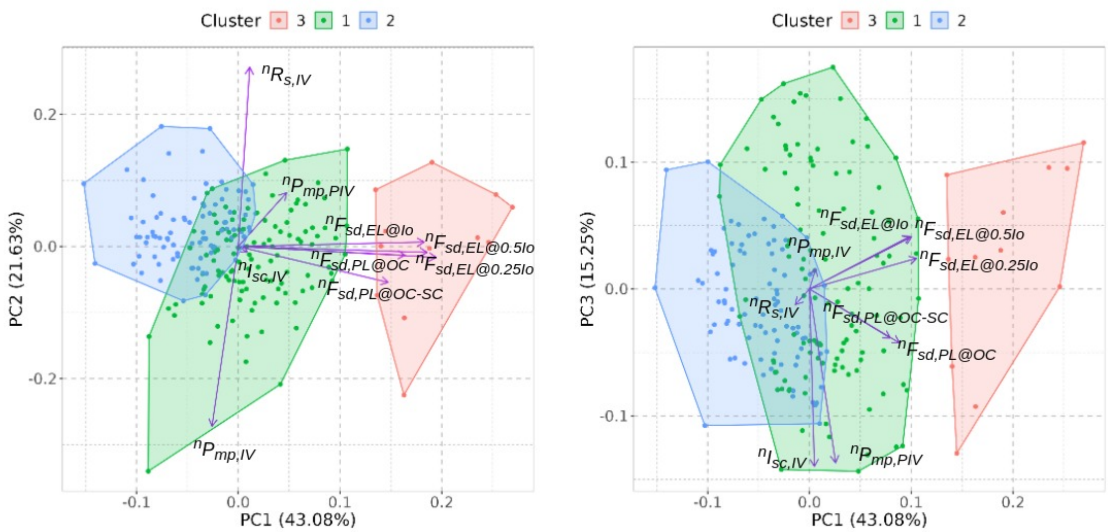

(a) PC2 versus PC1. (b) PC3 versus PC1.

Figure 4.11. Principal component scores for brand A of each input observations, colored by the clusters identified by the hierarchical clustering result. The arrow displays the loading of each variable, of which the projected length can be understood as the weight for each original variable when calculating the principal component.

Table 4.3. The number of observations for each cluster under different subsetting conditions, including encapsulant materials, module architectures, and cell types after each accelerated exposure for brand B.

Cluster ID	mDH						mDH+FSL					
	Encapsulant		Architecture		Cell Type		Encapsulant		Architecture		Cell Type	
	EVA	POE	DG	GB	Monofacial	Bifacial	EVA	POE	DG	GB	Monofacial	Bifacial
1	22	20	16	26	29	13	18	16	15	19	26	8
2	14	33	30	17	18	29	23	36	38	21	24	35
3	8	1	1	8	6	3	7	1	0	8	4	4

Table 4.4. The medium value of selected features of each cluster for brands A and B.

Cluster ID	Brand A			Brand B		
	${}^{n}F_{sd,EL@I_o}$	${}^{n}P_{mp,IV}$	${}^{n}I_{sc,IV}$	${}^{n}F_{sd,EL@I_o}$	${}^{n}P_{mp,IV}$	${}^{n}I_{sc,IV}$
1	1.05	0.940	0.997	1.19	0.900	0.992
2	0.979	0.926	0.998	1.03	0.927	1.00
3	1.28	0.918	0.997	1.65	0.859	0.986

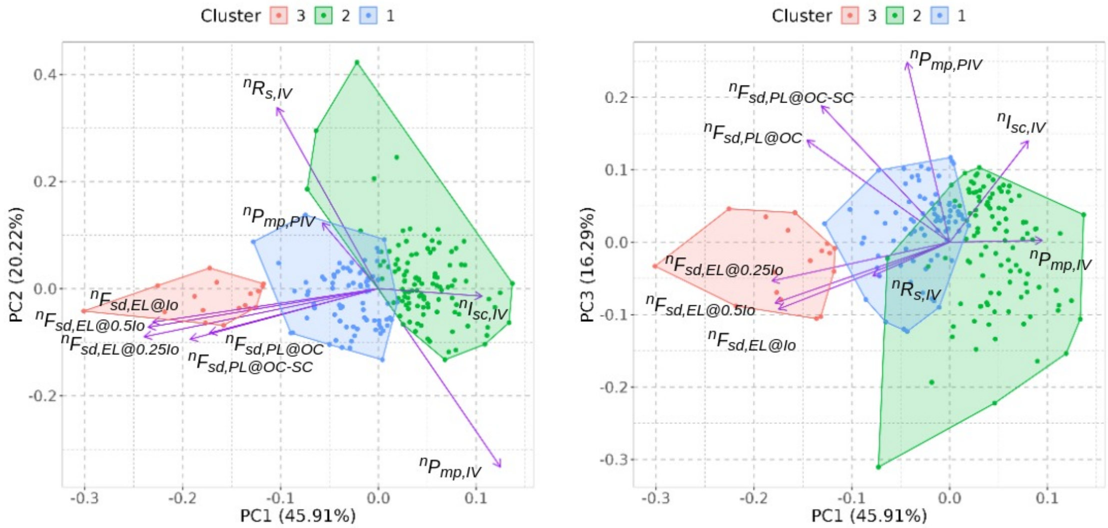

(a) PC2 versus PC1.

(b) PC3 versus PC1.

Figure 4.12. Principal component scores for brand B of each input observations, colored by the clusters identified by the hierarchical clustering result. The arrow displays the loading of each variable, of which the projected length can be understood as the weight for each original variable when calculating the principal component.

4.4 Discussion

4.4.1 Study Protocol for Parametric Variations across Module Variants and Exposures

Solar technology and products have changed rapidly in recent years, bringing significant challenges to reliability studies. In most studies comparing the PV module reliability performance, only average characterization results have been reported, ignoring confidence intervals caused by sample and measurement uncertainties. Most studies evaluated only the P_{mp} and paid less attention to features related to specific degradation mechanisms. A sufficient number of samples are essential to evaluate the statistical significance of the results. In our study, eight cells laminated in two minimodules were used to compare module variants from each brand under each accelerated exposure.

Such sample size allows us to use the 83.4% confidence interval (CI) to visualize the null hypothesis two-sample t-test results for comparing two module variants. Whether their average performance has a statistically significant difference at the significance level of 0.05 is indicated by the overlapping of their confidence intervals. Our study evaluated sixteen module variants of two brands, A and B, under two different accelerated exposures: mDH and mDH+FSL. The sixteen module variants take different encapsulant materials (EVA and POE), encapsulant types, cell types, and module architectures (GB and DG) into account. The detailed specifications of the sixteen module variants are listed in Table 3.1. The two accelerated exposures were chosen to evaluate the module reliability against high temperature and humid conditions, with or without operating solar cells. It is worth noting that the minimodules tend to amplify the degree of degradation due to the reduced size compared to the commercial PV module, which usually contains about 60 cells or more.

4.4.2 Performance and Degradation Mechanism Features

${}^{n}P_{mp,IV}$ was chosen as an indicator for the overall degradation since the power output decides the performance of PV modules. In addition, ${}^{n}R_{s,IV}$, ${}^{n}I_{sc,IV}$ and ${}^{n}P_{mp,PIV}$ were selected as indicators for different degradation mechanisms. R_s is expected to increase when the solar cell experiences interconnection corrosion. The reduction in I_{sc} is generally linked to transmittance loss in the encapsulant layer due to discoloration or encapsulant delamination which influences the optical coupling at the interface. On the other hand, a very large R_s can also lead to a decrease in I_{sc}, but such a high value is not typical in practice. ${}^{n}P_{mp,PIV}$ captures the change in recombination behavior. Easier recombination leads to a decrease in ${}^{n}P_{mp,PIV}$. EL reveals the spatial information of the solar cell through light emission under current excitation, while PL reveals the spatial information through light emission under light excitation. The standard deviation is an indicator for measuring signal uniformity. If more local defects are presented in the solar cell and detectable under an excitation mechanism, the standard deviation of the corresponding image will increase. Near-uniformly added or subtracted signal has a minor influence on the standard deviation of an image. The electrical status of a solar cell when measuring EL is similar to that of measuring I-V curves, considering the forwarding current in common. The electrical status for measuring the open-circuit PL is similar to that of measuring $Suns$-V_{oc}. It is worth mentioning that the features selected in this study can also be obtained from the outdoor timeseries I-V curves through modeling methods[8, 54]. Thus, it provides common variables for data-driven methods to compare the degradation behaviors of PV modules under indoor accelerated and outdoor exposures.

4.4.3 Correlation of Performance and Mechanisms Features and Between Mechanisms

Comparing the quantitative change of different electrical features related to specific degradation mechanisms helps us understand the reasons behind power loss. Studying the correlation between power loss and degradation mechanism features can give clues on whether a specific degradation mechanism is strongly associated or not. In Fig. 4.6, ${}^{n}P_{mp,IV}$ and ${}^{n}R_{s,IV}$ are found to have a highly negative correlation, and this correlation coefficient is more negative for mDH than mDH+FSL. Considering that our exposure conditions contain high humidity and temperature rather than mechanical stress, such a correlation indicates that power loss is closely related to interconnection corrosion.

However, strong correlations between mechanism features and power are necessary but not enough to conclude the dominant mechanism of power loss, especially when multiple features all correlate to the power. In addition, ${}^{n}F_{sd,EL@I_o}$ and ${}^{n}F_{sd,PL@OC}$ are found to have a moderate positive correlation as shown in Fig. 4.6. The defects detected in $PL@OC$ are also detectable in $EL@I_o$, which is the physical foundation of a moderate positive correlation between the standard deviations from both images. However, it should be noted that not all correlations between variables related to the degradation mechanisms will have a physical meaning. For example, our PIV curves were converted from $Suns$-V_{oc} curves using a constant I_{sc}. Therefore, no characteristic features extracted from the PIV curve should be physically influenced by the I_{sc} value extracted from the I-V curve. The simultaneous changing effect could cause their statistical correlation, but both mechanism variables are physically independent of each other. All three degradation mechanisms features chosen in the study, ${}^{n}R_{s,IV}$, ${}^{n}I_{sc,IV}$, and ${}^{n}P_{mp,PIV}$ are physically relatively independent of each other.

4.4.4 Rank Ordering of Variant Factors on Degradation and Performance

This section discusses the differences in the reliability performance of the sixteen module variants of brand A minimodules under each accelerated exposure. From Fig. 4.1, under mDH, the average ${}^{n}P_{mp,IV}$ drop for module variants 1, 2, 4, and 15 is lower than 5%, and these module variants are considered to be stable. Among these stable module variants, module variant 1 has the lowest lower boundary of the 83.4% CI, which is the criteria to decide the module variant with a significantly greater average power loss. Module variants 5, 9, and 16 under mDH are observed to have a significantly greater average power loss than these stable module variants. A similar analysis is conducted for module variants under mDH+FSL exposure. Module variants 1, 2, 4, 11, and 14 are found to have an average ${}^{n}P_{mp,IV}$ drop that is less than 5%. The lower boundary of the 83.4% CI of module variant 11 is the lowest, which is used as the deciding criteria. Then module variants 5, 6, 8, 9, and 16 are identified to have a significantly greater average power loss. Therefore, module variants 5, 9, and 16 perform relatively poorly under both accelerated exposures. Both module variants 5 and 9 are EVA+GB modules with the opaque rear encapsulant, and module variant 16 is the bifacial POE+DG modules. Module variants 1, 2, and 4 are identified to be stable under both exposures, and they are EVA+GB, EVA+DG and POE+DG modules with UV-Cutoff rear encapsulant, respectively.

From the results of ${}^{n}R_{s,IV}$, ${}^{n}I_{sc,IV}$, and ${}^{n}P_{mp,PIV}$, shown in Fig. 4.2, Fig. 4.3, and Fig. 4.4, respectively, ${}^{n}R_{s,IV}$ has changed much more significantly than the other two features. The average change in ${}^{n}R_{s,IV}$ is much higher than that of ${}^{n}I_{sc,IV}$ and ${}^{n}P_{pm,PIV}$ for brand A modules under both accelerated exposures as shown in Table 4.1. While more changes occur in ${}^{n}I_{sc,IV}$ and ${}^{n}P_{mp,PIV}$ for modules under mDH+FSL than mDH, it is still much smaller than the change in ${}^{n}R_{s,IV}$. The difference in the amount of change in ${}^{n}R_{s,IV}$ averaged across all module variants is minor between exposures, although mDH+FSL only has 2/3 of the total exposure time under mDH. Therefore, the minor difference can be related to the continuous aging effect of the degradation product obtained under mDH. Moreover, the average power loss among all sixteen module variants is similar for both exposures, as 6.59% for mDH and 6.93% for mDH+FSL. However, the comparable power loss between exposures is not general across all module variants. Module variants 6, 8, 11, 14, and 15 have a difference of larger than 2% in the average ${}^{n}P_{mp,IV}$ between exposures. Several module variants have a relatively higher average

${}^{n}R_{s,IV}$ shown in Fig. 4.2. Under mDH, module variants 3, 5, 9, 13, and 16 have an average ${}^{n}R_{s,IV}$ increase of over 19%, and under mDH+FSL, module variants 5, 6, 8, 9, 13, and 16 have an average ${}^{n}R_{s,IV}$ increase of over 18%. These identified module variants with a more significant ${}^{n}R_{s,IV}$ increase include all module variants that are identified to have a significantly greater average power loss. Furthermore, none of the module variants with an average power loss of less than 5% are identified in the module variants with a relatively greater ${}^{n}R_{s,IV}$ increase, which is evidence that corrosion dominates power loss for modules under both defined exposures. One more piece of evidence is the negative correlation coefficient of -0.891 between ${}^{n}P_{mp,IV}$ and ${}^{n}R_{s,IV}$ for brand A minimodules considering both exposures, as shown in Fig. 4.7. The averages of ${}^{n}I_{sc,IV}$ for most module variants are within the range of 1 ± 0.005 under mDH as shown in Fig. 4.3. The largest ${}^{n}I_{sc,IV}$ drop under mDH occurs in module variant 1 at 1.37%. Module variant 1 is for the EVA+GB monofacial modules with UV-Cutoff rear encapsulant. Under mDH+FSL, more module variants show a slight ${}^{n}I_{sc,IV}$ decrease. The most significant average drop under mDH+FSL occurs in module variant 12 at 2.34%. Module variant 12 is for the POE+DG modules with opaque rear encapsulant. In addition, module variant 8 which has similar packaging as module variant 12, also shows a significant ${}^{n}I_{sc,IV}$ drop. From the ${}^{n}P_{mp,PIV}$ results shown in Fig. 4.4, the recombination behavior can be considered as unchanged for most module variants under both exposures since the average change is within 1%, except module variant 1 which has a decrease in ${}^{n}P_{mp,PIV}$ of 1.13% under mDH+FSL.

The PCA result of brand A minimodules using the centered and unit variance scaled data as the input is shown in Fig. 4.11. From Fig. 4.11, the first principal component (PC_1) is found to represent most image features. PC_2 is mainly influenced by ${}^{n}R_{s,IV}$ and ${}^{n}P_{mp,IV}$. The opposite directions of these two feature loadings agree with their highly negative correlation coefficient. Moreover, PC_3 is mainly influenced by ${}^{n}I_{sc,IV}$ and ${}^{n}P_{mp,PIV}$ with some ability to separate features obtained from EL and PL. The first three principal components explain 80.0% of total data variance, as shown in Fig. 4.9. Using the first three principal components obtained from the scaled and centered data as the input to the clustering algorithm, the resulting clusters avoid influences from the variance difference of selected features and the selection of correlated features. Based on the dendrogram shown in Fig. 4.10 for brand A, the two large clusters are more similar to each other than the tiny cluster in the red color. Table 4.4 lists the median value for ${}^{n}F_{sd,EL@I_o}$, ${}^{n}P_{mp,IV}$, and ${}^{n}I_{sc,IV}$ to associate the degree of degradation to each cluster. Cluster 3 has the most significant power loss and ${}^{n}F_{sd,EL@I_o}$ increase. Therefore, it has the highest degree of degradation. Cluster 1 has the least power loss with a slightly increased ${}^{n}F_{sd,EL@I_o}$. Cluster 2 has the smallest ${}^{n}F_{sd,EL@I_o}$ but a slightly greater power loss than that of cluster 1. These three features are selected based on each principal component, and the comparison of their medium values agrees with the similarity found in the dendrogram.

Table 4.2 reveals the dependency of these clusters on the module specifications. Cluster 3 is only made of samples under mDH, and it has 50% more EVA samples than POE, and 50% more GB samples than DG. However, cluster 3 has a smaller number of observations. Therefore, the revealed dependency does not indicate average performance differences between EVA and POE or DG and GB. A better interpretation is that a few samples under the category of EVA or GB have a higher risk of performing like outliers than modules of its counterpart. Further investigation finds that six samples of cluster 3 belong to module variants 5 and 9, which are EVA+GB with opaque rear encapsulant modules having significant power loss. In addition, cluster 2 is found to have 47.1% more DG samples than GB samples under mDH. Under mDH+FSL, cluster 1 has 37.0% more GB samples, and cluster 2 has 46.2% more DG samples. Therefore, the unsupervised hierarchical clustering result finds that the identified clusters of brand A minimodules under accelerated exposures mainly depend on the module architecture rather than the encapsulant material or the cell type.

4.4.5 Impact of Manufacturing Variability on Degradation and Performance: Two Brands

This section discusses the degradation performance of brand B minimodules and compares the results to brand A. From the $^{n}P_{mp,IV}$ result shown in Fig. 4.5, module variants 2 and 4 have an average $^{n}P_{mp,IV}$ drop of less than 5% under mDH. Module variant 4 has the lowest lower boundary of the 83.4% confidence interval of $^{n}P_{mp,IV}$, which is used as the criteria to identify that module variants 5, 7, 9, and 13 have a significantly greater average power loss. These four module variants are found to have an average $^{n}R_{s,IV}$ increased by 25%. Under mDH+FSL, module variants 2, 4, and 10 have an average $^{n}P_{mp,IV}$ drop of less than 5%. Module variant 10 has the lowest lower 83.4% CI boundary and is used to identify the module variant with a significantly greater average power loss, which was identified as module variants 5, 7, 9, 11, 13, 15, and 16. Among them, module variants 5, 7, 11, and 13 have an average $^{n}R_{s,IV}$ increase of over 25%, and the rest have an average increase of over 18.5%. Module variants 2 and 4 are identified as the stable module variants, and module variants 5 and 9 as the relatively unstable module variants under mDH in both brands. Under mDH+FSL, module variants 2 and 4 are identified in the stable group, and module variants 5, 9, and 16 are identified in the unstable group in both brands. However, compared to the results of brand A, there are more GB module variants, which have an odd module variant ID, falling into the relatively unstable group in brand B modules.

The average amount of change in ${}^{n}P_{mp,IV}$ and ${}^{n}R_{s,IV}$ is greater for brand B modules than for brand A under each exposure, as shown in Table 4.1, indicating reliability performances differences due to manufacturing (lamination, soldering, and cell storage) since the packaging materials used are the same. The change in ${}^{n}R_{s,IV}$ is greater than that of ${}^{n}I_{sc,IV}$ and ${}^{n}P_{mp,PIV}$, and the change in ${}^{n}I_{sc,IV}$ and ${}^{n}P_{mp,PIV}$ is greater under mDH+FSL than that under mDH, which are consistent with the findings for brand A modules. Therefore, interconnection corrosion is again identified as the dominant degradation mechanism contributing to the power loss of brand B modules. The correlation coefficient between ${}^{n}P_{mp,IV}$ and ${}^{n}R_{s,IV}$ is even more negative for brand B than that of brand A, as shown in Fig. 4.7. We also find the correlation coefficient between ${}^{n}F_{sd,EL@I_o}$ and ${}^{n}F_{sd,PL@OC}$ has a difference between the two cell types, as shown in Fig. 4.8. By calculating $r({}^{n}F_{sd,EL@I_o}, {}^{n}F_{sd,PL@OC})$ using the data of each brand, each cell type, and each accelerated exposure, a more positive correlation coefficient for modules with monofacial cells is found to be mainly present in brand B modules, as shown in the results listed in Table 4.5.

The PCA results of brand B modules are shown in Fig. 4.12. The influence of different features on each principal component for brand B modules is similar to that of brand A. However, there is a slightly greater influence from ${}^{n}I_{sc,IV}$ to PC_1 and from PL image features to PC_3. The data variance explained by the first three principal components is also 80% of the total as shown in Fig. 4.9. In the dendrogram shown in Fig. 4.10, three clusters can be obtained by cutting at the height of 19.5. The small cluster is more similar to one large cluster colored in blue than the other large cluster. However, in brand A,

Table 4.5. The correlation coefficient between ${}^{n}F_{sd,EL@I_o}$ and ${}^{n}F_{sd,PL@OC}$ for each brand, each cell type, and under each accelerated exposure.

Brand	Exposure	Cell Type	$r({}^{n}F_{sd,EL@I_o}, {}^{n}F_{sd,PL@OC})$
A	mDH	bifacial	0.584
A	mDH	monofacial	0.541
A	mDH+FSL	bifacial	0.554
A	mDH+FSL	monofacial	0.349
B	mDH	bifacial	0.391
B	mDH	monofacial	0.512
B	mDH+FSL	bifacial	0.313
B	mDH+FSL	monofacial	0.546

the two large clusters are from the same branch and are more similar to each other. Therefore, the reliability performance of most brand A minimodules is more consistent than that of brand B. Based on the median feature value listed in Table 4.4 for brand B modules, cluster 3 is found to have the highest level of degradation indicated by the pronounced ${}^{n}P_{mp,IV}$ drop and ${}^{n}F_{sd,EL@I_o}$ increase, and cluster 2 has the slightest degree of degradation.

From Table 4.3, brand B results have more complex dependencies for the cluster separation than that of brand A. Under mDH, most observations under cluster 3 are EVA samples or GB samples, which is similar to brand A. However, cluster 3 also has 25% more samples that use monofacial cells than bifacial cells. Under mDH, the most significant difference in the number of samples for cluster 2 occurs between encapsulant materials at 40.4%. In addition, apparent differences are also presented in different module architectures and cell types for cluster 2 under mDH. Differences between module architectures and cell types are also shown in cluster 1 under mDH, and the most prominent difference occurs between cell types at 38.1%. Under mDH+FSL, we find cluster 3 has more EVA samples and more GB samples than their counterparts. Cluster 1 has 52.9%

more samples with monofacial cells than bifacial cells. The most noticeable difference in cluster 2 under mDH+FSL occurs between module architectures, but it is only 28.8% due to many observations in cluster 2. Comparing Table 4.2 and Table 4.3, the difference in reliability performance caused by cell types and encapsulant materials could be reduced by a more strict manufacturing quality control. The difference between cell types shown in brand B modules could be related to the storage duration and the compatibility with the manual soldering process. For brand B modules, set #1 was made earlier than set #2, and set #3 was made earlier than set #4. Set #1 and #3 use monofacial cells, and set #2 and #4 use bifacial cells. Although all solar cells were carefully stored in a dark chamber with nitrogen flow, some cell discoloration was noticed when fabricating sets #3 and #4 modules.

4.5 Conclusions

By comparing the characterization results of sixteen module variants of two brands under the accelerated exposure of mDH and mDH+FSL of up to 2,520 hours, module variants 2 and 4, which are DG modules with the UV-Cutoff rear encapsulant, are identified to experience an average power loss of less than 5%. Module variants 5 and 9, which are EVA+GB modules with the opaque rear encapsulant, are identified to have a more significant average power loss than that of the module variants in the stable group and are considered as stable module variants. The power loss under both accelerated exposures is mainly due to interconnection corrosion indicated by the increase in series resistance, which is much higher than the change in ${}^{n}I_{sc,IV}$ and ${}^{n}P_{mp,PIV}$ after each exposure, the highly negative correlation coefficient between ${}^{n}P_{mp,IV}$ and ${}^{n}R_{s,IV}$, and the opposite directions of the feature loadings of $^nP_{mp,IV}$ and $^nR_{s,IV}$ in the PCA result. With the same exposure hours, mDH+FSL leads to more changes in $^nI_{sc,IV}$ and $^nP_{mp,PIV}$ than mDH but similar changes in $^nP_{mp,IV}$ and $^nR_{s,IV}$ on average for both brands. The manufacturing process is found to influence the reliability performance. Brand A modules, which have more strict quality control in manufacturing, experience less degradation than brand B in power and series resistance. The unsupervised hierarchical clustering result shows that the performance of most brand A modules only has a dependency on the module architecture, which is GB or DG. However, the cluster of brand B modules shows differences in the number of observations between encapsulant materials, module architectures, and cell types. Therefore, different manufacturing processes could amplify the differences in the reliability performance caused by encapsulant materials and cell types under our accelerated exposure conditions.

5 Outdoor Exposure Study of Module Variants using Timeseries Data

Title to submit: **Outdoor Degradation Study Using I-V, P_{mp} Timeseries Data and $Suns$-V_{oc} Analysis of PERC Minimodules with Differing Encapsulants and Module Architectures**

The degradation of photovoltaic (PV) modules depends on their interactions with environmental stressors. Due to the rise of bifacial PV modules in the market, double glass (DG) modules and modules using polyolefin elastomer (POE) encapsulants have become strong competitors of conventional PV modules using ethylene-vinyl acetate (EVA) encapsulants with polymer backsheets. In this study, 32 minimodules of 16 module variants were fabricated with differences in encapsulant materials, rear encapsulant types, module architectures, and cell types. These modules were mounted at an outdoor testing site in the Dfa climate zone (continental, no dry season, hot summer). Their timeseries current-voltage curves, module temperature, and irradiance data measured over the time period of 1.6 years were processed to obtain predicted electrical features and power loss due to four factors using the outdoor I_{sc}-V_{oc} method implemented by the $SunsVoc$ package. The averages and confidence intervals of normalized features were calculated to identify statistically significant differences among module variants and packaging combinations in the final three months. Two module variants are found to have a significantly lower power output, and their dominant power loss factors are current mismatch power loss and uniform current power loss. Uniform current power loss, or power loss due to increased series resistance, is found to be the dominant power loss factor for most module variants. No significant differences in the power output and power loss factors are identified for the four packaging combinations considering only the encapsulant materials and module architectures.

5.1 Introduction

The performance loss rate (PLR) of PV modules is considered to be the third most important factor affecting the levelized cost of electricity[31] of solar energy. The degradation of PV modules depends on their interactions with environmental stressors. Commercial PV modules have several packaging layers to protect the internal solar cell. The different combinations of packing materials can influence the degradation behaviors of PV modules under certain exposure conditions[6, 11]. Due to the rise of bifacial PV modules, double glass (DG) PV modules and modules using POE encapsulant have become strong competitors to the conventional glass-backsheet (GB) modules using EVA encapsulant, which have dominated the market for nearly 40 years[1, 2]. However, studies comparing the performance of PV modules in the field with these different commercial packaging strategies are still lacking. The performance of modules fabricated ten to twenty years ago in early studies differ from that of modules made today due to innovation and improvement in technology. In addition, the performance of commercial

PV modules varies among brands[6]. Patel et al. studied two GB modules installed at the same site for about 20 years. The degradation rates of the two GB modules were significantly different as 1.01%/a. and 0.44%/a., respectively[2]. Studies using commercial PV modules from different manufacturers commonly lack variable control in material sources and fabrication processes. Therefore, a sufficient number of commercial PV modules are required to represent the average performance of a module type. Moreover, the comparison of PV modules in the field mainly focuses on comparing the PLR obtained by processing timeseries power data[32]. Timeseries current-voltage (I-V) curve data are less abundant than timeseries power data, but they can provide more insights into the cause of power reduction. The outdoor I_{sc}-V_{oc} method proposed by Wang et al. provides the predicted electrical features and four power loss factors at reference conditions[51], which enables a direct comparison to identify the significant contributors to the total power loss[8].

In this study, 32 four-cell minimodules of sixteen module variants were fabricated using a commercial PV module manufacturing pipeline. These minimodules were mounted on a fixed rack at an outdoor testing site. Timeseries current-voltage curves, module temperature, and irradiance data measured over the course of 1.6 years were processed to compare the degradation behaviors with the statistical significance among different module variants. The dominant contributor to the power loss of each module variant was identified by comparing the four power loss factors. Finally, the dependencies of power output and power loss factors on packaging combinations of different encapsulant materials and module architectures were investigated.

5.2 Methods

5.2.1 Outdoor PV Minimodules

In this study, minimodules were fabricated with four cells connected in series. A solar company made these minimodules using its commercial manufacturing pipeline. There were 32 minimodules mounted outdoor, with two minimodules for each module variant. These module variants have differences in encapsulant materials, rear encapsulant types, module architectures, and cell types as shown in Fig. 3.2. The encapsulant material is either ethylene vinyl acetate (EVA) or polyolefin elastomer (POE). The front encapsulant is always the transparent type, but the rear encapsulant has the choice of being transparent, UV-Cutoff, or opaque (which is also called white encapsulant). The module architecture is either glass-backsheet (GB) or double glass (DG). The solar cells in these minimodules are multicystalline silicon P-type PERC cells with five busbars. However, the cells are either monofacial or bifacial for the different module variants. The detailed specifications of each module variant are described in Table 3.1.

After the initial boron-oxygen defect stabilization process, these minimodules were mounted on a fixed tilted rack shown in Fig. 3.9 on our SDLE solar farm located in Cleveland, OH. The longitude and latitude of the installed site are -81.616° and 41.511°, respectively. According to the Köppen-Geiger climate classification system[99], this site belongs to the Dfa climate zone, where the letter "D" stands for continental, the letter "f" stands for no dry season, and the letter "a" stands for hot summer. These minimodules were arranged into three rows and eleven columns on a south-facing rack with a tilted angle of 23°. The distance from the minimodule to the ground varied between 25 to 100 cm. The outdoor exposure started in May 2020. Data for this analysis was collected until Dec 2021, ending with a total exposure time of 1.6 years. The modules are still being exposed today for future analysis.

5.2.2 The Timeseries *Pmp*, *I-V*, Meteorological Data

The electrical data, including the maximum power (P_{mp}) and the current-voltage (I-V) curve of each module, were collected by a Daystar MT5 Multi-Tracer. The time interval between the I-V curves was ten minutes with accuracies for both current and voltage within 0.1% of the full scale (5 V, 15 A). Each I-V curve had about 200 data points. Timeseries I-V features were extracted from the timeseries I-V curve. These features include P_{mp}, the current at P_{mp} (I_{mp}), the voltage at P_{mp} (V_{mp}), the short-circuit current (I_{sc}), the open-circuit voltage (V_{oc}), the series resistance (R_s), and the shunting resistance (R_{sh}). In addition, a T-type thermocouple was attached to the back of each minimodule around the center position of a solar cell to record the module temperature. The thermocouple had an accuracy of ± 0.5 °C. A Kipp Zonen CMP6 pyranometer was installed nearby for tracking the plane of array irradiance (POA). The pyranometer was installed three meters above the ground to avoid influences from ground activities, such as mowing the grass. The 32 thermocouples and the pyranometer were connected to a Campbell Sci CR1000 data logger with a data recording frequency of every one minute. The timeseries electrical data and sensor data were joined by the closest time. Observations with POA lower than 5 W/m^2 were treated as nighttime observations and were removed.

5.2.3 Outdoor Module Temperature Quality Detection & Imputation

The thermocouples for measuring the outdoor module temperature sometimes gave abnormal readings due to detachment or surrounding wildlife. The abnormal readings were detected and then replaced by imputation. Outlier detection was applied to compare around 180 readings recorded every five minutes from the 32 thermocouples using Tukey's fences method[100]. If the abnormal readings exceeded a certain percentage in a day, all readings from that day were labeled as abnormal, taking the time continuity of the thermocouple's behavior into consideration.

Five regression models were evaluated to replace the abnormal readings with predicted module temperatures. First, normal readings in each hour were partitioned into training and testing datasets using an 80:20 ratio. The adjusted R squared (adj R^2) and the testing mean absolute error (MAE) were used to evaluate the model performance. Table 5.1 describes the five models examined to predict the outdoor module temperature. The independent variables included in these models were the ambient temperature (T_{amb}), POA, the installed position, cell types, and module architectures. The installed position was specified by rows and columns, which were treated as factors in the models rather than numeric values. The best model was then implemented to replace the abnormal readings. For every abnormal reading, all normal readings within half an hour before and after were partitioned into training and testing datasets using an 80:20 split. After obtaining the model by fitting it to the training dataset, the MAE was calculated using the testing dataset. If the MAE was smaller than 2 °C, then the value predicted by the model was accepted to replace the abnormal reading.

Table 5.1. Specifications of the five regression models used to predict the module temperature readings.

ID	Expression
1	$T_{mod} = \beta_0 + \beta_1 \times T_{amb} + \beta_2 \times POA$
2	$T_{mod} = \beta_0 + \beta_1 \times T_{amb} + \beta_2 \times POA + \beta_3 \times T_{amb} \times POA$
3	$T_{mod} = \beta_0 + \beta_1 \times T_{amb} + \beta_2 \times POA + \beta_3 \times T_{amb} \times POA + \beta_4 \times row + \beta_5 \times column$
4	$T_{mod} = \beta_0 + \beta_1 \times T_{amb} + \beta_2 \times POA + \beta_3 \times T_{amb} \times POA + \beta_4 \times cell\ type + \beta_5 \times module\ architecture$
4	$T_{mod} = \beta_0 + \beta_1 \times T_{amb} + \beta_2 \times POA + \beta_3 \times T_{amb} \times POA + \beta_4 \times row + \beta_5 \times column + \beta_6 \times cell\ type + \beta_7 \times module\ architecture$

5.2.4 Data Processing: *ddiv* & *SunsVoc*

The $ddiv$ package on CRAN[49] was applied to extract I-V features from each I-V curve. These I-V features included P_{mp}, I_{mp}, V_{mp}, I_{sc}, V_{oc}, R_s, and R_{sh}. The $ddiv$ algorithm first fits a smooth spline model to the I-V curve data and then obtains 500 points from the model, which are evenly distributed in voltage from 0 V to V_{oc}. Then P_{mp}, I_{mp}, and V_{mp} are identified globally. Linear models are applied to both ends of the curve to extract the I_{sc}, V_{oc}, R_s, and R_{sh}. In addition, the algorithm uses a small moving window to avoid the highly fluctuating data sometimes showing up around the I_{sc} region.

Module temperatures, POA, and these I-V features except R_{sh} were then put into the $SunsVoc$ package[54], which uses physics-based models to predict the I-V features for a defined period, such as one week, at reference conditions. The reference conditions are 1000 W/m^2 POA and the median annual module temperature at around 1000 W/m^2 POA. These models have been proven to have excellent performance on multiple outdoor data sources[46, 51]. The $SunsVoc$ package returns four power loss factors: the uniform current power loss (ΔP_{Isc}), the recombination power loss (ΔP_{Voc}), the power loss due to R_s (ΔP_{Rs}), and the current mismatch power loss (ΔP_{Imis}). It is worth noting that values of ΔP_{Isc}, ΔP_{Voc}, and ΔP_{Imis} returned by the algorithm are changes relative to a defined initial period. However, ΔP_{Rs} is the absolute power loss due to R_s. Therefore it is always negative even at the beginning of the exposure time. The value of ΔP_{Imis}

contains all power loss that can not be explained by the other three power loss factors. Other degradation mechanisms, such as a change in R_{sh} could contribute to this kind of power loss.

5.3 Results

5.3.1 Outdoor Module Temperature

When detecting abnormal readings in the timeseries module temperature, outliers were identified by comparing the readings obtained from the 32 outdoor minimodules every five minutes. Fig. 5.1 shows the percentage of outliers each day for the outdoor minimodule sa43070. The percentage of outliers is significantly higher within the period from the 200th day to the 382nd day. A threshold of the percentage of outliers in each day was set to account for the continuity of thermocouples' abnormal behavior. If a day had a percentage of outliers higher than the threshold, then all readings of that day were labeled as abnormal. Fig. 5.2 shows the overall percentage of abnormal readings for two outdoor modules with different threshold values. These two modules have no record of thermocouple malfunctions. The red line in Fig. 5.2 marks the threshold value used in this study, which is 25%. The total percentage of abnormal readings was 6.08%, but it varied a lot among different outdoor minimodules. Fig. 5.3 shows the total percentage of abnormal readings for each outdoor minimodule, from which seven minimodules are found to have more than 5% abnormal readings with a maximum of 75.4% for sa43092.

Fig. 5.4 shows the boxplots of the adjusted R-squared (adj R^2) and the testing mean absolute error (MAE) of the five models listed in Table 5.1 using the hourly normal module temperature readings. Model 5 has the highest adj R^2 with a median value of 0.775

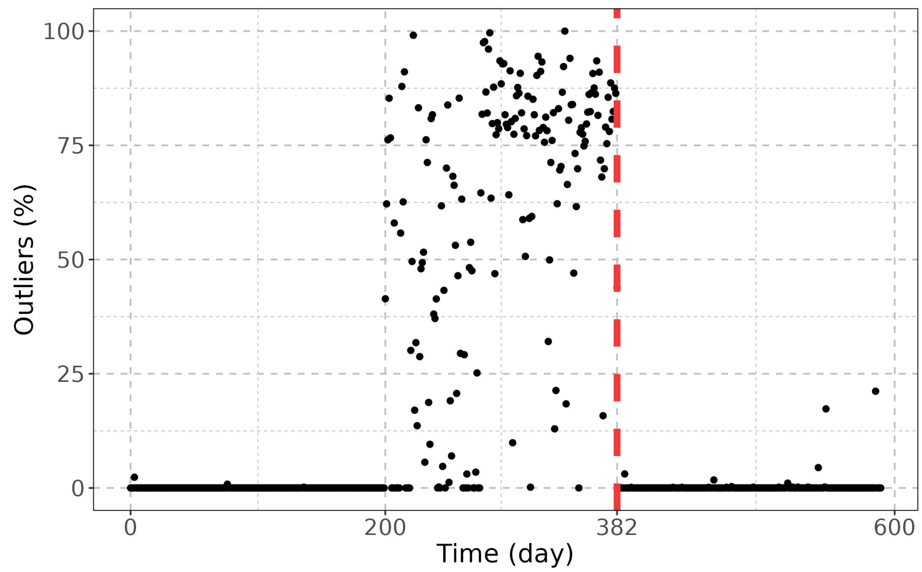

Figure 5.1. Percentage of outliers in each day for module temperature readings of the outdoor module sa43070.

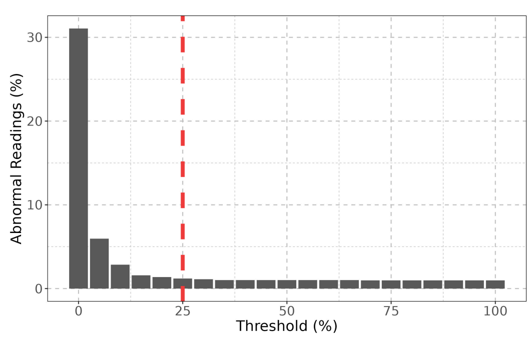

(a) Sa43001.

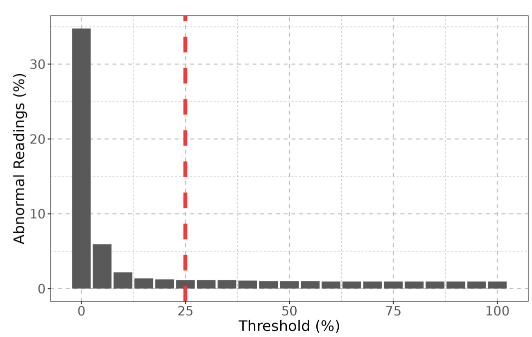

(b) Sa43057.

Figure 5.2. Percentage of abnormal module temperature readings for two outdoor modules: sa43001 and sa43057.

and the lowest testing MAE with a median value of 0.669 °C. Therefore, it was chosen to predict the module temperature for replacing the abnormal readings. 98.3% of the abnormal readings were successfully replaced, and the remaining abnormal readings were removed.

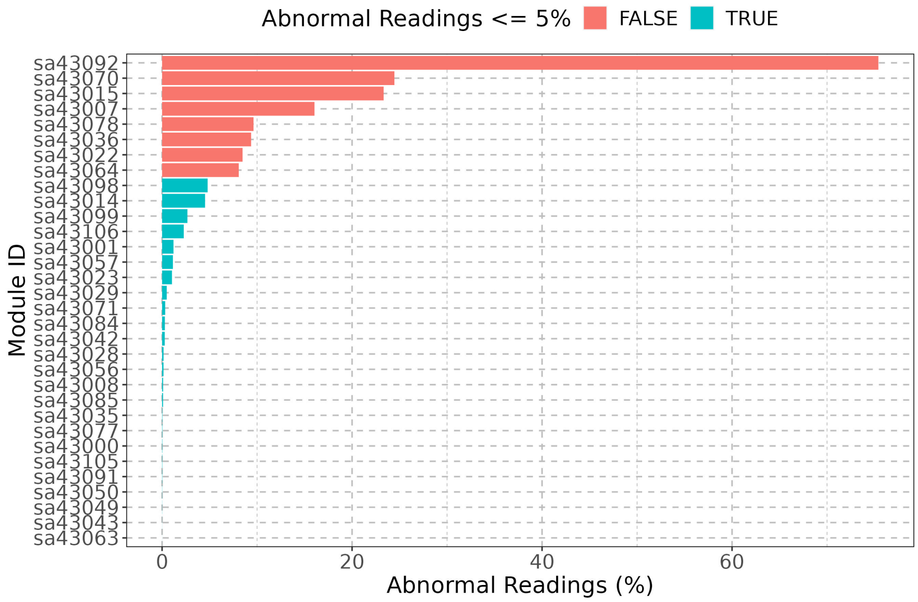

Figure 5.3. Percentage of abnormal module temperature readings for each outdoor minimodule.

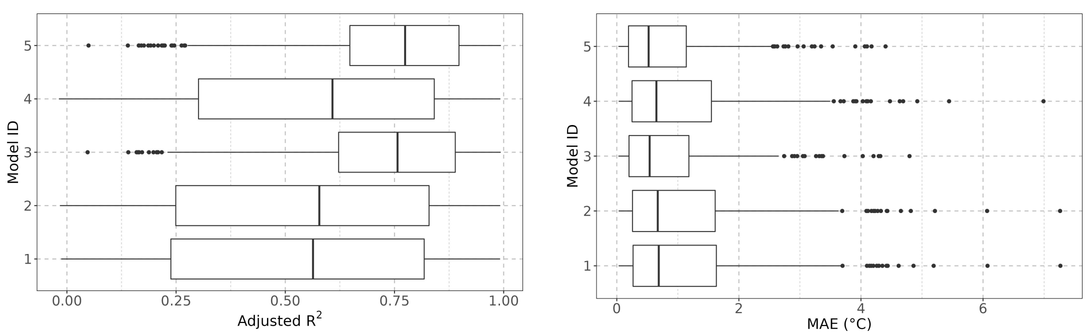

(a) adj R^2. (b) MAE.

Figure 5.4. Boxplots of the adj R^2 and the testing MAE evaluated from the normal readings for the five models predicting the module temperature.

5.3.2 Outdoor *Isc*-*Voc* Results of One Outdoor PV Module

Outdoor minimodule sa43099 is chosen as an example to show the results of predicted electrical features and power loss factors obtained from the $SunsVoc$ package[54]. Fig. 5.5 shows the four normalized electrical features, including ${}^{n}P_{mp,IV}$, ${}^{n}I_{sc,IV}$, ${}^{n}R_{s,IV}$, and

$^{n}V_{mp,PIV}$ for outdoor minimodule sa43099. These electrical features can also be obtained in the lab through current-voltage (I-V) and $Suns$-V_{oc} characterizations. Therefore, they can be common variables to compare module degradation behaviors under indoor accelerated and outdoor exposures. The electrical features were normalized by the average value of the corresponding feature for the first three months of the same minimodule for Fig. 5.5. The curve in Fig. 5.5 is fitted by the local estimated scatterplot smoothing (LOESS) method[101] to indicate the trend of how the feature changes over time. Fig. 5.6 shows the four power loss factors with LOESS curves, in which a negative $\Delta Power$ value represents a power loss.

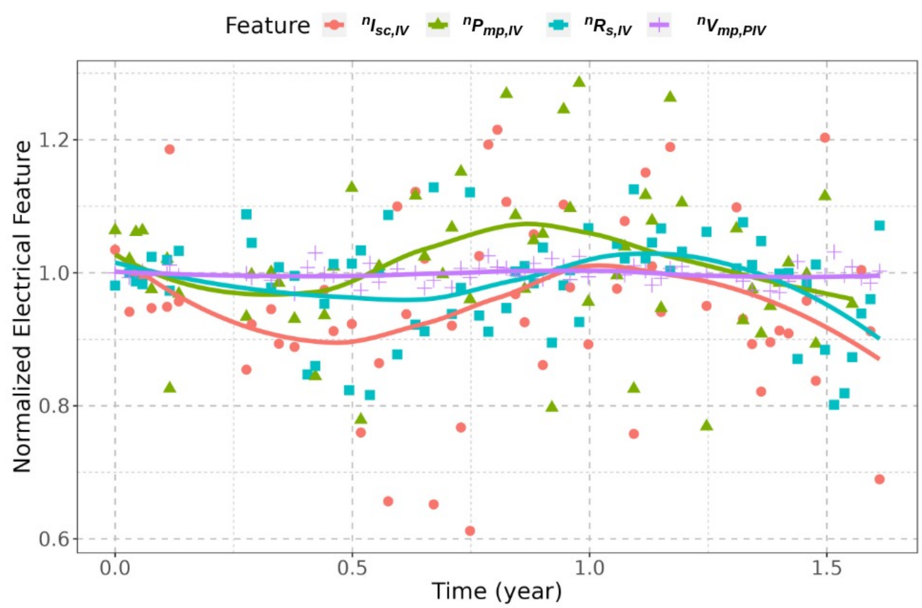

Figure 5.5. The normalized electrical features obtained from the $SunsVoc$ package for outdoor module sa43099, including $^{n}P_{mp,IV}$, $^{n}I_{sc,IV}$, $^{n}R_{s,IV}$, and $^{n}V_{mp,PIV}$.

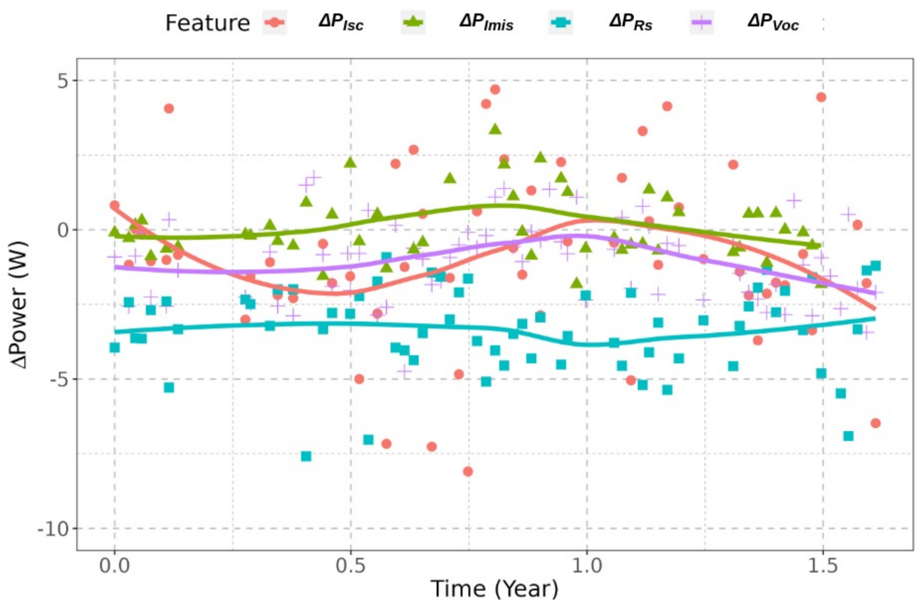

Figure 5.6. The four power loss factors obtained from the *SunsVoc* package for outdoor module sa43099, including ΔP_{Isc}, ΔP_{Voc}, ΔP_{Rs}, and ΔP_{Imis}.

5.3.3 Normalized Electrical Features

Fig. 5.7 shows the average values and confidence intervals (CIs) of the normalized electrical features, including ${}^{n}P_{mp,IV}$, ${}^{n}I_{sc,IV}$, ${}^{n}R_{s,IV}$, and ${}^{n}V_{mp,PIV}$, in the final three months for each module variant. In the first two months of the outdoor exposure, there were frequent troubleshooting issues and necessary repairs to be made. The data from the third month were missing due to a problem with the hardware. Therefore, we used the data from the fourth and fifth months for normalization. The red open circles in Fig. 5.7 mark the average values, and the two blue dashed lines mark the values of 1 ± 0.005. The black bars represent the 83.4% CIs. If two of such bars have no overlap, then their corresponding averages have a statistically significant difference at the significance level of 0.05. The purple bars represent the 95% CI. When a value is not within the purple bar of a module variant, its average value is significantly different from that value at the significance level of 0.05. The average values and CIs of the ${}^{n}R_{s,IV}$ in the final three months of each module are shown in Fig. 5.8. In addition, the averages and CIs of the ${}^{n}P_{mp,IV}$ for the four packaging combinations, considering only the encapsulant materials (EVA or POE) and module architectures (GB or DG), are shown in Fig. 5.9.

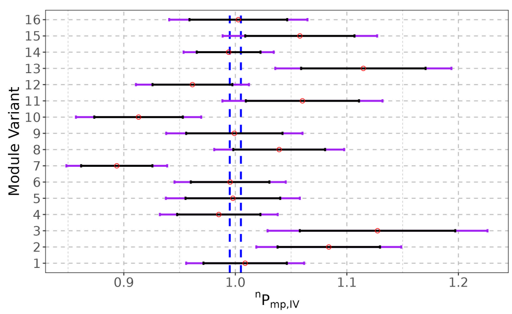

(a) ${}^{n}P_{mp,IV}$.

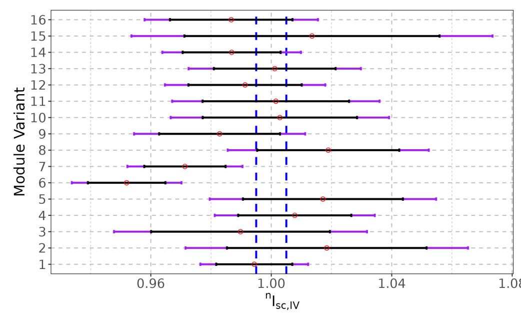

(b) ${}^{n}I_{sc,IV}$.

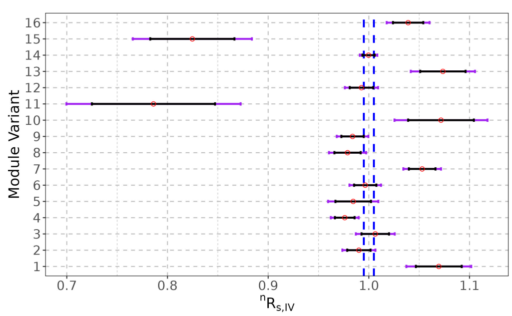

(c) ${}^{n}R_{s,IV}$.

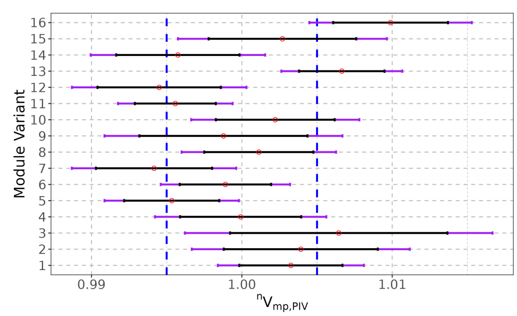

(d) ${}^{n}V_{mp,PIV}$.

Figure 5.7. The average value, 83.4% CI, and 95% CI of the four normalized electrical features, including ${}^{n}P_{mp,IV}$, ${}^{n}I_{sc,IV}$, ${}^{n}R_{s,IV}$, and ${}^{n}V_{mp,PIV}$, from the final three months for each module variant.

5.3.4 Degradation Mechanisms: Power Loss Factors

Fig. 5.10 shows the average values and CIs of the normalized uniform current power loss (${}^{n}\Delta P_{Isc}$) from the final three months of exposure for each module variant and each outdoor minimodule. The red open circles in Fig. 5.10 represent the average values, and

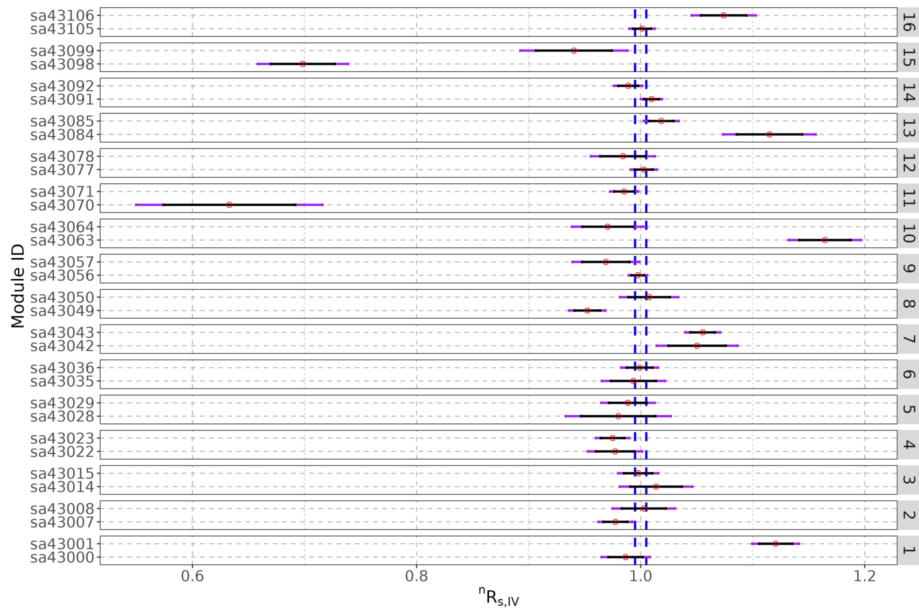

Figure 5.8. The average value, 83.4% CI, and 95% CI of $^nR_{s,IV}$ from the final three months for each module.

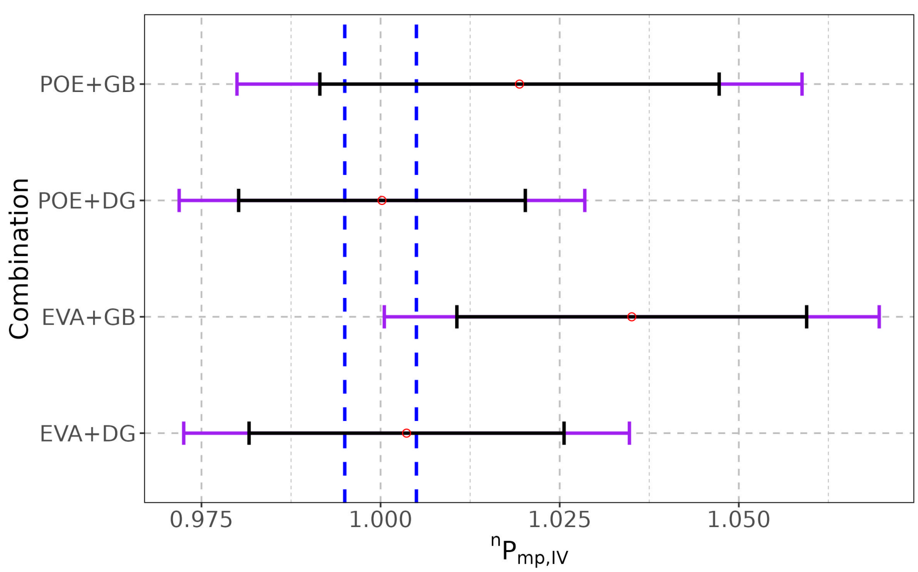

Figure 5.9. The average value, 83.4% CI, and 95% CI of $^nP_{mp,IV}$ of the four packaging combinations considering only the encapsulant materials and module architectures using data from the final three months.

the black and purple bars represent the 83.4% CI and 95% CI, respectively. If two black bars have no overlap, then their corresponding averages have a statistically significant difference at the significance level of 0.05. Comparing these black bars provides a way to visualize the null hypothesis two-sample t-test results of comparing the average values of two groups[96–98]. The two blue dashed lines mark the values of ± 0.5%. The average value in the fourth and fifth months was first subtracted from each power loss factor. Then the data were normalized by the average $P_{mp,IV}$ for these two months. Similar results for the normalized recombination power loss (${}^{n}\Delta P_{Voc}$), the normalized R_s power loss (${}^{n}\Delta P_{Rs}$), and the normalized current mismatch power loss (${}^{n}\Delta P_{Imis}$) are shown in Fig. 5.11, Fig. 5.12, and Fig. 5.13, respectively. Moreover, Fig. 5.14 shows the average values and CIs of the four normalized power loss factors in the final three months of exposure for the four packaging combinations, namely EVA+GB, EVA+DG, POE+GB, and POE+DG.

5.4 Discussion

5.4.1 Solution for Failure in Module Temperature Thermocouples

Fig. 5.1 shows the percentage of outliers each day for the module temperature readings obtained from minimodule sa43070 through a comparison of the module temperature readings from all 32 modules every five minutes. The percentage of outliers is unusually high for most days between the 200th to the 382nd day. Based on our maintenance records, the thermocouple for recording the module temperature of minimodule sa43070 got repaired on the 382nd day. Therefore, the outlier detection based on comparing the module temperature readings from all modules can accurately reflect when

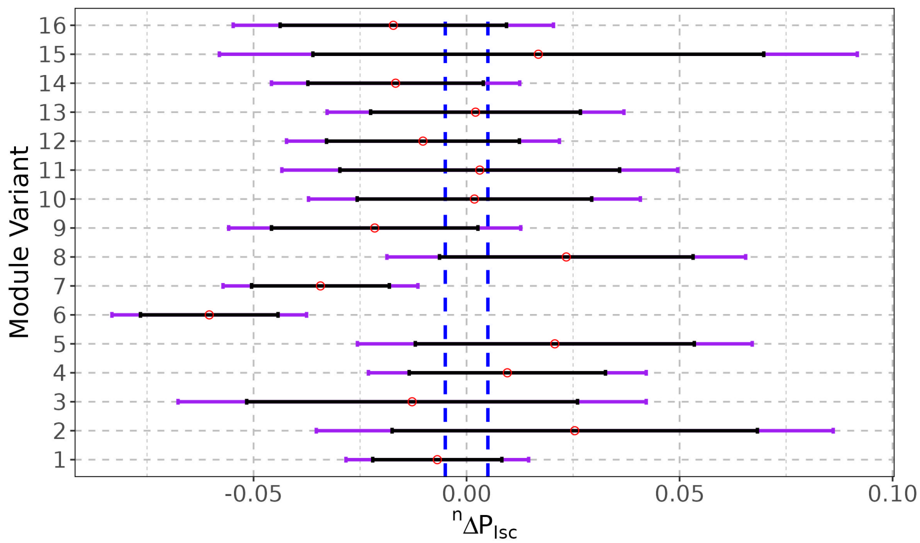

(a) Each Module Type.

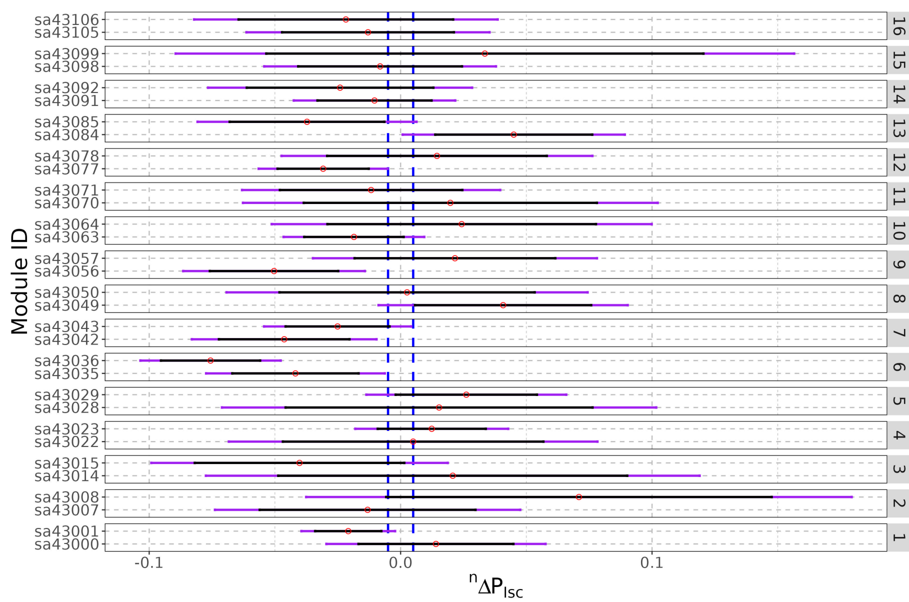

(b) Each Module.

Figure 5.10. The average value, 83.4% CI, and 95% CI of the normalized uniform current power loss ($^n\Delta P_{Isc}$) from the final three months of exposure for each module variant and each module, respectively.

the status of a thermocouple changes. A threshold for the percentage of outliers each day was set to consider the time continuity of the thermocouple behavior. When the

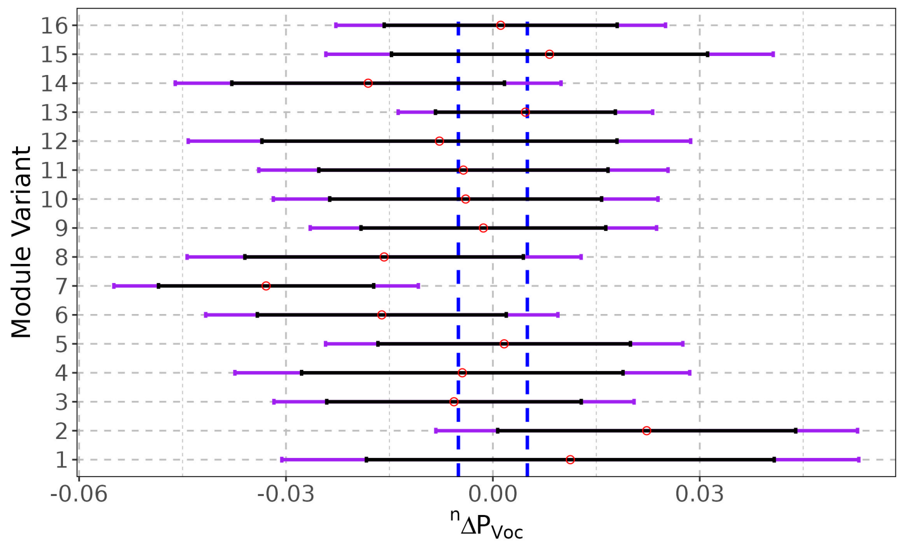

(a) Each Module Type.

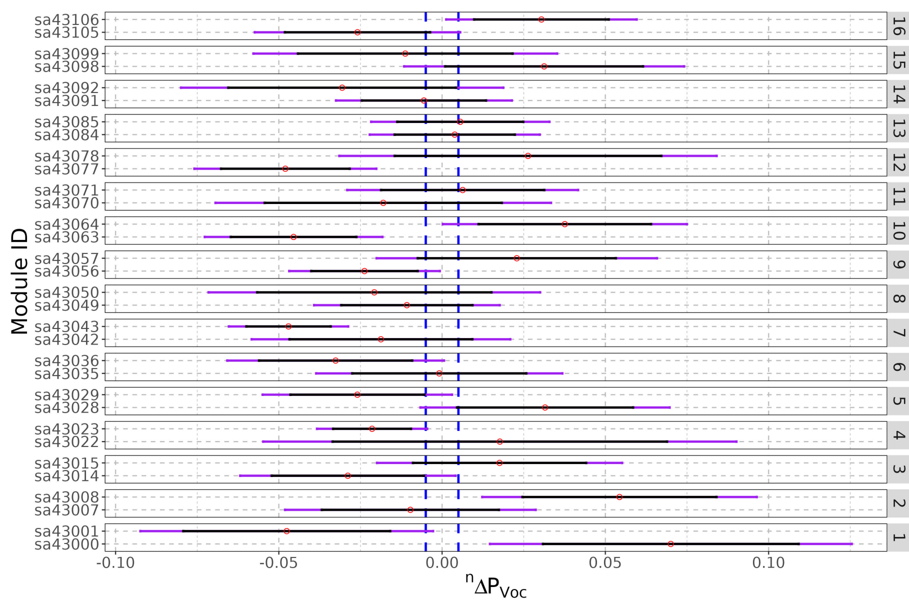

(b) Each Module.

Figure 5.11. The average value, 83.4% CI, and 95% CI of the normalized recombination power loss ($^{n}\Delta P_{Voc}$) from the final three months of exposure for each module variant and each module, respectively.

percentage of outliers for a day exceeded the threshold, then all readings for that day were labeled as abnormal. Otherwise, only the outliers were labeled as abnormal. If

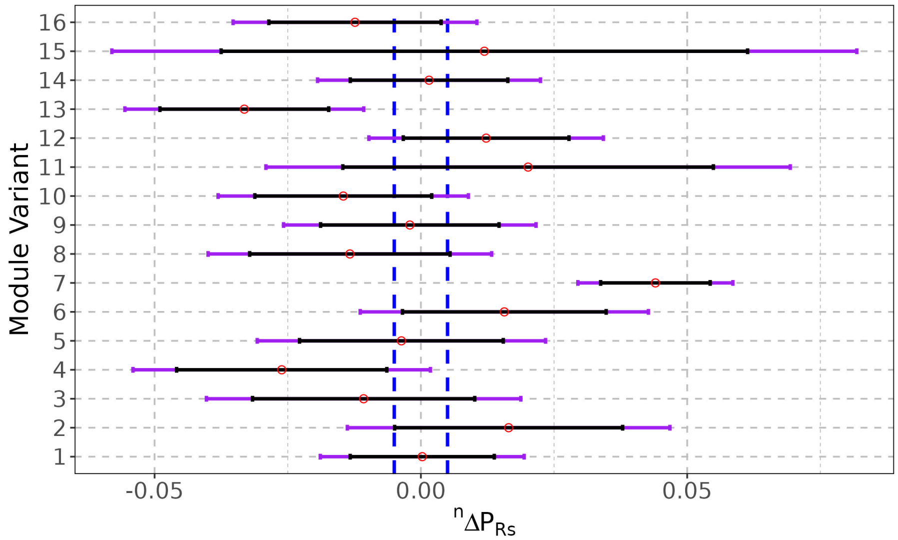

(a) Each Module Type.

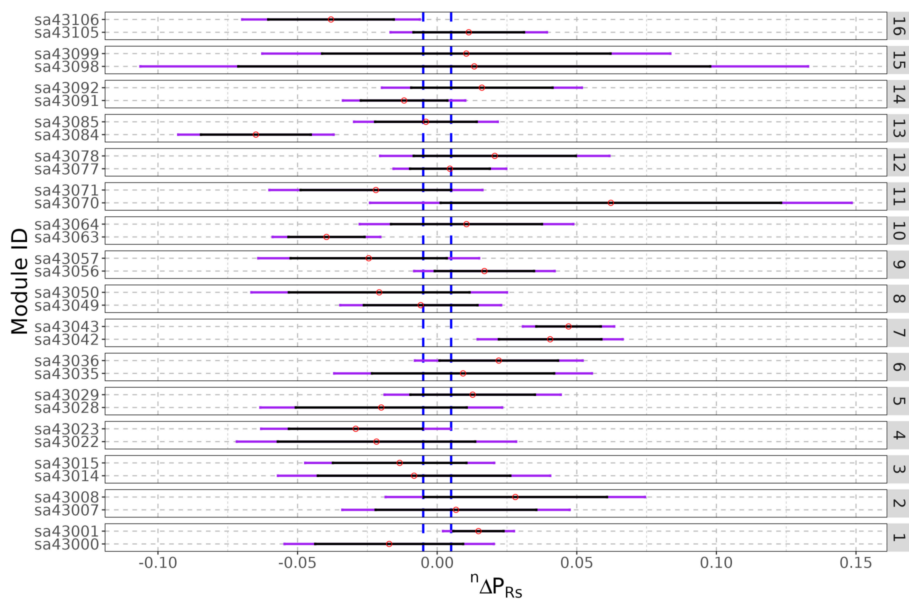

(b) Each Module.

Figure 5.12. The average value, 83.4% CI, and 95% CI of the normalized power loss due to series resistance ($^{n}\Delta P_{Rs}$) from the final three months of exposure for each module variant and each module, respectively.

the threshold is too small, like the extreme case of 0, then even one abnormal reading will lead to all readings on the same day being labeled as abnormal. However, if the

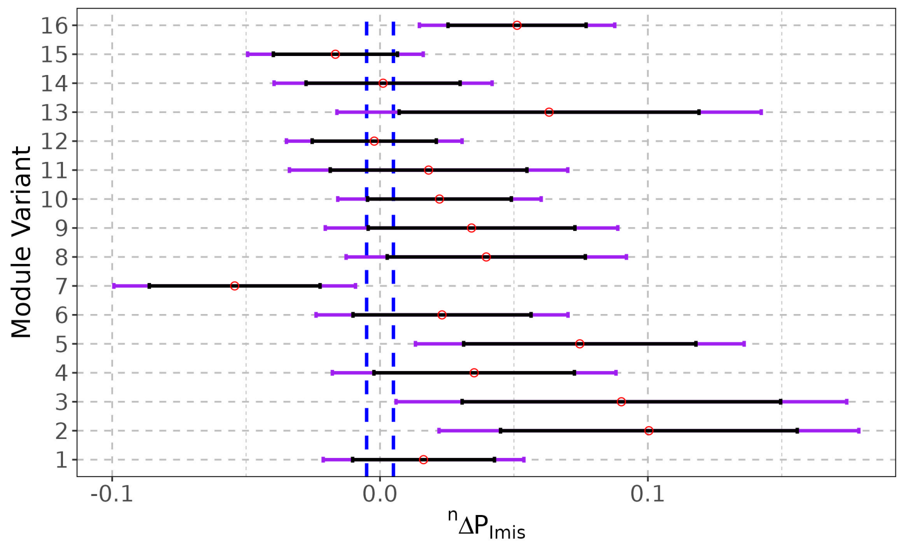

(a) Each Module Type.

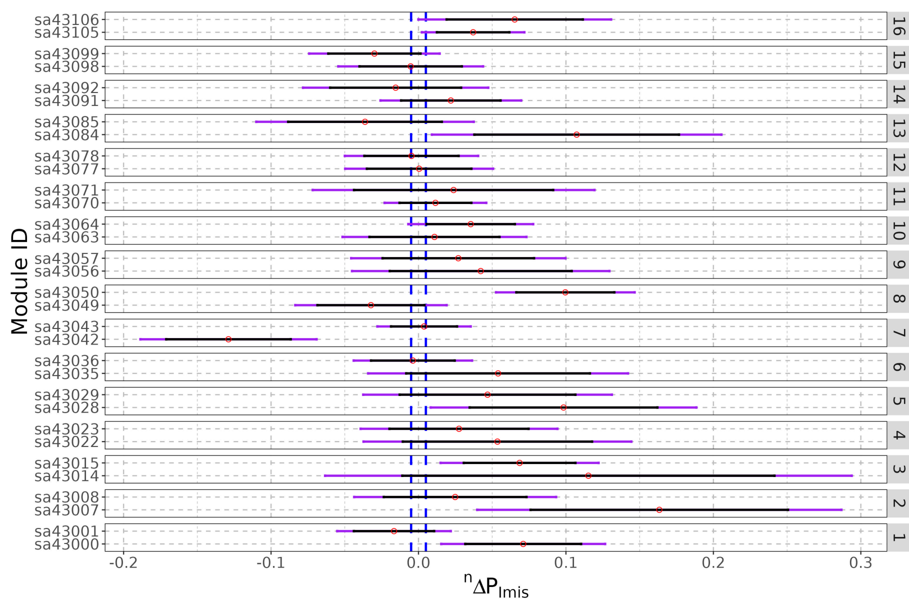

(b) Each Module.

Figure 5.13. The average value, 83.4% CI, and 95% CI of the normalized current mismatch power loss (${}^{n}\Delta P_{Imis}$) from the final three months of exposure for each module variant and each module, respectively.

threshold is too large, like the extreme case of 100%, it can not take the time continuity of the thermocouple's behavior into consideration. Fig. 5.2 shows the overall percentage

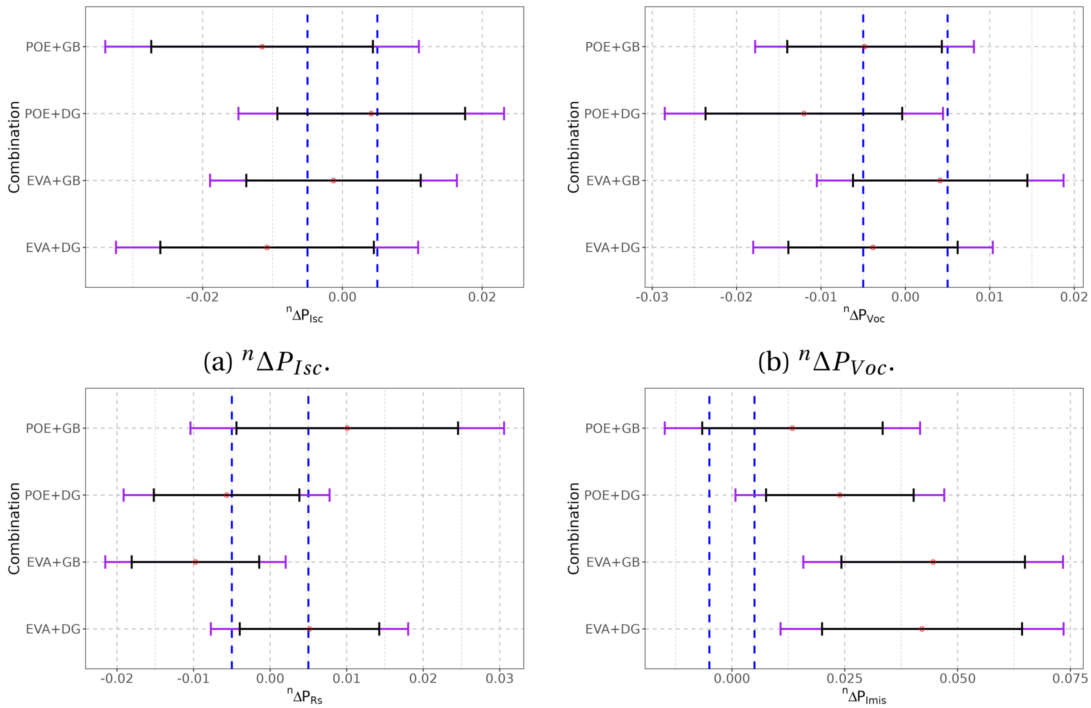

(a) $^{n}\Delta P_{Isc}$.

(b) $^{n}\Delta P_{Voc}$.

(c) $^{n}\Delta P_{Rs}$.

(d) $^{n}\Delta P_{Imis}$.

Figure 5.14. The average value, 83.4% CI, and 95% CI of the four normalized power loss factors for the four packaging combinations from the final three months of exposure.

of abnormal readings using different threshold values varying from 0% to 100% for two outdoor minimodules, which have no record of thermocouple maintenance. It is found that when the threshold value is less than 25%, there is an apparent increasing trend in the percentage of abnormal readings with a decrease of threshold values. However, the percentage of abnormal readings is very stable when the threshold value is no less than 25%. Therefore, the threshold value was set to 25% to balance the continuity of thermocouple behavior and the chances of mislabeling many normal readings.

Only 6.08% of all module temperature readings were detected as abnormal. They did not appear evenly across all modules but were concentrated around a few modules. As shown in Fig. 5.3, there are eight modules with more than 5% abnormal readings.

Sa43092 has the highest percentage of abnormal readings at 75.4%. Five models described in Table 5.1 were evaluated to predict the module temperature for replacing the abnormal readings. The model was fit and evaluated using the normal readings in each hour, with 80% of the data used for training the model and 20% for testing the model performance. Fig. 5.4 shows the boxplot of the adjusted R-squared (adj R^2) and the testing mean absolute error (MAE) of each model. Model 5 has the highest median adj R^2 and the lowest median testing MAE, so it was selected as the imputation model to replace abnormal module temperature readings. The performance of model 3 is very similar to that of model 5. Their median adj R^2, testing MAE, and testing root-mean-squared error (RMSE) are 0.757 and 0.774, 0.538 °C and 0.522 °C, and 0.696 °C and 0.673 °C, respectively.

Since the performance of model 3 is similar to that of model 5 and is much better than that of model 4, the installed position (rows and columns) must be a more critical independent variable than cell type or module architecture for predicting the module temperature. When replacing abnormal readings, normal readings within half an hour before and after the abnormal reading were selected first. Then 80% of the normal readings were used to train the model, and the rest were used to calculate the testing MAE. When the testing MAE was no more than 2 °C, the predicted module temperature was used to replace the abnormal reading. 98.3% of abnormal readings were successfully replaced, and the remaining 1.7% were removed. As can be seen in Fig. 5.4, there are occasional cases with the model performing relatively worse, indicated by a lower adj R^2 and a significantly higher testing MAE.

5.4.2 Comparison of Power Output for the Sixteen Module Types

Fig. 5.5 shows how the normalized predicted electrical features under reference conditions change over time for minimodule sa43099. The reference conditions are 1000 W/m^2 POA and the median annual module temperature when POA is in the range of 1000 ± 10 W/m^2. The reference module temperature was estimated to be 45 °C using the data from the first year of exposure. ${}^{n}V_{mp,PIV}$ is found to fluctuate around 1 with a much smaller magnitude than that of the other three I-V features, including ${}^{n}P_{mp,IV}$, ${}^{n}I_{sc,IV}$, and ${}^{n}R_{s,IV}$, which also show more apparent seasonal changes. In PLR calculations with timeseries P_{mp} data, models such as classical seasonal decompose (CSD) and autoregressive integrated moving average (ARIMA) are usually applied to obtain a trend without seasonality and noise[32]. However, these models need data taken over the course of more than two years, so they could not be implemented to process the outdoor data that were currently available in this study. Therefore, we compare the normalized features among different module variants, where the normalization is implemented by the average performance of the same module at the beginning of the exposure. The four normalized electrical features in Fig. 5.5 are obtained by being divided by the average value of each feature from the first three months. However, due to frequent maintenance work and missing records during the first three months, we use the average reading from the fourth and fifth months for the normalization process when comparing different module variants.

The average values and confidence intervals (CIs) of ${}^{n}P_{mp,IV}$ for each module variant in the final three months are shown in Fig. 5.7a. It is worth noting that a value of more than one does not necessarily mean a power increase due to the retained seasonal effect. Therefore, our analysis focuses on the differences between module variants rather than on the amount of change that occurs in an individual module variant. Module variants 7, 10, and 12 are found to have lower average ${}^{n}P_{mp,IV}$ values, which are significantly lower than that of module variants 2, 3, 8, 11, 13, and 15. We also notice that several module variants, including 1, 7, 10, 11, 13, 15, and 16, have average ${}^{n}R_{s,IV}$ values that are significantly different from that of most module variants, accompanied by a large confidence interval as shown in Fig. 5.7c. From Fig. 5.8, it can be found that six of these module variants, except module variant 7, have one minimodule with an average ${}^{n}R_{s,IV}$ value that is significantly different not only from the majority of the other minimodules but also the other minimodule of the same variant. Such a difference in ${}^{n}R_{s,IV}$ between two modules of the same type is likely to be caused by electrical connection failures and repairs when strange electrical output was noticed. Without considering these six module variants, module variants 7 and 12 are found to have lower average ${}^{n}P_{mp,IV}$ values, which are significantly lower than that of module variants 2, 3, and 8.

5.4.3 Comparison of Degradation Modes for the Sixteen Module Types

The amount of differences between module variants varies among ${}^{n}I_{sc,IV}$, ${}^{n}R_{s,IV}$, and ${}^{n}V_{mp,PIV}$, which corresponds to different distances between the two blue dashed lines in Fig. 5.7b, Fig. 5.7c, and Fig. 5.7d. The largest difference in the average values between module variants is 6.69% for ${}^{n}I_{sc,IV}$, 7.69% for ${}^{n}R_{s,IV}$, and 1.57% for ${}^{n}V_{mp,PIV}$, respectively. The evaluation of the largest difference in ${}^{n}R_{s,IV}$ does not include the six module variants suspected to be influenced by electrical connection failures and repairs. The largest difference in the average ${}^{n}V_{mp,PIV}$ is only about one-fifth of that of ${}^{n}I_{sc,IV}$ and ${}^{n}R_{s,IV}$. The changes in these I-V features reflect specific degradation modes and mechanisms. The decrease in I_{sc} indicates the uniform current loss, which is often associated with the discoloration of the encapsulant. The increased R_s leads to more power loss as dissipated heat caused by metal connection corrosion or joint fatigue. The decrease in $V_{mp,PIV}$ results from easier recombination due to solar cell defects. The differences in these normalized electrical features reflect some quantitative differences in the degradation behaviors of various module variants.

Module variants 6 and 7 are found to have lower average ${}^{n}I_{sc,IV}$ values which are significantly lower than that of module variants 2, 4, 5, and 8, as shown in Fig. 5.7b. After excluding the module variants suspected to be influenced by electrical connection failures and repairs, module variant 7 is found to have the highest average ${}^{n}R_{s,IV}$, which is significantly higher than that of all the other module variants, as shown in Fig. 5.7c. Module variant 4 has the lowest average ${}^{n}R_{s,IV}$, which is significantly lower than that of module variants 3 and 14. While module variants 5, 7, 11, 12, and 14 have average ${}^{n}V_{mp,PIV}$ values that are significantly lower than those of module variants 13 and 16, the amount of difference is generally small across module variants. Comparing results of ${}^{n}I_{sc,IV}$, ${}^{n}R_{s,IV}$, and ${}^{n}V_{mp,PIV}$ provides some clues on significant power loss differences of ${}^{n}P_{mp,IV}$ among module variants. Module variants 7 and 12, which have greater power loss, both experience a greater $V_{mp,PIV}$ decrease. Module variant 7 also experiences more change in I_{sc} and R_s. Module variants 2 and 8, which display less power loss, are found to have the highest ${}^{n}I_{sc,IV}$, indicating a minimal decrease in I_{sc}. However, the percentage of change in these electrical parameters is not linearly proportional to their contributed power loss due to their physical relationships to the P_{mp}. The four power loss factors obtained from the $SunsVoc$ package[54], which quantify the power loss due to different degradation modes, can be compared directly to rank their contributions to the total power loss.

Fig. 5.10, Fig. 5.11, Fig. 5.12, and Fig. 5.13 show the average values and CIs of the four normalized power loss factors, including ${}^{n}\Delta P_{Isc}$, ${}^{n}\Delta P_{Voc}$, ${}^{n}\Delta P_{Rs}$, and ${}^{n}\Delta P_{Imis}$, for each module variant and each module from the final three months of exposure. The normalized power loss factor is the ratio of the change in a specific power loss factor to the initial P_{mp}. The largest difference between module variants is 8.58% for ${}^{n}\Delta P_{Isc}$, 5.52% for ${}^{n}\Delta P_{Voc}$, 7.72% for ${}^{n}\Delta P_{Voc}$, and 15.60% for ${}^{n}\Delta P_{Imis}$. The largest difference between module variants is minimal for ${}^{n}\Delta P_{Voc}$, which agrees with the findings in comparing ${}^{n}V_{mp,PIV}$ to other I-V features, indicating minor differences in the change of recombination behavior among module variants.

As shown in Fig. 5.10, module variants 6 and 7 have lower average ${}^{n}\Delta P_{Isc}$ values, which are significantly lower than that of module variants 2, 4, 5, and 8. These identified module variants are in complete agreement with the comparison of ${}^{n}I_{sc,IV}$ shown in Fig. 5.7b. Comparing the 83.4% CIs of ${}^{n}\Delta P_{Isc}$ between the two modules in each module variant among these six module variants mentioned above, no significant differences are found. Therefore, the module variant comparison result is affected less by the inconsistency of sample performance and better represents the universal performance of the module variant. Module variants 6, 7, 8, and 14 have lower average ${}^{n}\Delta P_{Voc}$ values than the others, as shown in Fig. 5.11. No module variants are found to have a significantly higher average ${}^{n}\Delta P_{Voc}$ than these module variants, indicating comparable changes in recombination behavior. As shown in Fig. 5.12, module variants 4 and 13 are found to have lower average ${}^{n}\Delta P_{Rs}$ values than those of the other module variants, which are also significantly lower than those of module variants 2, 6, 7, and 12. The results of module variant 13 are strongly influenced by the sample disparity, indicated by the significant differences in the average ${}^{n}R_{s,IV}$ and ${}^{n}\Delta P_{Rs}$ of its two constituent modules. The results for ${}^{n}\Delta P_{Imis}$ are shown in Fig. 5.13, in which module variants 7 and 15 are found to have an average ${}^{n}\Delta P_{Imis}$ that is significantly lower than that of module variants 2, 3, 5, 13, and 16. Significant differences in the average ${}^{n}\Delta P_{Imis}$ are found between the two modules of the same variant in module variants 2, 7, and 13, so the ${}^{n}\Delta P_{Imis}$ results of these three module variants are more affected by the inconsistency of modules.

From the comparison of the four power loss factors among different module variants, the three modules variants with a higher average ${}^{n}P_{mp,IV}$ are found to have a better performance in ${}^{n}\Delta P_{Isc}$ and ${}^{n}\Delta P_{Rs}$ for module variant 2, ${}^{n}\Delta P_{Imis}$ and ${}^{n}\Delta P_{Isc}$ for module variant 3 and module variant 8, respectively. Module variant 7, which has a lower average ${}^{n}P_{mp,IV}$, is found to have significantly lower average values in ${}^{n}\Delta P_{Isc}$ and ${}^{n}\Delta P_{Voc}$. While module variant 12 has a relatively low average ${}^{n}P_{mp,IV}$, which is 6.79% higher than that of module variant 7, it had no significantly lower average values in any power loss factors. The power loss factor with the lowest average value is defined as the dominant power loss factor for each module variant. The dominant power loss factors for the two module variants with significantly lower ${}^{n}P_{mp,IV}$ values are ΔP_{Imis} and ΔP_{Isc} for module variants 7 and 12, respectively. In addition, ΔP_{Isc} is the dominant power loss factor for most module variants, followed by ΔP_{Rs}.

5.4.4 Degradation Dependency on Module Specification

The sixteen module variants can be classified into four packaging combinations if considering only the encapsulant materials and module architectures, namely EVA+GB, EVA+DG, POE+GB, and POE+DG. The average values and CIs of ${}^{n}P_{mp,IV}$ for each packaging combination from the final three months are shown in Fig. 5.9, in which no significant differences are identified. The average ${}^{n}P_{mp,IV}$ is higher for GB modules than that of their counterpart using the same encapsulant material. The power loss factors of these four packaging combinations are compared in Fig. 5.14, in which no significant differences are found among packaging combinations in any power loss factors. DG modules are found to have a lower average ${}^{n}\Delta P_{Voc}$ than GB modules, and POE modules are found to have a lower average ${}^{n}\Delta P_{Imis}$ than EVA modules. A longer exposure time is needed to amplify the degradation performance differences among module variants or packaging combinations and enable robust seasonal decomposition. As shown in Fig. 5.5 and Fig. 5.6, most electrical features and the four power loss factors all experience noticeable seasonal changes over time. Recent studies have started paying more attention to data quality to obtain robust $PLRs$ of outdoor modules. Timeseries data of less than two years is not recommended for PLR evaluation in the latest IEA PVPS report of task 13[35].

5.5 Conclusions

In this study, 32 minimodules were fabricated with four multicystalline Si P-Type PERC cells in each, mounted on a fixed rack on an outdoor solar farm, which is in the Dfa climate zone in the Köppen-Geiger climate classification system. Outdoor timeseries current-voltage curves, module temperatures, and POA taken over the course of 1.6 years were processed using the $ddiv$ and $SunsVoc$ packages to obtain the predicted electrical features and the four power loss factors at references conditions. These power loss factors include uniform current power loss (ΔP_{Isc}), recombination power loss (ΔP_{Voc}), power loss due to R_s (ΔP_{Rs}), and current mismatch power loss (ΔP_{Imis}). A method of detecting abnormal module temperature readings and a model to impute the corresponding normal readings for replacement are proposed with a median testing MAE around 0.67 °C. After normalization, the averages and confidence intervals of these electrical features and power loss factors are reported and compared among module variants for the final three months of exposure. Two module variants are found to have a significantly lower ${}^{n}P_{mp,IV}$, and their dominant power loss factors are ΔP_{Imis} and ΔP_{Isc}, respectively. The dominant power loss factor for most module variants are ΔP_{Isc} and ΔP_{Rs}. The dependencies of ${}^{n}P_{mp,IV}$ and the four power loss factors on the four packaging combinations considering only the encapsulant materials and module architectures are investigated, and no statistically significant differences are observed. A further extension of outdoor exposure is necessary to enable robust seasonal decomposition and to amplify the degradation differences among module variants and packaging combinations.

6 Indoor/outdoor Cross-correlation for PV Degradation Studies

Title to submit: **To Compare Activated Mechanisms and Performance Loss using Cross-correlation of Stepwise Indoor and Timeseries Outdoor Degradation Studies**

Indoor accelerated exposures are generally used to study the reliability of photovoltaic (PV) modules. They reproduce the degradation and failure mechanisms experienced during real-world exposure in a shorter timeframe. The environmental conditions for outdoor exposures are complicated; they vary by time and installed location leading to differences in the degradation behaviors of PV modules, which are hard to duplicate by accelerated exposures entirely. In recent years, more timeseries data have become available for PV modules operating in the field with developed analytical methods to obtain similar features to those measured using lab characterizations. This provides opportunities to investigate their degradation behaviors in detail and compare performance between indoor accelerated exposures and outdoor exposures using the same features. Linking the degradation behaviors under indoor accelerated and under outdoor exposures is essential to evaluate the PV module lifetime and guide the development of accelerated exposures. This study developed a cross-correlation method comparing models that describe how the electrical features change over time to quantify the difference in rates and trends to evaluate the similarities in the degradation behaviors of PV modules under different exposures. The developed method was applied to compare sixteen module variants under the outdoor exposure and two indoor accelerated exposures, including modified damp heat (mDH) and mDH with full-spectrum light (mDH+FSL). The results show that our accelerated exposures, on average, lead to a twice faster power loss when compared to the outdoor exposure with high similarities in trends of power reduction and series resistance increase during the exposure time covered by the scaled indoor accelerated exposure.

6.1 Introduction

Most commercial PV modules operate under environmental conditions that vary with time and location. PV reliability studies use indoor accelerated exposures more often since outdoor exposures are generally more expensive due to the longer exposure time needed. However, recently more timeseries data have become available for PV modules installed in the field; this provides further opportunities to study their degradation under daily operation. Some methods have been developed to process timeseries data in order to obtain features that are usually characterized in a lab under strictly controlled conditions. These methods make it possible to compare module performance under indoor accelerated and outdoor exposures using the same features[51]. It is essential to link the degradation behaviors between indoor accelerated and outdoor exposures to guide lifetime estimation and improve the design of accelerated exposures. There are two typical ways to build such a link: one is to match the environmental conditions, and the second is to match the characterized performance. For matching environmental conditions, Miller et al. used an accumulated dose of light when comparing the maximum shear stress of samples under different exposures[13]. Bheemreddy et al. input the temperature and relative humidity to the time-dependent Hallberg-Peck Model (a corrosion rate analytical model) to compare PV module performance under different exposing conditions[79]. Matching the environmental condition for this comparison brings many challenges, including integrating a variety of environmental variables together, accounting for their dynamic behaviors, and choosing a proper model. For matching characterized performance, Kersten et al. compared the power loss of PV modules installed in Cyprus and module under current injection around maximum power at 75 °C in the lab. A one-year exposure in Cyprus was found to cause power loss equal to 290 hours in the specified indoor accelerated exposure[82]. A similar approach was used to investigate accelerated factors between the outdoor exposure and multiple accelerated exposures with different temperature settings to study the potential induced degradation[83]. However, matching performance usually assumes identical degradation mechanisms, and the result is influenced by time point selection when the power loss rate is not constant.

This study first modeled the degradation behaviors of modules under accelerated and outdoor exposures through power and other electrical features related to different degradation mechanisms. Then a method named indoor/outdoor cross-correlation was developed to compare these models and quantitatively evaluate differences in power loss rates and similarity in trends of features changing over time by scaling the time of indoor models. This method was then applied to compare the sixteen module variants under outdoor exposure in Cleveland and two indoor accelerated exposures: mDH and mDH+FSL. The results showed that the indoor accelerated exposures led to a power drop roughly two times faster with highly similar trends for power and series resistance within the exposure time covered by the scaled indoor exposure.

6.2 Methods

6.2.1 Research Minimodules

In this study, minimodules containing four solar cells connected in series with five junction boxes were fabricated by a solar company using its commercial manufacturing pipeline. There are sixteen module variants with differences in encapsulant materials, rear encapsulant types, module architectures, and cell types, as shown in Fig. 3.2. The encapsulant material is either ethylene-vinyl acetate (EVA) or polyolefin elastomer (POE). While the front encapsulant is always the transparent type, the rear encapsulant types can be transparent, UV-Cutoff, and opaque (also described as white encapsulant) for different module variants. The module architecture is either glass-backsheet (GB) or double glass (DG). The glass for DG modules is heat-strengthened and 2.5 mm thick. For GB modules, the front glass is tempered and 3.2 mm thick. Monofacial GB modules have a KPf backsheet with a fluorine-coated inner layer, polyethylene terephthalate (PET) core layer, and polyvinylidene fluoride (PVDF) outer layer. Bifacial GB modules have a transparent polyvinyl fluoride (PVF) backsheet with a transparent fluoroethylene vinyl ether (FEVE) inner layer, PET core layer, and PVF outer layer. The solar cell is either monofacial or bifacial multicystalline silicon P-type PERC with five busbars for different module variants. The detailed specifications for each module variant are listed in Table 3.1.

6.2.2 Stepwise Characterizations and Accelerated Exposures

This study had two kinds of accelerated exposures including mDH and a sequential exposure named mDH+FSL. For mDH, the temperature was set to 80 °C, and the relative humidity (RH) was set to 85%. When the modules were exposed under full-spectrum light (FSL), the average light intensity was 420.4 W/m^2 and 85.1 W/m^2 for the front and rear sides of the exposed module, respectively. In addition, a 0.5 Ω resistor was connected to each module in order to make it operate around maximum power (P_{mp}), and the module temperature was below 70°C. The total exposure time was 2,520 hours for each accelerated exposure. This was divided into five steps with 504 hours (21 days) per step. Under mDH+FSL, a sequential exposure was conducted with mDH taking 2/3 of the time (14 days) and FSL taking the remaining 1/3 of the time (7 days) at each exposure step. For every solar cell at each step, including the baseline, current-voltage (I-V) curves and a $Suns$-V_{oc} curve were measured to obtain measurements from eight cells in two laminated modules for each module variant under each accelerated exposure.

Every I-V measurement provided three I-V curves at three different irradiance levels: 1000 W/m^2, 500 W/m^2, and 250 W/m^2 at room temperature. After temperature corrections, the maximum power (P_{mp}) and the short-circuit current (I_{sc}) were extracted from the 1000 W/m^2 I-V curve using the $ddiv$ package[49]. The series resistance (R_s) was extracted using all three I-V curves based on IEC 60891. The $Suns$-V_{oc} curve can be converted into the Pseudo I-V curve (PIV) with an I_{sc} input, to provide an I-V curve without the effects of R_s[86]. This study used the nameplate I_{sc} at 9.465 A for the curve conversion to avoid being influenced by the change and measurement error of I_{sc} obtained from the I-V measurement. Then the voltage at maximum power was extracted from the PIV curve, denoted as $V_{mp,PIV}$. These extracted features from I-V and PIV were normalized by the feature value measured from the same solar cell at baseline.

6.2.3 Outdoor Data Collection and Processing Pipeline

Two minimodules for each module variant were installed on a tilted fixed rack at an outdoor testing site. The testing site was in the Dfa climate zone according to the Köppen-Geiger climate classification system[99], where "D" stands for continental, "f" stands for no dry season, and "a" stands for hot summer. The timeseries I-V curves, module temperature, and plane of array irradiance (POA) data have been recorded since May 2020 and up through December 2021. All of these data have been analyzed and encompass a total exposure time of 1.6 years. Timeseries I-V features were first extracted from the timeseries I-V curves using the $ddiv$ package[49]. Next, they were combined with the module temperature and POA data to obtain the predicted electrical features at reference conditions for each analyzed period (one week) using the $SunsVoc$ package[54]. These predicted features included $P_{mp,IV}$, $I_{sc,IV}$, $R_{s,IV}$, and $V_{mp,PIV}$. The reference conditions specify a POA of 1000 W/m^2 and module temperature of 45 °C; this is the annual median module temperature where POA is in the range of 1000 ± 10 W/m^2. These predicted features were normalized by the average value obtained from the same module in the first three months of exposure.

6.2.4 $<\mathrm{S|R}>$ and $<\mathrm{S|M|}$ Pathways Models

In the expressions of $<\mathrm{S|R}>$ and $<\mathrm{S|M|}$ models, "S" represents the stressor variable, "R" represents the response variable, and "M" corresponds to the mechanism variable. In this study, time was chosen as the stressor variable and was measured in years. The response variable is the normalized maximum power from I-V measurement (${}^{n}P_{mp,IV}$). The mechanism variables are ${}^{n}I_{sc,IV}$, ${}^{n}R_{s,IV}$, and ${}^{n}V_{mp,PIV}$. These features were chosen due to their relative independence and association with different degradation mechanisms. The reduction of $I_{sc,IV}$ is usually caused by the transmittance loss of the encapsulant material, the rise of $R_{s,IV}$ indicates interconnection corrosion or joint fatigue, and the decrease of $V_{mp,PIV}$ is associated with recombination due to solar cell defects. These features can be obtained from either lab characterizations and outdoor timeseries I-V feature modeling. Therefore, they can be the common variables for comparing the degradation behaviors of between modules under accelerated and outdoor exposures. The purpose of $<\mathrm{S|R}>$ and $<\mathrm{S|M|}$ models in this study is to describe the approximate trend of how the response and mechanism variables change over time. Table 6.1 lists the five models considered in the study. The number of parameters in these five models varies from two to four. The best model was selected by the highest adjusted R-squared (adj R^2). Since the purpose of these models was not an accurate prediction, and the degree of freedom was high enough to eliminate the concern of overfitting due to a large number of observations, all of the data were used to fit the model without splitting a testing dataset to evaluate the root-mean-squared error (RMSE).

Table 6.1. The five models considered for the $< S|R >$ and $< S|M|$ pathway model.

Name	Abbreviation	Expression
Simple linear	SL	$y = \beta_0 + \beta_1 x$
Simple quadratic	SQuad	$y = \beta_0 + \beta_1 x^2$
Quadratic	Quad	$y = \beta_0 + \beta_1 x + \beta_2 x^2$
Exponent	Exp	$y = \beta_0 + \beta_1 exp(x)$
Change-point linear	CP	$y = \beta_0 + \beta_1 x + \beta_2 (x - \tau)_c$ $for \quad x \leq \tau : y = \beta_0 + \beta_1 x \qquad for \quad x > \tau : y = \beta_0 + \beta_1 x + \beta_2 (x - \tau)$

6.2.5 Indoor/Outdoor Cross-correlation Algorithm

This study developed a cross-correlation algorithm to evaluate the differences in the degradation rates and trends between modules under different exposures. The algorithm returns the optimal cross-correlation scale factor ($CCSF^*$) and the cross-correlation coefficients ($CCCs$) to evaluate the rate difference and trend similarity separately. The cross-correlation scale factor ($CCSF$) is defined as the ratio of exposure time for indoor accelerated exposure to the equivalent exposure time for outdoor exposure. Therefore, it is generally lower than one because the indoor accelerated exposure usually leads to a faster degradation than the outdoor exposure. The required inputs of the cross-correlation algorithm include the $< S|R >$ and $< S|M|$ models for samples under the indoor accelerated and outdoor exposures, their exposure times, and a guessing range of $CCSF$. The algorithm begins by solving the $CCSF^*$ using only the $< S|R >$ models. The y-axis intercepts of the two $< S|R >$ models are shifted to one in order to represent a change in performance starting at exactly 100%. A $CCSF$ is then taken from the guessing range to scale the indoor $< S|R >$ model. The green and blue curves shown in Fig. 6.1 are stretched indoor $< S|R >$ models with different $CCSF$ values. Next, the overlapping exposure time is obtained between the outdoor and scaled indoor models, and one hundred time points are evenly generated in this calculated overlapping time range. This time sequence is then input to the outdoor and scaled indoor models to obtain two predicted value sequences to calculate their RMSE. The above process is repeated for all $CCSF$ in the defined guessing range with a specified interval. The $CCSF^*$ corresponds to the $CCSF$ with the lowest RMSE. In summary, the indoor $< \mathrm{S|R} >$ is scaled along the x-axis to approach the outdoor model within the overlapping exposure time, and the corresponding scale factor is the $CCSF^*$. It is worth noting that the $CCSF^*$ tends to return at the guessing boundaries when the indoor model has a tendency to be stretched or compressed to extremes. This will happen when the indoor and outdoor models have opposite trends, or one model exhibits a much slower change than the other.

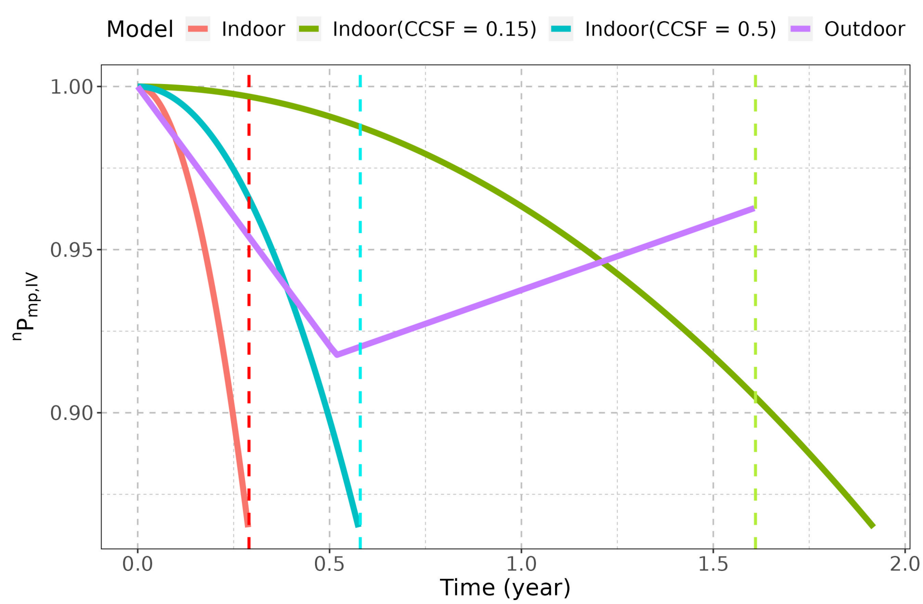

Figure 6.1. Illustration of the process for obtaining the optimal cross-correlation scale factor ($CCSF^*$) by comparing the scaled indoor model to the outdoor model in their overlapping exposure time.

Next, the $CCSF^*$ is applied to both the $< \mathrm{S|R} >$ and $< \mathrm{S|M|}$ models for the indoor accelerated exposure. After obtaining the predicted value sequences from the outdoor model and the scaled indoor model within their overlapping exposure time, the Pearson correlation coefficient is calculated instead of RMSE and renamed as the cross-correlation coefficient (CCC). Therefore, the CCC is evaluated for each pathway using a common overlapping exposure time determined by the $CCSF^*$, which is obtained by comparing the $<$ S|R $>$ models under different exposures. CCC quantifies the similarity of trends described by the models. The more similar the two models' trends are, the closer the value of CCC is to one; the more opposing the two models' trends are, the closer the value of CCC is to minus one. Additionally, $CCCs$ of the activated degradation mechanisms should be the focus when using them to evaluate the similarity of degradation behaviors for modules in different exposures. In this study, the outdoor modules exhibit changes in both $I_{sc,IV}$ and $R_{s,IV}$, while the indoor modules experience a significant change only in $R_{s,IV}$ due to the exposure conditions. Therefore, $I_{sc,IV}$ and $V_{mp,PIV}$ are not common activated mechanisms for both exposures. They are included in this study to illustrate how to select proper degradation mechanism features.

6.3 Results

6.3.1 Examples of Indoor and Outdoor $<$ S|R $>$ and $<$ S|M| Data

Fig. 6.2 shows the four normalized electrical features including ${}^nP_{mp,IV}$, ${}^nI_{sc,IV}$, ${}^nR_{s,IV}$, and ${}^nV_{mp,PIV}$ over time for module variant 8 under the mDH and the outdoor exposure conditions. There are six unique time points with measurements obtained from eight cells for each module variant in each indoor accelerated exposure. There are many more unique time data points for each module variant in the outdoor exposure, but each time point has results from only two modules. Table 6.2 lists the average percent change of the three mechanism features for the last step of the two indoor accelerated exposures and the last three months of outdoor exposure across all modules.

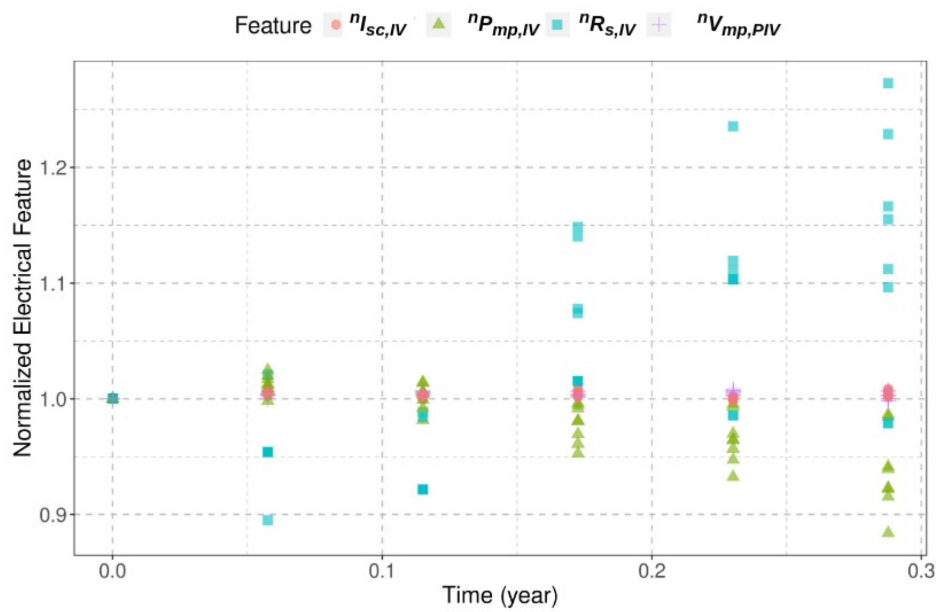

(a) mDH.

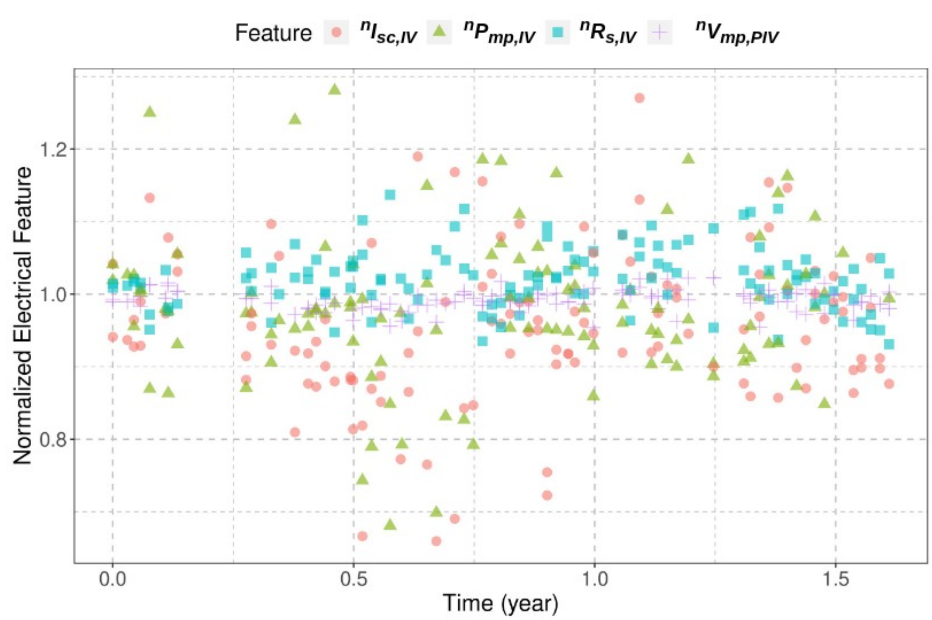

(b) Outdoor.

Figure 6.2. The normalized electrical features over time for module variant 8 under mDH and the outdoor exposure.

Table 6.2. The average percent change of the three normalized degradation mechanism features for each exposure of all of the modules.

Feature	mDH	mDH+FSL	Outdoor
${}^{n}I_{sc,IV}$	-0.14%	-0.72%	-5.15%
${}^{n}R_{s,IV}$	15.46%	14.82 %	2.58%
${}^{n}V_{mp,PIV}$	-0.09%	-0.35%	-0.75%

6.3.2 $< \mathrm{S}|\mathrm{R} >$ and $< \mathrm{S}|\mathrm{M}|$ Pathway Models

Table 6.3 shows the number of module variants for each model format that performed best under each model format and the average adj R^2 for each pathway of each accelerated exposure. Table 6.4 shows the number of module variants for each model format that performed best under each model format and the average adj R^2 for each pathway of the outdoor exposure.

Table 6.3. The number of module variants for each model format that performed best under each model format and the average adj R^2 for each pathway of each accelerated exposure.

Exposure	Pathway	Average adj R^2	Model Format				
			SL	SQuad	Quad	Exp	CP
mDH	$< Time\|{}^{n}P_{mp,IV} >$	0.444	4	4	1	2	5
	$< Time\|{}^{n}I_{sc,IV}\|$	0.427	1	1	5	1	8
	$< Time\|{}^{n}R_{s,IV}\|$	0.361	3	7	0	3	3
	$< Time\|{}^{n}V_{mp,PIV}\|$	0.141	6	3	6	0	1
mDH+FSL	$< Time\|{}^{n}P_{mp,IV} >$	0.400	3	5	2	3	3
	$< Time\|{}^{n}I_{sc,IV}\|$	0.339	3	3	5	0	5
	$< Time\|{}^{n}R_{s,IV}\|$	0.337	3	6	1	3	3
	$< Time\|{}^{n}V_{mp,PIV}\|$	0.222	2	0	4	1	9

Table 6.4. The number of module variants for each model format that performed best under each model format and the average adj R^2 for each pathway of the outdoor exposure.

Pathway	Average adj R^2	Model Format				
		SL	SQuad	Quad	Exp	CP
$< Time\|^n P_{mp,IV} >$	0.0345	0	1	2	1	12
$< Time\|^n I_{sc,IV}\|$	0.0404	1	0	0	0	15
$< Time\|^n R_{s,IV}\|$	0.127	1	0	1	1	13
$< Time\|^n V_{mp,PIV}\|$	0.0549	0	0	0	1	15

6.3.3 Cross-correlation Scale Factors and Coefficients

The guessing range of $CCSF$ was defined as 0.04 to 2, with an interval of 0.001. Therefore, the indoor model could be compressed into half of its original exposure time and stretched up to 25 times longer exposure time. The results of the $CCSF^*$ and CCC for each module variant are listed in Table 6.5 for comparing the degradation behaviors between mDH and the outdoor exposure. Table 6.6 shows results of comparing the degradation behaviors between mDH+FSL and the outdoor exposure.

6.4 Discussion

6.4.1 Power and Selected Degradation Mechanism Features

PV module performance is usually evaluated by either energy conversion efficiency or power output under certain environmental conditions. Timeseries power data are usually used to calculate the performance loss rate (PLR) to quantify the degradation rate of PV modules. Similarly, this study chose the $^nP_{mp,IV}$ to evaluate the overall performance.

Table 6.5. The results of $CCSF^*$ and CCC comparing the models for each module variant between mDH and the outdoor exposure.

Module Variant	$CCSF^*$	CCC			
		$< Time\|^n P_{mp,IV} >$	$< Time\|^n I_{sc,IV}\|$	$< Time\|^n R_{s,IV}\|$	$< Time\|^n V_{mp,PIV}\|$
1	2.000	0.804	0.999	0.968	1.000
2	2.000	0.374	0.307	0.783	0.968
3	2.000	-0.858	-0.925	0.968	1.000
4	**0.169**	0.726	0.561	0.259	0.068
5	**0.511**	0.959	0.716	0.968	-1.000
6	2.000	0.778	0.968	0.962	-0.860
7	**0.210**	1.000	-0.112	0.888	-0.515
8	**0.792**	0.935	-0.747	0.884	-0.586
9	**0.398**	0.972	0.893	0.999	0.231
10	**0.122**	0.885	-0.461	0.979	0.601
11	**0.584**	0.999	0.648	0.999	-0.649
12	2.000	-1.000	-0.775	-1.000	0.586
13	0.040	-0.696	-0.658	0.913	0.998
14	**0.210**	0.994	-0.918	1.000	-0.448
15	**1.089**	0.953	0.673	0.968	-1.000
16	**0.654**	1.000	-0.127	0.979	-0.994

Table 6.6. The results of $CCSF^*$ and CCC comparing the models for each module variant between mDH+FSL and the outdoor exposure.

Module Variant	$CCSF^*$	CCC			
		$< Time\|^n P_{mp,IV} >\|$	$< Time\|^n I_{sc,IV}\|$	$< Time\|^n R_{s,IV}\|$	$< Time\|^n V_{mp,PIV}\|$
1	2.000	0.999	0.978	0.944	0.846
2	2.000	0.378	0.414	0.783	0.868
3	2.000	-0.968	-1.000	0.999	0.645
4	**0.168**	0.862	-0.602	0.439	0.524
5	**0.599**	0.968	0.612	0.968	-0.129
6	2.000	0.800	0.968	0.937	-1.000
7	**0.207**	1.000	-0.183	0.978	-0.670
8	**0.475**	0.964	0.981	0.968	-0.948
9	**0.063**	-0.308	-0.006	-0.406	0.260
10	**0.188**	0.864	0.349	0.988	0.275
11	**0.576**	0.968	0.995	0.968	0.821
12	2.000	-0.939	-0.975	-1.000	-1.000
13	0.040	-0.560	0.678	0.918	-0.979
14	**0.357**	1.000	-0.865	1.000	0.038
15	**0.448**	0.985	0.899	0.968	-0.616
16	**1.217**	0.932	0.731	0.940	0.563

The reduction in $^nP_{mp,IV}$ can be caused by numerous reversible and irreversible physical and chemical changes happening to PV modules. These changes are reflected in different electrical signals, which can be used as indicators for different degradation mechanisms. For example, soiling and encapsulant discoloration both lead to a decrease in

I_{sc}. Multiple features extracted from different characterizations preserve some correlations due to their physical relationships like the open-circuit voltage (V_{oc}) and the voltage at the maximum power (V_{mp}) extracted from I-V curves. Features with less correlation to the others regarding their physical relationships are preferred as indicators for different degradation mechanisms. This study selected ${}^{n}I_{sc,IV}$, ${}^{n}R_{s,IV}$, and ${}^{n}V_{mp,PIV}$ for their associations to the encapsulant discoloration, interconnection corrosion, and increased recombination. In addition, when selecting degradation mechanism features, we should consider their availability. In this study, the four normalized electrical features were obtained for both the sample under indoor accelerated exposure through direct measurements and the sample exposed outdoor through modeling on timeseries I-V features like the example in Fig. 6.2.

6.4.2 Indoor/outdoor Cross-correlation

The indoor/outdoor cross-correlation algorithm first calculates the $CCSF^{*}$ through the comparison of two $<\mathrm{S|R}>$ models describing how the response variable changes over time under different exposures. The $CCSF^{*}$ is obtained by scaling the indoor model along the time axis (x-axis) to make it as close as possible to the outdoor model in the overlapping exposure time. This $CCSF^{*}$ is then applied to all indoor models, including $<\mathrm{S|R}>$ and various $<\mathrm{S|M|}$ models to calculate the CCC for different pathways in order to quantify similarity between trends in the same overlapping exposure time range. It is worth noting that the CCC of the pathway for activated degradation mechanisms is more important to evaluate the similarity of the degradation behaviors due to their higher contribution to power loss. In this study, the trends for the four normalized electrical features for module variant 8, shown in Fig. 6.2, represent a general situation of all module variants. For modules in the indoor accelerated exposure, there are more significant changes in ${}^{n}P_{mp,IV}$ and ${}^{n}R_{s,IV}$, comparing to those in ${}^{n}I_{sc,IV}$ and ${}^{n}V_{mp,PIV}$. Such differences can also be observed from the average percent change of the three mechanism features for all samples under different exposures as shown in Table 6.2. The outdoor results in Table 6.2 are estimated for the final three months and are found to have greater changes in both $I_{sc,IV}$ and ${}^{n}R_{s,IV}$ than ${}^{n}V_{mp,PIV}$. If the $CCSF^{*}$ is evaluated for each pathway rather than determined by the $< S|R >$ pathway, $CCSF^{*}$ appears at the guessing boundary as two in the majority cases for ${}^{n}I_{sc,IV}$ and ${}^{n}V_{mp,PIV}$ pathways, indicating that our indoor accelerated exposures generally lead to minor changes in ${}^{n}I_{sc,IV}$ and ${}^{n}V_{mp,PIV}$.

The changes calculated from outdoor samples in this study are not entirely due to degradation. It is challenging to extract trends while removing seasonality and noise because the short outdoor exposure time limits the repetition of seasonality. The large spread in outdoor data shown in Fig. 6.2 can be reduced by enabling seasonal decomposition. Furthermore, looking at the number of module variants that chose different model formats between Table 6.3 and Table 6.4 for different exposures, one can observe that change-point models are strongly preferred for all pathways under outdoor exposure. This is believed to be influenced by the retained seasonality. All PV modules have been stabilized through light and current injection before different exposures. As a result, they are not supposed to experience a fast power reduction in the first year due to light-induced degradation. The time length of current outdoor data was too short to investigate whether the performance loss rate changes over time. The primary purpose of this study is to illustrate the working principle of the developed cross-correlation algorithm with examples of interpreted results, since the outdoor exposure was too short to make firm conclusions on degradation performance comparison.

6.4.3 Modified Damp Heat vs. Outdoor

Table 6.5 shows the cross-correlation result comparing < S|R > and < S|M| models under mDH and outdoor exposure conditions. Ten module variants have a $CCSF^*$ that does not appear on the guessing boundaries. These $CCSF^*$ vary from 0.122 to 1.08 with an average of 0.4739, indicating that ${}^nP_{mp,IV}$ drops two times faster under mDH than outdoor exposure in the time covered by the scaled indoor model. Their $CCCs$ for the pathways of $< Time,^n P_{mp,IV} >$ and $< Time,^n R_{s,IV}|$ are very close to one with an average value of 0.9423 and 0.8924, respectively. However, the average value of $CCCs$ for $< Time,^n I_{sc,IV}|$ and $< Time,^n V_{mp,PIV}|$ are 0.1126 and -0.4292, which demonstrates dissimilar trends for how ${}^nI_{sc,IV}$ and ${}^nV_{mp,PIV}$ change over time. In addition, the three cases with a negative CCC for $< Time,^n P_{mp,IV} >$ are found to have $CCSF^*$ shown at the guessing boundaries. Another reason that will lead to a $CCSF^*$ appearing at the guessing boundaries is a large difference in the changing rates of ${}^nP_{mp,IV}$. Most cases with a $CCSF^*$ appearing at the boundaries have a $CCSF^*$ of two. For these cases, the change in ${}^nP_{mp,IV}$ is even slower under mDH than the outdoor exposure, which is believed to be partially due to their stable performance under mDH and the retained seasonality in outdoor data.

6.4.4 Modified Damp Heat + Full-spectrum Light vs. Outdoor

Table 6.6 shows the cross-correlation result for comparing models under mDH+FSL and the outdoor exposure. These are the same ten module variants with a $CCSF^*$ that does not appear at the guessing boundaries as the ones identified by comparing models under mDH and the outdoor exposure, indicating similarities in the degradation behavior under mDH+FSL and mDH. The $CCSF^*$ of these module variants varies from 0.063 to 1.217 with an average of 0.4298, indicating that ${}^{n}P_{mp,IV}$ drops about twice as fast under mDH+FSL than under the outdoor exposure, similar to mDH. The average $CCCs$ for $< Time|^{n}P_{mp,IV} >$ and $< Time|^{n}R_{s,IV}|$ are 0.8234 and 0.7809, which are slightly lower than those obtained from comparing mDH and the outdoor exposure. This difference is mainly due to the resulting difference in module variant 9. If module variant 9 is excluded, the average $CCCs$ for $< Time|^{n}P_{mp,IV} >$ and $< Time|^{n}R_{s,IV}|$ for both indoor accelerated exposures are in the range from 0.8805 to 0.9491. In addition, the average CCC for $< Time|^{n}I_{sc,IV}|$ is 0.2911, which is higher than that obtained from comparing mDH and the outdoor exposure. The decrease in ${}^{n}I_{sc,IV}$ is slightly greater under mDH+FSL than mDH as shown in Table 6.2, although it is still much smaller than the change in ${}^{n}R_{s,IV}$. The average CCC for $< Time|^{n}V_{mp,PIV}|$ is only 0.0117, indicating dissimilarity in trends of ${}^{n}V_{mp,IV}$ between mDH+FSL and the outdoor exposure. It is worth noting that even if the $CCCs$ for ${}^{n}I_{sc,IV}$ and ${}^{n}V_{mp,PIV}$ are large in this study, it only indicates similar trends for the corresponding degradation mechanisms and is not enough to conclude highly similar degradation behaviors under different exposures. This is due to the activated mechanisms not being consistent between the indoor accelerated and outdoor exposures.

6.5 Conclusions

This study proposes a cross-correlation algorithm to compare the degradation behaviors between PV modules under indoor accelerated exposures and outdoor exposures in order to evaluate similarities in degradation rates and trends through models that describe how electrical features change over time. The normalized maximum power (${}^{n}P_{mp,IV}$) was chosen as the overall response variable; the other three electrical features were chosen as mechanism variables which include ${}^{n}I_{sc,IV}$, ${}^{n}R_{s,IV}$, and ${}^{n}V_{mp,PIV}$. These selected mechanism features are physically highly independent and related to specific degradation mechanisms. For modules in indoor accelerated exposures, these electrical features were obtained through lab characterizations. For modules exposed outdoors, these features were predicted by modeling timeseries electrical and weather data. The cross-correlation algorithm was applied to compare sixteen module variants under an outdoor exposure and two indoor accelerated exposures, including mDH and mDH+FSL. For each accelerated exposure, ten module variants are identified to have a $CCSF^{*}$ that does not appear at the guessing boundaries. Their averages are 0.4739 and 0.4298 for mDH and mDH+FSL, respectively, indicating a power reduction roughly two times faster than the outdoor exposure. Their average $CCCs$ for $< Time|{}^{n}P_{mp,IV} >$ and $< Time|{}^{n}R_{s,IV}|$ pathways are very close to one, indicating highly similar trends for how ${}^{n}P_{mp,IV}$ and ${}^{n}R_{s,IV}$ change over time for the overlapping period between the scaled indoor accelerated and outdoor exposures. However, the outdoor models in this study describe changes that are not entirely explained by degradation; there was great difficulty in robustly removing seasonality and noise over our short outdoor exposure time.

Extending outdoor exposure time is essential in order to enable seasonal decomposition and to confirm the similarity between degradation behaviors for PV modules under different exposures in this study.

7 Regression CNN & RNN of Degradation of Power and Series Resistance

Title to submit: **Comparison of Regression CNN & RNN models for Simultaneous Prediction of the Degradation of PV Module Power and Series Resistance Based on PV Images**

Electroluminescence (EL) is commonly used to detect defects in solar cells. It is popular to develop machine learning models to process these images due to the availability of large datasets in recent years. However, most research utilized convolution neural networks for defective cell classification. Few studies used images to evaluate the electrical performance of the solar cell quantitatively. Although stepwise characterizations are commonly applied to study photovoltaic (PV) module reliability under accelerated exposures, this temporal relationship has not been exploited in machine learning models developed using such datasets. This study used EL images, photoluminescence (PL) images, and electrical features collected from PV modules under stepwise accelerated exposures. Different model variants in categories of convolution neural network (CNN), recurrent neural network (RNN), and CNN+RNN were developed to predict the normalized power and series resistance using images as the input. The influence of scaling the output features and using different images as the input on the modeling performance was investigated. Combining an RNN model using a gated recurrent unit (GRU) layer with the output dimension specified as two and the raw EL images as the input is proposed as the best combination. This is determined by its lowest testing root-mean-squared error (RMSE) and less complex image processing.

7.1 Introduction

Image characterization is a powerful approach to providing spatial information about PV systems. Image characterizations commonly applied for PV reliability studies include EL, PL, and thermographic images. Thermographic images are often used to detect operational faults in PV arrays by the presence of abnormal hot spots[59]. EL is generally used to identify defective solar cells within a PV module[61]. PL is more popularly applied to silicon wafers or bare solar cells since it does not require a well electrical connection[102]. Human inspection of these images requires domain knowledge and is a time-consuming process. A convolution neural network (CNN) is a typical model that directly uses images as the input. It is known that CNN is a feed-forward neural network where each neuron merely affects the neurons nearby in the adjacent layer and retains the spatial correlation of the input images to capture local patterns[60]. The trained CNN kernel can be thought of as a filter for feature extraction. The developed CNN models to classify EL cell images were usually customized to have around five convolution layers[72, 73] or modified from published CNN models, like the VGG series[74, 75]. However, to produce optimal performance from CNNs, many images are required. Lacking enough images could lead to a worse performance[60]. In such cases, other machine learning models using feature vectors as the input could achieve comparable performance with fewer images. Some studies take texture features such as contrast, energy, homogeneity, and correlation calculated from the Gray Level Co-occurrence Matrix (GLCM) and the histogram of gradient features[61, 62]. Such feature vectors take contributions from both local and global feature extractors. Then an artificial neural network (ANN) or a simple classifier like Naive Bayes could replace the CNN to achieve comparable performance (an accuracy above 90%)[61, 62]. Most studies in this field focused on classification with targeting classes as binary[74] or multiple, like for different kinds of defects such as isolation, cracks, corrosion[72, 73]. The image data have the problem of being unbalanced in nature[74]. Image augmentation such as rotation, flipping has been shown to improve the model performance[72, 74]. While EL images used in most studies for defect classification were the single-channel grayscale images, multiple images of the same sample can be combined by merging into a single channel[76] or taking multiple channels.

Few studies have designed models to predict the change in electrical parameters through image characterizations quantitatively. There was a study that first calculated four image features, including the median intensity, the percentage of dark pixels after thresholding, the normalized busbar width, and a corrosion degree[77]. Then a model was built using image features as independent variables to predict the normalized P_{mp} and R_s through polynomial regression. The artificially defined image features have limited generality. While they worked well for the studied image dataset, in which the primary concern is corrosion, they might not work so well for another image dataset in which the primary concern is cracking. Although the images and electrical parameters in this study were obtained through stepwise characterizations of PV modules under accelerated exposures, the relationship of measurements for the same sample evaluated at different steps was not utilized[77]. Another study predicted the change in efficiency from EL images by a CNN model[103]. It first identified the location of defects and then removed them by constructing a defect-free image through the generative adversarial network (GAN). Next, the difference between the predicted efficiency from the actual image and the fake defect-free image was calculated. The model was a CNN predicting the efficiency rather than its change based on EL images. It also did not utilize the relationship of stepwise measurements for the same cell sample.

In addition, machine learning models were also widely applied to timeseries PV data for power prediction and forecast. A recurrent neural network (RNN) model is a typical neural network model type that processes timeseries data for prediction or forecast[67]. It can process variable-length input sequences using its internal state. Because the depth of an RNN neuron is decided by the length of the input sequence, which could be relatively long in some cases, a plain RNN neuron is likely to encounter a gradient vanishing problem through backpropagation. It could form a short-term memory that hinders performance improvement when training with more input data. Therefore, some special RNN neurons are more popular in RNN models such as long short-term memory unit (LSTM)[68] and gated recurrent unit (GRU)[69]. Both of them have gates using a sigmoid function to control the balance between long-term memory and the current updated state so that the information obtained from the very early input can also reach the recent output[68, 69].

This paper collected a dataset of 396 cell samples in laminated modules with images and electrical parameters measured at six steps under accelerated exposures. The developed neural network models took images as the input to predict the normalized power and series resistance. The performance of different model variants in categories of CNN, RNN, and CNN+RNN using different input images was compared. RNN models utilizing the stepwise measurements for each cell sample outperformed CNN models.

7.2 Methods

7.2.1 Minimodule Fabrication

Data for this study were acquired from stepwise characterizations applied to minimodules under indoor accelerated exposures. Each studied minimodule has four cells connected in series with five junction boxes installed on the rear side to enable each cell's current-voltage (I-V) measurement. The solar cell is either the monofacial or bifacial P-type multi-crystalline silicon PERC cell with five busbars. There are sixteen module variants of each brand with differences in module architectures (GB or DG), encapsulant materials (EVA or POE), rear encapsulant types (transparent, UV-Cutoff, or opaque), and cell types (monofacial or bifacial). There are two brands: A and B. Brand A minimodules were fabricated by a solar company using its manufacturing pipeline for commercial PV modules. Brand B minimodules were fabricated by the Solar Durability and Lifetime Extension Center (SDLE). While their fabrication steps are identical, including soldering, lamination, and junction box installation, there are differences in the finished module due to differences in soldering methods such as machine soldering or manual soldering and lamination equipment.

7.2.2 Experimental Data Acquisition

Some minimodules were exposed under an accelerated exposure named modified damp heat (mDH) with the condition of 80 °C and 85% relative humidity (RH), and the rest of the minimodules were exposed under a sequential accelerated exposure of modified damp heat with full-spectrum light (mDH+FSL). The total exposure time for each accelerated exposure was 2,520 hours, and each exposure step took 504 hours (21 days). For each exposure step under mDH+FSL, FSL took 1/3 of the exposure time, and mDH took 2/3 of the exposure time. When modules were under FSL, a 0.5 Ω resistor was connected to each module to make it operate around the maximum power (P_{mp}). The average irradiance intensity for the front and rear sides of the module under FSL were 420.4 W/m^2 and 85.1 W/m^2, respectively. At each exposure step, including the baseline, we measured current-voltage (I-V) curves at three irradiance levels, including 1000 W/m^2, 500 W/m^2, 250 W/m^2, and eight images. P_{mp} is extracted from the 1000 W/m^2 I-V curve by the $ddiv$ package[49], and series resistance (R_s) is extracted using the three I-V curves at different irradiance levels following IEC 60891. The eight images contain three electroluminescence (EL) images with three different forwarding currents, three corresponding dark images with the same camera settings and no forwarding current, and two PL images. The three forwarding currents are 9.4 A (I_o), 4.7 A (0.5 I_o), and 2.4 A (0.25 I_o). The camera exposure time was adjusted for each EL image to reasonably utilize the range of allowed image intensity. One PL image denoted as $PL@OC$ is measured under illumination with the module's current set as zero, that is, open-circuit status. Another PL image denoted as $PL@SC$ is measured under illumination with the module's voltage set as zero, that is, short-circuit status. The illumination is about twice as intense as the green light peak in the solar spectrum, provided by ten green LED lamps arranged in two columns in the imaging chamber.

7.2.3 Pre-processing of Input Images and Output Features

Fig. 3.7 shows the eight images obtained from one GB minimodule at the baseline. The power supply is connected to each module, and the obtained image is also for each module. The three EL images are denoted as $EL@I_o$, $EL@0.5I_o$, and $EL@0.25I_o$ after subtracting the corresponding dark images. A cell extraction python pipeline from $pvimage$ package[88] is applied to extract four cell images from each module image. Fig. 7.1 shows an example of the extracted cell images from a module $EL@I_o$ image.

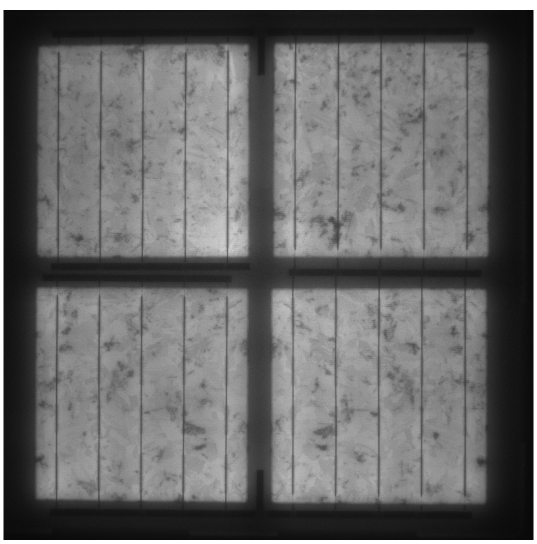

(a) Module.

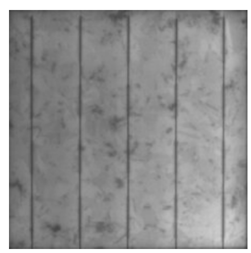

(b) Cell 4.

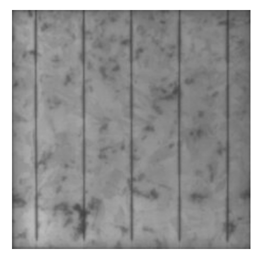

(c) Cell 3.

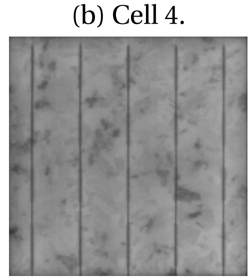

(d) Cell 1.

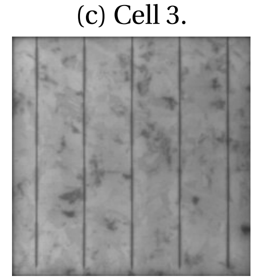

(e) Cell 2.

Figure 7.1. Extracted cell images from an $EL@I_o$ module image obtained from a glass-backsheet (GB) module measured at baseline.

In addition to the extracted $EL@I_o$ cell images used directly as the input, other images were constructed by image pre-processing to investigate potential model performance improvements, such as the baseline subtraction images, the enhanced signal-to-noise (S/N) EL images, and some hyper images. **The baseline subtraction image** is obtained by subtracting the studied image from the same type of image measured from the same sample at baseline. Then the difference was normalized by the average intensity of the baseline image. Therefore, the baseline subtraction image highlights a cell area that becomes darker after some time under an accelerated exposure. **The enhanced S/N EL image** is a weighted average of the three EL images measured with different forwarding currents. The weights are the reciprocal of their corresponding camera exposure times. Table 7.1 lists the camera exposure time of these three EL images for modules with monofacial cells and bifacial cells, which is the only difference in the settings of the camera for three EL images with different forwarding currents. The enhanced S/N image is calculated by Eq. 7.1 to form a weighted average of the three EL images as a single-channel image, where the bit parameter is 16 for our images. Fig. 7.2 shows the extracted $EL@I_o$ cell image of one solar cell after five steps of mDH exposure, the corresponding baseline subtraction image, and the enhanced S/N EL image. **The hyper image** is constructed by putting different types of images into multiple image channels. Double-channel hyper images using the combination of $EL@I_o$ and $EL@0.25I_o$, and $EL@I_o$ and $PL@OC$ after the baseline subtraction were constructed in the study.

Table 7.1. Camera exposure times of different EL images for modules with monofacial cells and bifacial cells.

Image Type	Cell Type	Camera Exposure Time (second)
$EL@I_o$	monofacial	4.0
$EL@0.5I_o$	monofacial	9.0
$EL@0.25I_o$	monofacial	19.0
$EL@I_o$	bifacial	2.2
$EL@0.5I_o$	bifacial	5.0
$EL@0.25I_o$	bifacial	13.0

$$\begin{aligned} monofacial: & \frac{\frac{19.0}{4.0}EL@I_o + \frac{19.0}{9.0}EL@0.5I_o + \frac{19.0}{19.0}EL@0.25I_o}{(\frac{19.0}{4.0} + \frac{19.0}{9.0} + \frac{19.0}{19.0}) \times (2^{bit} - 1)} \\ bifacial: & \frac{\frac{13.0}{2.2}EL@I_o + \frac{13.0}{5.0}EL@0.5I_o + \frac{13.0}{13.0}EL@0.25I_o}{(\frac{13.0}{2.2} + \frac{13.0}{5.0} + \frac{13.0}{13.0}) \times (2^{bit} - 1)} \end{aligned} \tag{7.1}$$

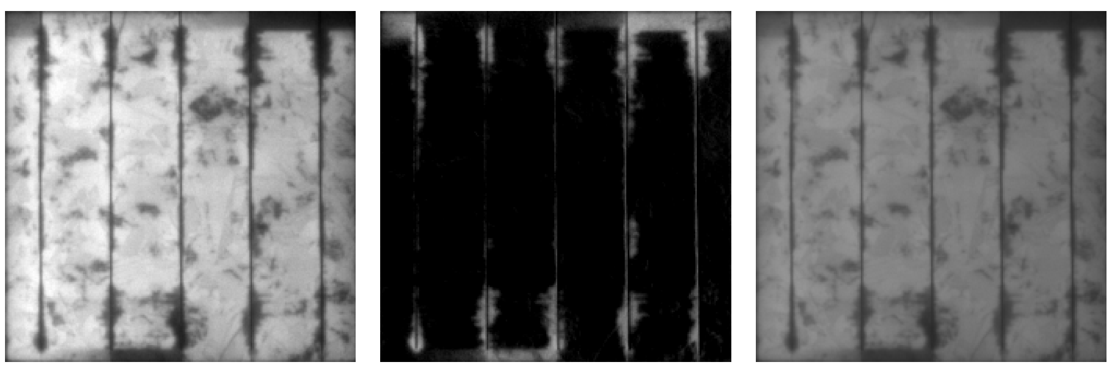

(a) Raw. (b) Baseline subtraction. (c) Enhanced S/N EL.

Figure 7.2. The raw $EL@I_o$ image (a), the baseline subtraction image (b), and the enhanced S/N EL image (c) for a solar cell in a laminated module after five steps of mDH exposure.

The normalized P_{mp} (${}^{n}P_{mp,IV}$) and R_s (${}^{n}R_{s,IV}$) were chosen as the predicted output features. These electrical features were normalized by the feature value measured from the same cell at baseline. Two kinds of scaling methods were tested for the output to explore the potential improvements in model performance, including the minimum-maximum scaler (MMS) shown in Eq. 7.2 and the standard scaler (STS) shown in Eq. 7.3. The scaler translates each feature individually, denoted as X in Eq. 7.2 and Eq. 7.3 using the statistics obtained from the training dataset, such as the range, the average (μ), and the standard deviation (σ).

$$X_{scaled} = \frac{X - min(X)}{max(X) - min(X)} \tag{7.2}$$

$$X_{scaled} = (x - \mu)/\sigma \tag{7.3}$$

7.2.4 Neural Network Models

The convolution neural network (CNN) is designed to automatically and adaptively learn spatial hierarchies of features through backpropagation by using multiple building blocks, such as convolution layers, pooling layers, and dense layers[104]. In this study, multiple modifications were applied to CNN models to explore potential model performance improvements, including adding dropout layers, changing the number of neurons in dense layers, alternating the grid size in max-pooling layers, adding different regularization and batch normalization, and changing convolution structures. The simplest and the most complex CNN models in this study contain two and seven convolution layers shown in Fig. 7.3. For CNN model expressions, the letter "c" stands for the convolution layer, and the letter "p" stands for the max-pooling layer with the following number as the layer order.

The recurrent neural networks (RNN) is a class of artificial neural networks (ANNs) where connections between neurons form a directed or undirected graph along the sequence of input. A sequence is a particular order in which one thing follows another.

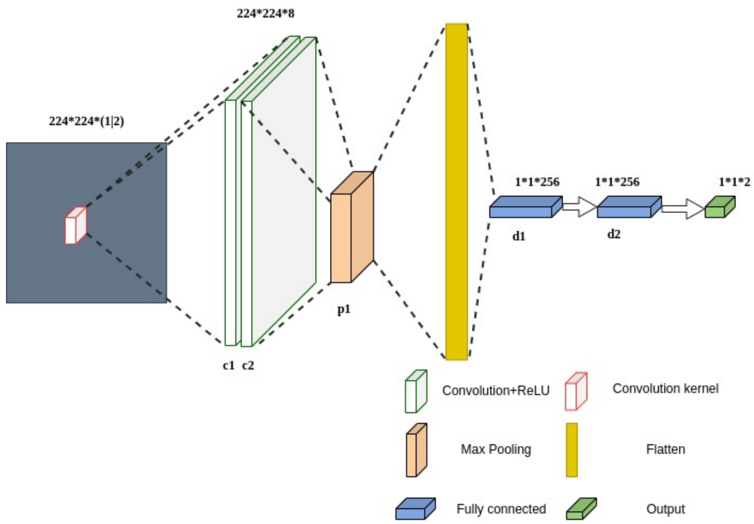

(a) c1c2p1.

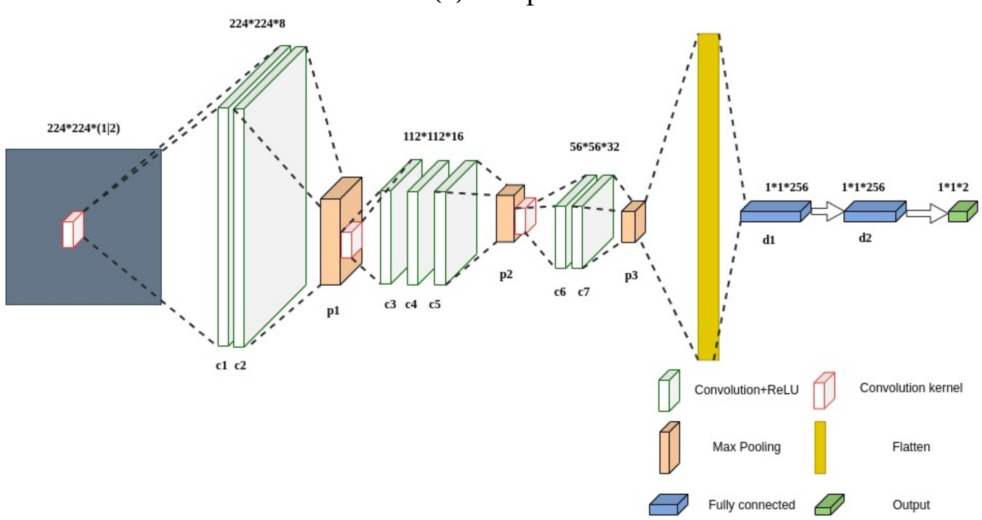

(b) c1c2p1c3c4p2c6c7p3.

Figure 7.3. The model architecture for the simplest and most complex CNN models.

The most common sequential input is timeseries data such as audio, video, and the daily stock price. A usual RNN neuron takes the current input like a typical feed-forward neural network and information from the previous input to predict the current output. So it exhibits temporal dynamic behavior and owns a memory. It is well known that a very deep feed-forward neuron network suffers from the vanishing gradient problem.

A usual RNN neuron will easily encounter the same issue. Its internal state can keep a short-term memory since its depth is decided by the length of the input sequence, which can be long in nature. Besides dividing a long input sequence into multiple short input sequences, two specially designed RNN neurons are applied more often to enable long-term memory. They are long short-term memory unit (LSTM) [68] and gated recurrent unit (GRU) [69] which can balance the contribution of the long-term memory, the short-term memory, and the current input to predicting the current output. GRU is used here due to its concise structure and fewer parameters. The number of parameters in a GRU neuron is decided by the input dimension and the specified output dimension, defined in the "units" parameter in the "tf.keras.layers.GRU" function. Performance of RNN models was investigated with units changed as two, 20, and 200 for a single GRU layer and the number of GRU layers chosen from one to three. The image dataset needs to be reorganized into a video format to train an RNN model. The video is for each solar cell with frames of images following the order of exposure steps.

Model Performance Matrix: The data of 396 solar cell samples were partitioned into training, validation, and testing datasets according to a 75:15:15 ratio based on randomly selected cells. Then rotations of 90°, 180°, and 270° were applied to each image to increase the number of observations and make the model generalized across different image orientations. Therefore, there were 1108 videos or 6648 images for training, 236 videos or 1416 images for validation, and 240 videos or 1440 images for testing. Mean squared error (MSE) calculated by Eq. 7.4 was used as the loss function in the training process. The model performance was evaluated using the root-mean-square error (RMSE) shown in Eq. 7.5 obtained from the testing dataset. In both Eq. 7.4 and Eq. 7.5, n is the number of observations in the dataset, Y_i is the actual output feature value, and

$\hat{Y}_i$ is the predicted output feature value. The number of epochs in the training process is denoted by a number in parentheses following the model expression. Models returned from checkpoints, denoted by a letter "c" following the defined training epoch number, were sometimes used to obtain models before overfitting. The checkpoint was set to continuously save model objects with a smaller MSE for the validation dataset in the training process.

$$MSE = \frac{1}{n}\sum_{i=1}^{n}(Y_i - \hat{Y}_i)^2 \tag{7.4}$$

$$RMSE = \sqrt{\frac{\sum_{i=1}^{n}(Y_i - \hat{Y}_i)^2}{n}} \tag{7.5}$$

Model Fitting Environment: Tensorflow 2.6.1 library was used for building the neural network model[105]. The model was trained and tested on Intel(R) Xeon(R) CPU E5-2630 v4 @ 2.20GHz, 64 GB memory, 8 CPU cores, and 12 GB Nvidia GeForce RTX 2080 GPU card.

7.3 Results

A baseline model was made by guessing values of output features as one, and its testing RMSE is 0.0958. The specification of all cases with differences in the model structure, input, and output is described in Table 7.2 with the testing RMSE. "Raw" is for the original image in the input column, and "BS" is for the baseline subtraction image. "Hyper" is for the image with multiple channels for different image characterizations, and "EH" is for the enhanced S/N EL image constructed by the three EL images with different forwarding currents. The normalized electrical features were used directly as the output if the output column was left empty. Otherwise, a scaler was applied, where MMS represents the minimum-maximum scaler as Eq. 7.2 and STS represents the standard scaler as Eq. 7.3. The convolution structures for CNN#1 to CNN#10 are described in Table 7.4. This section organizes results based on model categories, including CNN, RNN, and CNN+RNN.

7.3.1 CNN Model Variants

The experimental cases for CNN models include the first 42 rows in Table 7.2. Most CNN models use the baseline subtraction images as the input for model performance comparison. Table 7.3 shows the number of parameters in each layer in CNN#1 using single-channel images as the input. CNN#1 has five convolution layers separated by two max-pooling layers with a grid size of two by two. Its convolution part is followed by two dense layers with the number of neurons specified as 256 for each layer. Its output layer has two neurons for ${}^{n}P_{mp,IV}$ and ${}^{n}R_{s,IV}$. The activation function for the output layer and all the other layers is linear and rectified linear unit (ReLU), respectively.

Fig. 7.4 compares the testing RMSEs of the first six cases in Table 7.2, which contain several modifications applied to CNN#1. These modifications are adding dropout layers (case 2), reducing neurons in dense layers (cases 3 and 4), and enlarging the grid in max-pooling layers (cases 5 and 6). The red line in Fig. 7.4 marks the performance of the baseline model. These six cases all have similar learning curves, as shown in Fig. 7.7a, which show a sign of overfitting within 50 epochs. Therefore, more operations such as batch normalization, kernel regularization, and activation regularization were tested as possible solutions to delay overfitting and to improve model performance through more epochs of training. Batch normalization has two notations based on the added position

Table 7.2. The specification of each modeling experiment and its resulting testing RMSE.

Case	Model Expression	Comments	Input	Output	# of Parameters	RMSE
1	CNN#1(50)		BS($EL@I_o$)		12,918,090	0.0844
2	CNN#1+0.5D(50)	add dropout layer (50%) following each dense layer	BS($EL@I_o$)		12,918,090	0.0735
3	CNN#1+0.5D+RF1(50)	reduce neurons in the first dense layer from 256 to 128	BS($EL@I_o$)		6,462,666	0.0758
4	CNN#1+0.5D+RF2(50)	reduce neurons in the second dense layer from 256 to 128	BS($EL@I_o$)		12,884,938	0.0741
5	CNN#1+0.5D+MP3(50)	change the grid in max-pooling as 3 × 3	BS($EL@I_o$)		2,633,034	0.0777
6	CNN#1+0.5D+MP4(50)	change the grid in max-pooling as 4 × 4	BS($EL@I_o$)		875,850	0.0780
7	CNN#1+0.5D+KR(50)	add kernel regularization to each convolution layer	BS($EL@I_o$)		12,918,090	0.0742
8	CNN#1+0.5D+AR(50)	add activation regularization to each convolution layer	BS($EL@I_o$)		12,918,090	0.0788
9	CNN#1+0.5D+BNB16(50)	add BNB with a batch size of 16	BS($EL@I_o$)		12,918,186	0.0783
10	CNN#1+0.5D+BNB64(50)	add BNB with a batch size of 64	BS($EL@I_o$)		12,918,186	0.1154
11	CNN#1+0.5D+BNB256(50)	add BNB with a batch size of 256	BS($EL@I_o$)		12,918,186	0.1154
12	CNN#1+0.5D+BNB512(50)	add BNB with a batch size of 512	BS($EL@I_o$)		12,918,186	0.2017
13	CNN#1+0.5D+BNB1024(50)	add BNB with a batch size of 1024	BS($EL@I_o$)		12,918,186	0.5036
14	CNN#1+0.5D+BN16(50)	add BN with a batch size of 16	BS($EL@I_o$)		12,918,346	0.0779
15	CNN#1+0.5D+BN64(50)	add BN with a batch size of 64	BS($EL@I_o$)		12,918,346	0.0783
16	CNN#1+0.5D+BN256(50)	add BN with a batch size of 256	BS($EL@I_o$)		12,918,346	0.0792
17	CNN#1+0.5D+BN512(50)	add BN with a batch size of 512	BS($EL@I_o$)		12,918,346	0.0851
18	CNN#1+0.5D+BN1024(50)	add BN with a batch size of 1024	BS($EL@I_o$)		12,918,346	0.3259
19	CNN#1+0.5D(50)	add dropout layer (50%) following each dense layer	BS($EL@I_o$)	STS	12,918,090	0.0778
20	CNN#1+0.5D+BNB512(50)	add BNB with a batch size of 512	BS($EL@I_o$)	STS	12,918,186	0.0738
21	CNN#1+0.5D+BN512(50)	add BN with a batch size of 512	BS($EL@I_o$)	STS	12,918,346	0.0778
22	CNN#1+0.5D(50)	add dropout layer (50%) following each dense layer	BS($EL@I_o$)	MMS	12,918,090	0.0757
23	CNN#1+0.5D+BNB512(50)	add BNB with a batch size of 512	BS($EL@I_o$)	MMS	12,918,186	0.0788
24	CNN#1+0.5D+BN512(50)	add BN with a batch size of 512	BS($EL@I_o$)	MMS	12,918,346	0.0951
25	CNN#1+0.5D+BNB512(250)	add BNB with a batch size of 512	BS($EL@I_o$)		12,918,186	0.0787
26	CNN#1+0.5D+BN512(250)	add BN with a batch size of 512	BS($EL@I_o$)		12,918,346	0.0798
27	CNN#1+0.5D(50c)	add dropout layer (50%) following each dense layer	BS($EL@I_o$)		12,918,090	0.0749
28	CNN#2+0.5D(50c)	add dropout layer (50%) following each dense layer	BS($EL@I_o$)		25,757,338	0.0730
29	CNN#3+0.5D(50c)	add dropout layer (50%) following each dense layer	BS($EL@I_o$)		25,757,922	0.0742
30	CNN#4+0.5D(50c)	add dropout layer (50%) following each dense layer	BS($EL@I_o$)		12,912,866	0.0738
31	CNN#5+0.5D(50c)	add dropout layer (50%) following each dense layer	BS($EL@I_o$)		12,918,674	0.0737
32	CNN#6+0.5D(50c)	add dropout layer (50%) following each dense layer	BS($EL@I_o$)		12,916,354	0.0752
33	CNN#7+0.5D(50c)	add dropout layer (50%) following each dense layer	BS($EL@I_o$)		12,915,770	0.0754
34	CNN#8+0.5D(50c)	add dropout layer (50%) following each dense layer	BS($EL@I_o$)		6,494,879	0.0737
35	CNN#9+0.5D(50c)	add dropout layer (50%) following each dense layer	BS($EL@I_o$)		6,507,130	0.0738
36	CNN#10+0.5D(50c)	add dropout layer (50%) following each dense layer	BS($EL@I_o$)		6,516,378	0.0734
37	VGG16(T)+0.5D(50c)	trainable VGG16 with the same top layers structure	BS($EL@I_o$)		21,203,778	0.0756
38	VGG16(NT)+0.5D(50c)	non-trainable VGG16 with the same top layers structure	BS($EL@I_o$)		21,203,778	0.0777
39	CNN#1+0.5D(50c)		Raw($EL@I_o$)		12,918,090	0.0768
40	CNN#1+0.5D(50c)		EH		12,918,090	0.0860
41	CNN#1+0.5D(50c)	channel 0: BS($EL@I_o$); channel 1: BS($EL@0.25I_o$)	Hyper		12,918,162	0.0923
42	CNN#1+0.5D(50c)	channel 0: BS($EL@I_o$); channel 1: BS($PL@OC$)	Hyper		12,918,162	0.0922
43	RNN#1(50c)	one GRU layer with units as two	Raw($EL@I_o$)		301,236	0.0593
44	RNN#2(50c)	one GRU layer with units as 20	Raw($EL@I_o$)		3,013,332	0.0597
45	RNN#3(50c)	one GRU layer with units as 200	Raw($EL@I_o$)		30,241,212	0.0631
46	RNN#4(50c)	two GRU layer with units for each layer as two	Raw($EL@I_o$)		301,272	0.0593
47	RNN#5(50c)	three GRU layer with units for each layer as two	Raw($EL@I_o$)		301,308	0.0605
48	RNN#1(50c)	one GRU layer with units as two	BS($EL@I_o$)		301,236	0.0616
49	RNN#1(50c)	one GRU layer with units as two	EH		301,236	0.0593
50	CNN#1+0.5D+RNN#1(50c)	combine CNN#1 before the output layer and RNN#1	BS($EL@I_o$)		12,919,292	0.0599
51	CNN#1+0.5D+RNN#1(50c)	combine CNN#1 before the output layer and RNN#1	Raw($EL@I_o$)		12,919,292	0.0594
52	CNN#1+0.5D+RNN#1(50c)	combine CNN#1 before the output layer and RNN#1	EH		12,919,292	0.0596
53	RNN#1(50c)	similar to case 43 with original resolution images as input	Raw($EL@I_o$)		13,231,530	0.0593
54	RNN#1(50c)	similar to case 49 with original resolution images as input	EH		13,231,530	0.0592

in a model structure. BNB is for adding batch normalization to each convolution block before each max-pooling layer. BN is for adding batch normalization following each convolution layer. The number following BN or BNB is the batch size, which was turned

Table 7.3. The number of parameters in each layer for CNN#1.

Layer	Output Shape	# of Parameters
Input	224 × 224 × 1	0
Convolution layer 1	224 × 224 × 8	80
Convolution layer 2	224 × 224 × 8	584
Max pooling	112 × 112 × 8	0
Convolution layer 3	112 × 112 × 16	1,168
Convolution layer 4	112 × 112 × 16	2,320
Convolution layer 5	112 × 112 × 16	2,320
Max pooling	56 × 56 × 16	0
Flatten	50,176	0
Dense layer 1	256	12,845,312
Dense layer 2	256	65,792
Output	2	512

from 16 to 1024. The momentum in batch normalization was set as 0.9. Fig. 7.5 shows the performance comparison of adopting kernel regularization (case 7), activation regularization (case 8), and two kinds of batch normalization with different batch sizes (cases 9 to 18).

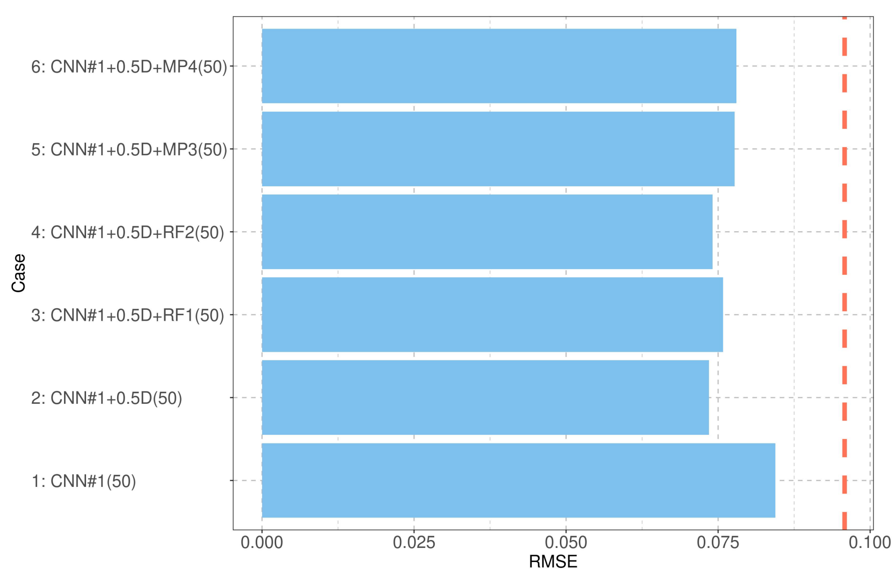

Figure 7.4. Comparison of the testing RMSEs for adding dropout layers and modifying dense layers and max-pooling layers in CNN#1.

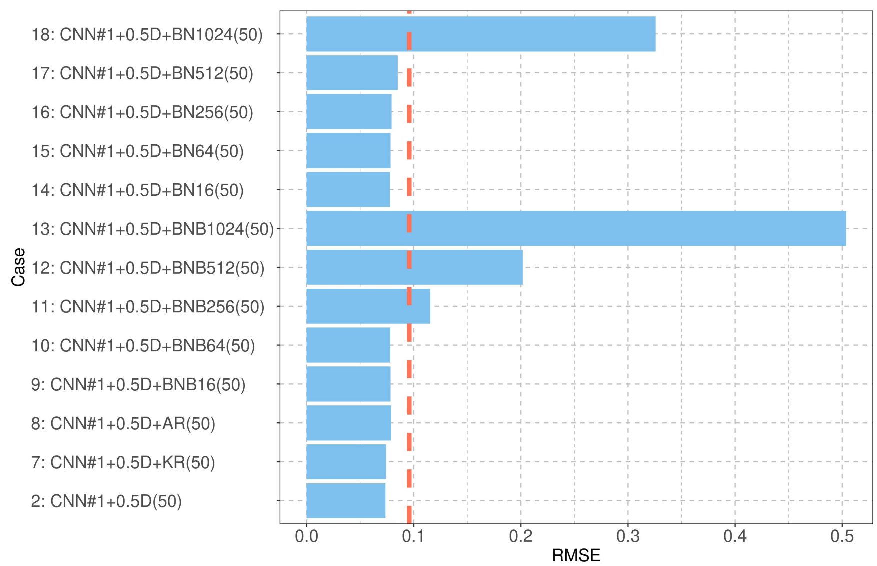

Figure 7.5. Comparison of the testing RMSEs for adopting kernel regularization, activation regularization, and batch normalization in CNN#1.

In the training dataset, ${}^{n}P_{mp,IV}$ and ${}^{n}R_{s,IV}$ have averages as 0.970 and 1.073, respectively. Cases 19 to 24 in Table 7.2 scale the output features and obtain the testing RMSE using three models. Their testing RMSEs are presented in Fig. 7.6. Fig. 7.7c shows the influence of scaling the output features by MMS on the learning curves of CNN#1+0.5D+BNB512. In Fig. 7.7, the purple point marks the epoch with the minimal MSE for the validation dataset. In Fig. 7.7b and Fig. 7.7c, the scale of the training MSE is on the left side in red, and that of the validating MSE is on the right side in green.

Table 7.4 lists the model structures of the convolution parts for CNN#1 to CNN#10. These CNN models have differences in the numbers of convolution layers varied from two to seven and the numbers and positions of max-pooling layers. VGG16 is a published CNN model with 13 convolution layers and five max-pooling layers[106]. The parameters in its convolution part can be fixed by specifying the weights parameter in the "VGG16" function as "imagenet" in non-trainable (NT) mode. These parameters

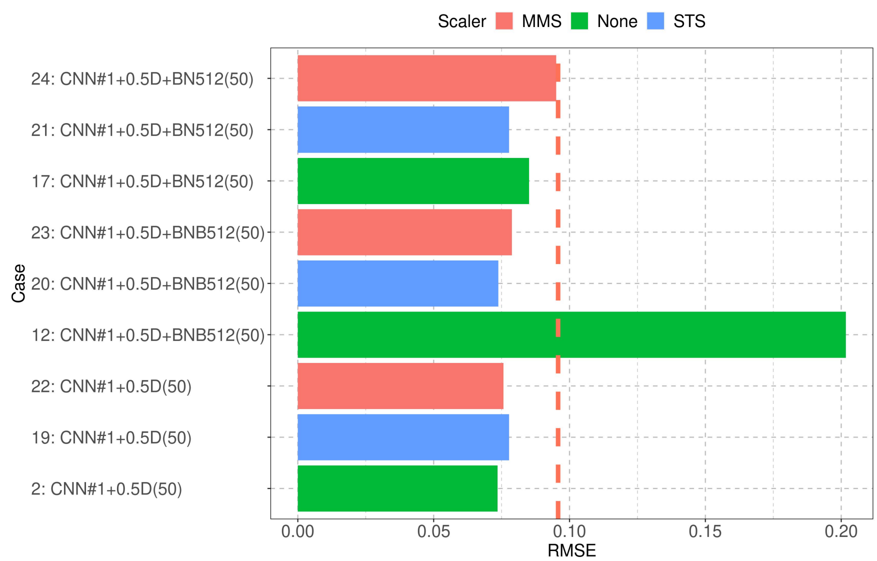

Figure 7.6. Comparison of the testing RMSEs by scaling the output feature using three models.

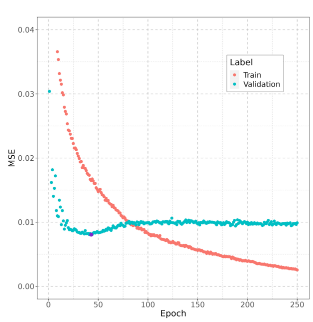

(a) CNN#1+0.5D.

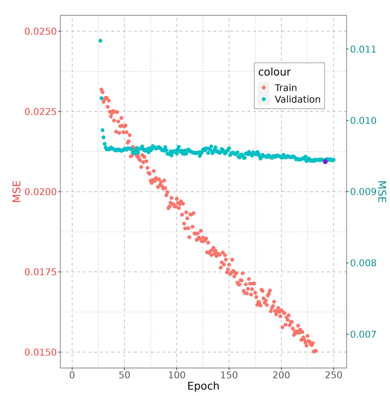

(b) CNN#1+0.5D+BNB512.

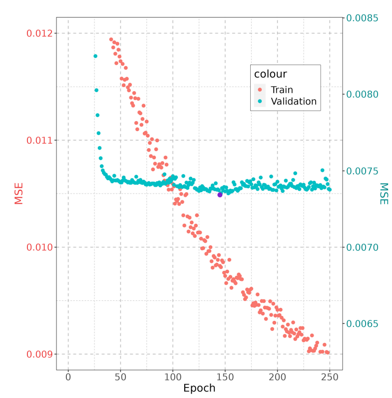

(c) CNN#1+0.5D+BNB512&MMS.

Figure 7.7. The learning curves after adopting batch normalization and the minimum-maximum scaler to CNN#1+0.5D.

certainly can be trained in trainable (T) mode. Fig. 7.8 compares the testing RMSEs of these models with different convolution structures only using the model object returned in the latest checkpoint during 50 epochs of training. The results presented in Fig. 7.8 correspond to cases 27 to 38 in Table 7.2.

Table 7.4. The model expressions for the convolution parts in CNN#1 to CNN#10.

ID	Model Expression
CNN#1	c1c2p1c3c4c5p2
CNN#2	c1c2p1
CNN#3	c1c2c3p1
CNN#4	c1p1c2p2
CNN#5	c1c2c3p1c4c5c6p2
CNN#6	c1c2c3p1c4c5p2
CNN#7	c1c2p1c3c4p2
CNN#8	c1p1c2p2c3p3
CNN#9	c1c2p1c3c4p2c5c6p3
CNN#10	c1c2p1c3c4c5p2c6c7p3

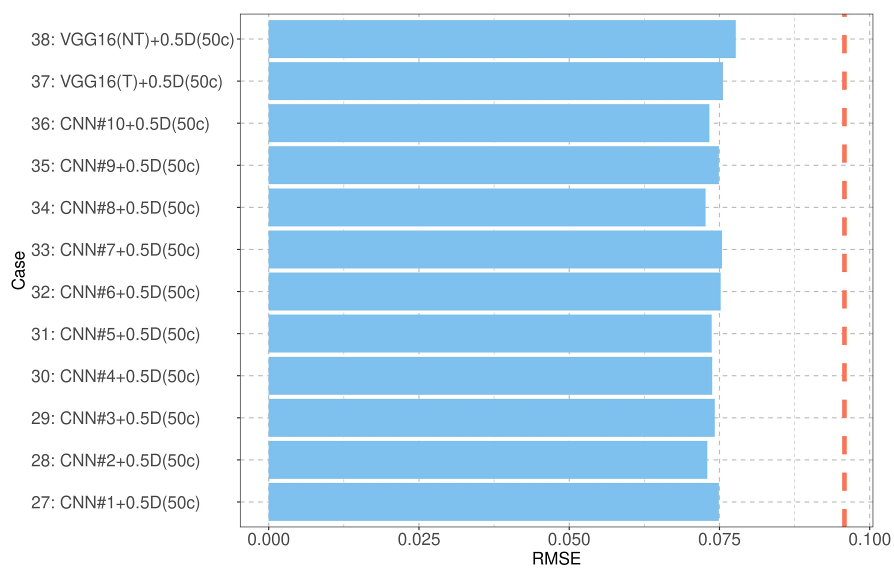

Figure 7.8. Comparison of the testing RMSEs for CNN models with different convolution structures.

Using CNN#1+0.5D returned at the latest checkpoint during 50 epochs of training, the testing RMSEs are compared using different images as the input. The results are presented in Fig. 7.9 and recorded as cases 39 to 42 in Table 7.2 with a detailed description of the input images.

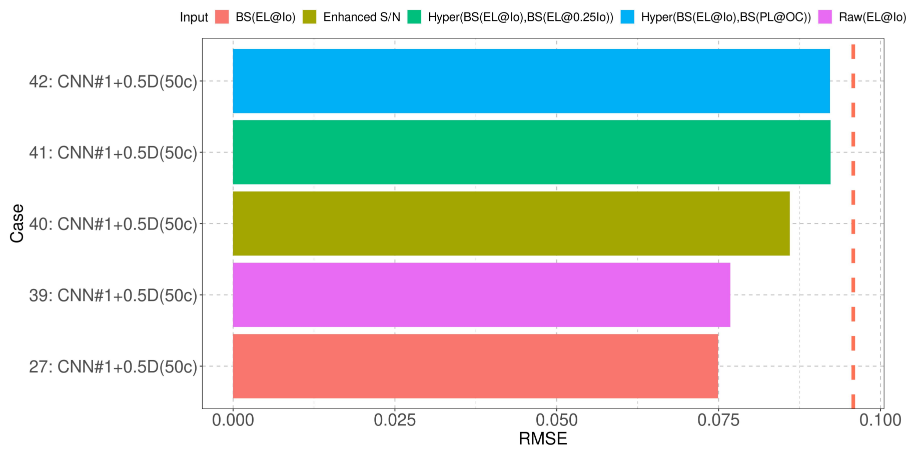

Figure 7.9. Comparison of the testing RMSEs for different kinds of images as the input using CNN#1+0.5D model returned at the latest checkpoint during 50 epochs of training.

7.3.2 RNN Model Variants

In Table 7.2, cases 43 to 47 have results for five RNN models with differences in their output dimensions and numbers of GRU layers using the raw $EL@I_o$ images as the input. RNN models in cases 43, 44, and 45 only have one GRU layer, but their output dimensions are two, 20, and 200, respectively. Cases 43, 46, and 47 have the same output dimension as two, but different numbers of GRU layers as one, two, and three, respectively. The specification of each layer in RNN#1 is listed in Table 7.5, and its learning curves are shown in Fig. 7.11a using the raw $EL@I_o$ images as the input. The testing RMSEs of these RNN models using the raw $EL@I_o$ image are shown in Fig. 7.10. The influence of different image inputs on the model performance is investigated using RNN#1. The results are compared in Fig. 7.12 and listed in cases 43, 48, and 49 in Table 7.2 for using the raw $EL@I_o$ images, the baseline subtraction $EL@I_o$ images, and the enhanced S/N EL images, respectively.

Table 7.5. The number of parameters in each layer for RNN#1.

Layer	Output Shape	# of Parameters
Input	6×50176	0
GRU	6×2	301080
Flatten	12	0
Dense layer	12	156
Reshape	6×2	0

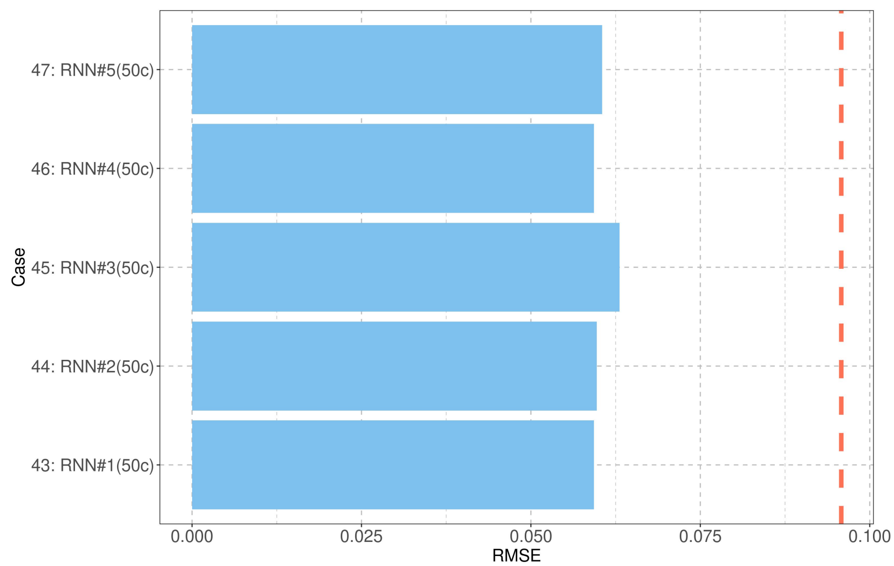

Figure 7.10. Comparison of the testing RMSEs of RNN models with differences in the number and the output dimension of GRU layers using the raw $EL@I_o$ images as the input.

7.3.3 CNN+RNN Model Variants

Cases 50 to 52 in Table 7.2 show results of a combined model of CNN and RNN using different input images, including the raw $EL@I_o$ images, the baseline subtraction $EL@I_o$ images, and the enhanced S/N EL images. The combined model takes all layers in CNN#1 described in Table 7.3 except the output layer, followed by the RNN#1 model structure described in Table 7.5 without the input layer. Fig. 7.11b shows the learning curve for the combined model with the raw $EL@I_o$ images as the input. The testing RMSEs for models selected in the three major categories as CNN, RNN, and CNN+RNN with three kinds of image inputs are compared in Fig. 7.12.

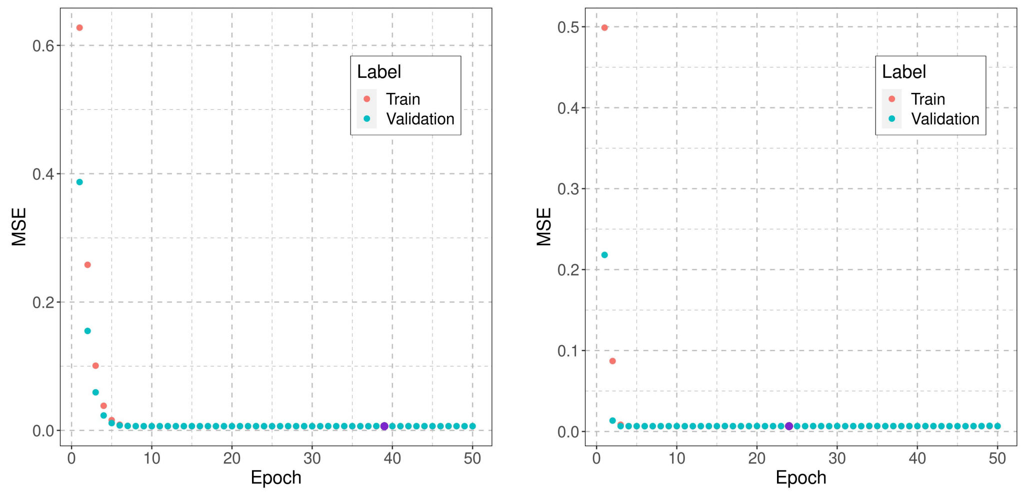

(a) RNN#1.

(b) CNN#1+0.5D+RNN#1.

Figure 7.11. The learning curves for RNN#1 and CNN#1+0.5D+RNN#1 up to 50 epochs of training using the raw $EL@I_o$ image as the input.

7.4 Discussion

7.4.1 Model Performance with Scaled Output Features

In this study, the goal is to accurately predict the ${}^{n}P_{mp,IV}$ and ${}^{n}R_{s,IV}$ using image characterizations as the input. Based on our accelerated exposure conditions, the degradation of solar cells leads to a reduction in power (P_{mp}) and an increase in series resistance (R_s), causing an average ${}^{n}P_{mp,IV}$ lower than one and an average ${}^{n}R_{s,IV}$ higher than one after exposures. Two approaches were applied to scale each normalized electrical feature, including the minimum-maximum scaler (MMS) and the standard scaler (STS).

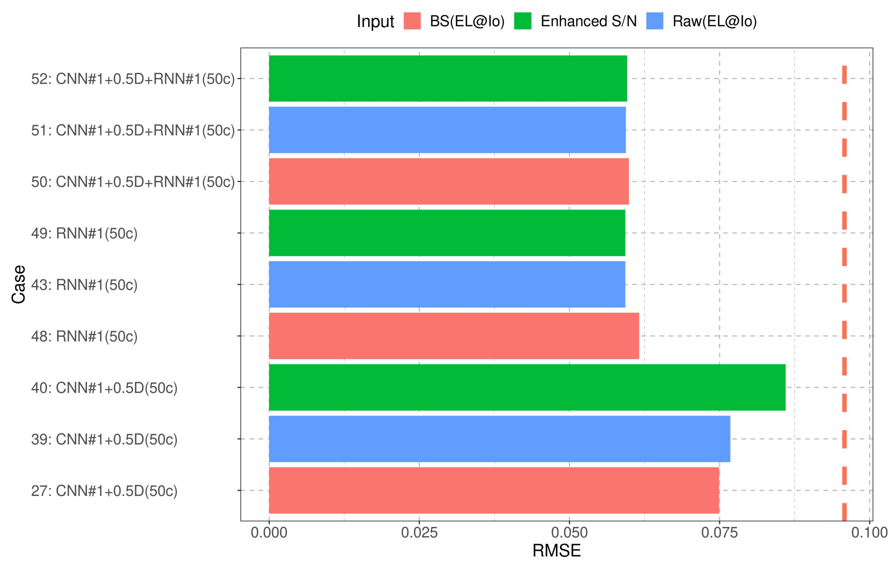

Figure 7.12. Comparison of the testing RMSEs of CNN, RNN and CNN+RNN model examples with three kinds of input images, including the raw $EL@I_o$ images, the baseline subtraction $EL@I_o$ images, and the enhanced S/N EL images.

MMS scales each feature into the range from zero to one using the minimum and maximum of its original values. STS centers each feature at zero and then scales the data to make its standard deviation as one. The effect on model performance by scaling the output feature was studied using three models: CNN#1+0.5D, CNN#1+0.5D+BNB512, and CNN#1+0.5D+BN512.

Fig. 7.6 shows the comparison of the testing RMSEs for these three models after 50 epochs of training with different scalers applied to the output features. Scaling output features for CNN#1+0.5D increases the testing RMSE, bringing no model performance improvement. CNN#1+0.5D+BNB512 model has the batch normalization operation added before each max-pooling layer compared to CNN#1+0.5D. Using the scaled output features significantly reduces the testing RMSE for the model obtained after 50 epochs of training. As can be seen in the learning curves shown in Fig. 7.7b and Fig. 7.7c, using the MMS scaled output features can speed up the convergence of the validating MSE. The validating MSE drops rapidly in the first 30 epochs of training and then slowly decreases, with a minimum appearing at the 242nd epoch in Fig. 7.7b. In Fig. 7.7c, the validating MSE transients from the fast dropping stage to the slowly dropping stage more smoothly, and its minimum appears at the 145th epoch training. CNN#1+0.5D+BN512 adds the batch normalization after each convolution layer compared to CNN#1+0.5D. The testing RMSEs in cases 24 and 26 in Table 7.2 show that the testing RMSE is smaller for the model with more epochs of training. So CNN#1+0.5D+BN512 has not yet overfitted within 50 epochs of training. Compared to the RMSE of CNN#1+0.5D+BN512 model using the normalized output features in Fig. 7.6, the STS scaler is found to speed up the convergence of model performance. However, scaling the output feature does not improve the model's performance even when trained with four times more epochs. The testing RMSEs of the model returned at the purple point in Fig. 7.7b and Fig. 7.7c are 0.0787 and 0.0784, respectively. Both are higher than 0.0749 for that in Fig. 7.7a, which is for CNN#1+0.5D without batch normalization and output feature scaling.

7.4.2 Performance of Model Variants: CNN, RNN, and CNN+RNN

In addition to the convolution layer, a CNN model can also contain max-pooling layers, dropout layers, and dense layers. This study first adjusted layers outside the convolution part to study other layers' influence on model performance, and the results are shown in Fig. 7.4. Adding a dropout layer after each dense layer reduces the testing RMSE from 0.0844 to 0.0735, improving the model performance. Other modifications, such as reducing the number of neurons in dense layers or increasing the grid size in max-pooling layers, do not improve the model performance. All studied models in Fig. 7.4 have a sign of overfitting within 50 epochs of training. The learning curves of 250 epochs of training for CNN#1+0.5D are presented in Fig. 7.7a. While the training MSE has been continuously decreasing, the validating MSE has a trend of first rising and then stabilizing after the purple point, with the lowest MSE for the validation data appearing at the 43rd epoch.

Kernel regularization, activation regularization, and batch normalization with different adding positions and batch sizes were examined to explore the chances of solving the early overfitting problem so that the model can be improved through more epochs of training. From Fig. 7.5, it can be observed that only when the batch size is large enough does the testing RMSE become significantly different from that of CNN#1+0.5D. For the model with BNB, which is for adding batch normalization before each max-pooling layer, the batch size needs to be larger or equal to 256. For the model with BN, which is for adding batch normalization after each convolution layer, the batch size needs to be as large as 1024. Fig .7.7b shows the learning curve for CNN#1+0.5D+BNB512 of up to 250 epochs of training. The validating MSE declines rapidly in the first 30 epochs, then gradually decreases. It is worth noting that the training and validating MSE curves in Fig. 7.7b and Fig. 7.7c use different scales and do not intersect. The training MSE curve is higher than the validating MSE curve numerically. Comparing the testing RMSEs in cases 25 and 26 to case 2 listed in Table 7.2, batch normalization does not bring an improvement in the model performance. After extending the training epochs by five times, the testing RMSE for the model with batch normalization added is still higher than that for the model without batch normalization. Therefore, the influence of modifying the convolution part on the CNN model performance was investigated without adding batch normalization.

Cases 27 to 36 in Table 7.2 show results of ten CNN models with differences in the convolution part. The structure of their convolution parts is described in Table 7.4. Among these ten CNN models, CNN#2 has the simplest structure with only two convolution layers and one max-pooling layer, and CNN#10 has the most complex structure with seven convolution layers and three max-pooling layers. The first dense layer after the flatten layer contributes the most parameters. For example, the first dense layer occupies 99.4% of the total number of parameters in CNN#1 as described in Table 7.3. Therefore, more max-pooling layers reduce the total number of parameters. The number of parameters for CNN#2+0.5D is about four times that for CNN#10+0.5D. However, these ten CNN models are less complex than the VGG16, which contains 13 convolution layers and five max-pooling layers. The total number of parameters for VGG16 is comparable to that for CNN#2 due to its significantly more kernels in each convolution layer. However, for the VGG16 in non-trainable mode, the trainable parameters are only 6,489,090, similar to CNN#10, out of 21,203,778 parameters in total. As shown in Fig. 7.8, CNN#1 to CNN#10 perform very similarly. Their testing RMSEs have a minimum of 0.0730 for CNN#2 and a maximum of 0.0754 for CNN#7. Furthermore, the most complex VGG16 in both modes has a higher testing RMSE than CNN#1 to CNN#10. Therefore, increasing the complexity of convolution structures does not improve the performance of CNN models.

RNN models' performance was investigated using the raw $EL@I_o$ images as the input and five RNN models with different complexities. The results are reported in cases 43 to 47 in Table 7.2 and compared in Fig. 7.10. The GRU layer occupies most parameters when its output dimension is not too large, like RNN#1 introduced in Table 7.5, differentiated from CNN models. In Fig. 7.10, RNN#1 and RNN#4 are found to have the lowest testing RMSE, both of which are 0.0593. Therefore, increasing the output dimension and the number of GRU layers beyond the settings of RNN#1 does not help the model performance. Moreover, the number of parameters of RNN#1 is only 4.64% of that of CNN#8+0.5D, which is the CNN model with the least number of parameters. From the learning curves of RNN#1 shown in Fig. 7.11a using the raw $EL@I_o$ as the input, it can be seen that RNN#1 reaches a stable state within 50 epochs of training.

In addition, the CNN#1+0.5D+RNN#1 model is built by removing the output layer in CNN#1+0.5D and then using it as the input for RNN#1. Its learning curves using the raw $EL@I_o$ images are shown in Fig. 7.11b. The model also reaches a stable region within 50 epochs of training. The results of CNN#1+0.5D+RNN#1 using different kinds of images as the input are recorded in cases 50 to 52 in Table 7.2. Fig. 7.12 compares the testing RMSEs for three selected CNN, RNN, and CNN+RNN models. CNN#1+0.5D+RNN#1 performs similarly to RNN#1, and both have a testing RMSE that is significantly lower than that of CNN#1+0.5D.

7.4.3 Model Performance with the Raw and the Baseline Subtraction Image

As shown in Fig. 7.12, using the baseline subtraction $EL@I_o$ images leads to a testing RMSE that is slightly smaller than that of using the raw $EL@I_o$ for CNN#1+0.5D. The predicted output in our study is the normalized electrical feature, which measures the relative change for a sample after accelerated exposures. The baseline subtraction $EL@I_o$ image is also an approach to quantify a relative change in the image characterization, which could contribute to its better performance working with CNN models.

Using the raw $EL@I_o$ images in RNN#1 has a smaller testing RMSE than using the baseline subtraction $EL@I_o$ images. The RNN model has the essential property of building internal memory to identify changes in the input time sequence. The result indicates that RNN models find more helpful information in the raw $EL@I_o$, contributing to a more accurate prediction of the normalized electrical feature. For the combined model of CNN#1+0.5D+RNN#1, using different types of images ends up with very similar performance, indicating the RNN model could process the temporal changes in image features extracted by CNN and achieve similar results.

7.4.4 Model Performance with the Hyper Image and the Enhanced S/N Image

The kernel in CNN models could learn through the depth of images which is different channels of images, without increasing the number of parameters in the model structure. Therefore, for CNN models, we added the additional types of images in two ways to investigate whether other image characterizations could help the prediction: the enhanced S/N EL image, which is a weighted average taking the three kinds of EL images, and the hyper image, which puts the baseline subtraction $EL@0.25I_o$ or $PL@OC$ as one more channel in the input images. As shown in Fig. 7.9, incorporating other image characterizations besides $EL@I_o$ images as part of the input increases the testing RMSE, and the testing RMSE is smaller for the case utilizing the enhanced S/N EL images than the case using hyper images. Moreover, the two cases using different hyper images perform similarly. The $EL@I_o$ image has the largest weight factor in the enhanced S/N EL image. Therefore, both results suggest that additional image characterizations except $EL@I_o$ do not help predict the electrical features' change while providing a more comprehensive evaluation of solar cells. The reason that other image characterizations are not that helpful could be due to that the electrical status of measuring the $EL@I_o$ images is closest to that of measuring the current-voltage curves to extract P_{mp} and R_s.

Using hyper images as the input significantly increases the number of parameters in RNN models, so the enhanced S/N EL images were used to investigate the influence of adding additional image characterizations on model performance without changing the number of parameters in the model. For RNN#1 and CNN#1+0.5D+RNN#1, the additional characterizations other than $EL@I_o$ do not influence the model performance. In Fig. 7.12, the testing RMSE using the raw $EL@I_o$ images is basically the same as using the enhanced S/N EL images for RNN#1 and CNN#1+0.5D+RNN#1.

7.4.5 Quantitative Performance of RNN with Raw Images for Predicting Electrical Performance

More complex image processing steps and model parameters require more computational resources and time to obtain predicted results. Based on results shown in Fig. 7.12, RNN#1 using the raw $EL@I_o$ and enhanced S/N EL images as the input has the lowest testing RMSE with the least number of modeling parameters. Therefore, RNN#1 using the raw $EL@I_o$ images is proposed as the best combination to accurately predict the normalized electrical features as ${}^nP_{mp,IV}$ and ${}^nR_{s,IV}$, which are chosen as the overall evaluation index and the degradation mechanism feature, respectively. Compared to the baseline model, the testing RMSE decreases from 0.0958 to 0.0593, realizing a reduction of 38.1%. Using original resolution images with a dimension of 1485×1485 as the input increases the number of model parameters by 44 times, while the testing RMSE is unchanged, as shown in case 53 in Table 7.2. Therefore, our proposed model has good stability against different image resolutions.

7.5 Conclusions

This study explores neural network models to predict the normalized power and series resistance based on EL and PL images for PV modules under accelerated exposures. The performance of different model variants in the categories of CNN, RNN, and CNN+RNN was compared. The Influences of scaling the output features and using different types of images as the input on the model performance were investigated. The early overfitting problem can be solved by adding batch normalization with large batch sizes. Scaling the output features can speed up the convergence of the validating MSE for training CNN models with batch normalization using large batch sizes. However, both modifications do not improve the model performance when extending the training epochs by five times. The baseline subtraction $EL@I_o$ image brings the lowest testing RMSE for the CNN model, and the raw $EL@I_o$ image and the enhanced S/N EL image bring the lowest testing RMSE for the RNN model. Incorporating other image characterizations into the input, such as using the enhanced S/N EL image or the hyper image, harms CNN models' performance but does not influence the performance of RNN and CNN+RNN models. The lowest testing RMSE for all CNN model variants is 0.0730, and for all RNN model variants is 0.0593. Compared to the performance of the baseline model, the testing RMSE is reduced by 23.8% for CNN models and 38.1% for RNN models at most. Combining the RNN model with one GRU layer, which has the output dimension specified as two, and the raw $EL@I_o$ images as the input is proposed as the best combination to predict the normalized electrical features, and the model is found to have good stability against different image resolutions. The finding of a significant performance improvement of RNN over CNN indicates that it is beneficial to take advantage of measurements for the same sample taken at different exposure times to make a more accurate prediction.

8 Conclusion

Commercial PV modules are usually made of several layers such as glass, encapsulant, solar cells, and backsheet, and the degradation is determined by their interaction with the exposed environment as a system. The properties and combinations of these packaging materials influence the ability to protect internal solar cells during long time operation[11] and the degradation rate, which is vital to lower the levelized cost of electricity[31]. In this study, degradation behaviors of sixteen module variants available in the PV market with considerable market share were compared under different exposure conditions with statistical analysis. Four-cell minimodules with five junction boxes installed to allow electrical measurements on each solar cell are used as study objects, and a total of 192 minimodules were fabricated. These sixteen module variants differed in encapsulant materials (EVA and POE), rear encapsulant types (transparent, UV-Cutoff, and opaque), module architectures (GB and DG), and cell types (monofacial and bifacial). Some modules were exposed under indoor accelerated exposures, including modified damp heat (80 $^{\circ}C$, and 85% RH) and modified damp heat with full-spectrum light (mDH+FSL), with a total exposure time of 2,520 hours, evenly divided into five steps for multiple stepwise characterizations. The remaining modules were installed in an outdoor testing site in the Dfa climate zone. Timeseries current-voltage curves, module temperature, and weather data recorded over the time period of 1.6 years were analyzed in this study. The timeseries data were processed by the $ddiv$[49] and $SunsVoc$[54] R packages to obtain the predicted electrical features and four power loss factors at reference conditions.

By comparing the confidence intervals (CIs) of various electrical features across different module variants, for both accelerated exposures and both brands, two DG module variants with the UV-Cutoff rear encapsulant and monofacial cells, are found to have the least average power loss of less than 5%. Two GB+EVA module variants with the opaque rear encapsulant, are found to have a significantly greater average power loss. From the comparison of the percent change in different electrical features, their correlation to power, and the principal component analysis results, the power loss is identified to be mainly affected by the increased series resistance (R_s). Considering the exposure conditions, the R_s increase is associated with interconnection corrosion. Unsupervised hierarchical clustering results show that clusters have a dependency on module architecture for both brands. As for the results of outdoor exposure, although some module variants are influenced by the electrical connection issues leading to significant differences between the two modules of the same variant, significant differences are identified between three module variants and the other two module variants. The dominant reason contributing to the power loss is identified by the lowest normalized power loss factor and identified to be uniform current power loss (${}^{n}\Delta P_{Isc}$), followed by power loss due to R_s (${}^{n}\Delta P_{Rs}$) for most module variants. However, the four package combinations, namely EVA+GB, EVA+DG, POE+GB, and POE+DG do not exhibit significant differences in normalized power and any normalized power loss factors for the last three months of outdoor exposure. It is worth noting that the change in features is not entirely caused by degradation due to the technical difficulty of removing seasonality and noise caused by the relatively short exposure time.

Nevertheless, the normalized electrical features were modeled over time for each module variant under indoor accelerated and outdoor exposures to illustrate how the developed cross-correlation algorithm works and the interpretation of the results. The developed algorithm can quantify the similarity of module degradation behaviors between indoor accelerated and outdoor exposures, considering both the degradation rates and trends over time. First, it scales the exposure time in the indoor model for ${}^{n}P_{mp,IV}$ and adjusts it to be closest to the outdoor model for ${}^{n}P_{mp,IV}$ in their overlapping exposure time and returns the scale factor as $CCSF^*$. The $CCSF^*$ is then applied to scale all indoor models, and a cross-correlation coefficient (CCC) is calculated for each feature to quantify the similarity in trends. For comparing each accelerated exposure and outdoor exposure, ten out of sixteen module variants do not have a $CCSF^*$ on the guessing range boundaries with an average of around 0.5, indicating that our indoor accelerated exposures lead to about two times faster power drop than the outdoor exposure in the overlapping time range. In addition, the $CCCs$ for ${}^{n}P_{mp,IV}$ and ${}^{n}R_{s,IV}$ are very high. However, due to the missing activated degradation mechanism indicated by a much smaller change in ${}^{n}I_{sc,IV}$ in accelerated exposures compared to the outdoor exposure, it can not be concluded that the degradation behaviors are similar under both exposures. In order to confirm the results of comparing module degradation behaviors between exposures, extending outdoor exposure is necessary because the seasonality heavily influences the outdoor models, as indicated by frequent occurrence of choosing the change-point model as the best model.

The extensive measurements of I-V, EL, and PL for samples at different exposure times provide the opportunity to use neural network models to predict the change in electrical parameters through image characterizations. Three primary neural network model categories using different image pre-processing were investigated in this study, which are CNN, RNN, and CNN+RNN. There are three main types of image input: the raw EL image, the baseline subtraction EL image, and the enhanced S/N EL image constructed by the three EL images with different injected currents. Considering the model performance and complexity of image processing, a combination of an RNN model and raw EL images as the input is proposed as the best solution. While stepwise characterizations are widely used for modules under indoor accelerated exposure, this temporal relationship is often not explored for neural network models. The finding of a significant performance improvement of RNN over CNN indicates that it is beneficial to take advantage of measurements for the same sample taken at different exposure times to make a more accurate prediction.

Appendix A

Preparation of this document

This document was prepared using pdfLaTeX and other open source tools. The (free) programs implemented are as follows:

- LaTeX implementation:

  MiKTeX http://www.miktex.org/

  TeXLive https://www.tug.org/texlive/

- TeX-oriented editing environments:

  TexStudio https://www.texstudio.org/

- Bibliographical:

  BibTeX http://www.bibtex.org/

  Biber http://biblatex-biber.sourceforge.net/

  Zotero https://www.zotero.org/

  Better BibTeX For Zotero https://retorque.re/zotero-better-bibtex/

Complete Bibliography

[1] Walburga Hemetsberger, Micheal SchMela, and Gianni Chianetta, "Global Market Outlook 2021-2025 – SolarPower Europe," Solar Power Europe, Tech. Rep., Jul. 2021.

[2] A. P. Patel, A. Sinha, and G. Tamizhmani, "Field-Aged Glass/Backsheet and Glass/Glass PV Modules: Encapsulant Degradation Comparison," *IEEE Journal of Photovoltaics*, vol. 10, no. 2, pp. 607–615, Mar. 2020, ISSN: 2156-3403. DOI: 10.1109/JPHOTOV.2019.2958516.

[3] W. Gu, T. Ma, S. Ahmed, Y. Zhang, and J. Peng, "A comprehensive review and outlook of bifacial photovoltaic (bPV) technology," *Energy Conversion and Management*, vol. 223, p. 113 283, Nov. 2020, ISSN: 0196-8904. DOI: 10.1016/j.enconman.2020.113283.

[4] T. C. Felder, W. Gambogi, H. Hu, T. J. Trout, L. Garreau-Iles, S. MacMaster, and K. R. Choudhury, "Analysis of glass-glass modules," in *New Concepts in Solar and Thermal Radiation Conversion and Reliability*, J. N. Munday, P. Bermel, and M. D. Kempe, Eds., San Diego, United States: SPIE, Sep. 2018, p. 1. DOI: 10.1117/12.2321637.

[5] B. M. Habersberger and P. Hacke, "Impact of illumination and encapsulant resistivity on polarization-type potential-induced degradation on n-PERT cells," *Progress in Photovoltaics: Research and Applications*, vol. n/a, no. n/a, Oct. 2021, ISSN: 1099-159X. DOI: 10.1002/pip.3505.

[6] A. Skoczek, T. Sample, and E. D. Dunlop, "The results of performance measurements of field-aged crystalline silicon photovoltaic modules," *Progress in Photovoltaics: Research and Applications*, vol. 17, no. 4, pp. 227–240, 2009, ISSN: 1099-159X. DOI: 10.1002/pip.874.

[7] M. C. C. de Oliveira, A. S. A. Diniz Cardoso, M. M. Viana, and V. d. F. C. Lins, "The causes and effects of degradation of encapsulant ethylene vinyl acetate copolymer (EVA) in crystalline silicon photovoltaic modules: A review," *Renewable and Sustainable Energy Reviews*, vol. 81, pp. 2299–2317, Jan. 2018, ISSN: 1364-0321. DOI: 10.1016/j.rser.2017.06.039.

[8] J. Liu, M. Wang, A. J. Curran, E. Schnabel, M. Köhl, J. L. Braid, and R. H. French, "Degradation mechanisms and partial shading of glass-backsheet and double-glass photovoltaic modules in three climate zones determined by remote monitoring of time-series current–voltage and power datastreams," *Solar Energy*, vol. 224, pp. 1291–1301, Aug. 2021, ISSN: 0038-092X. DOI: 10.1016/j.solener.2021.06.022.

[9] M. C. C. de Oliveira, D. A. Cassini, A. Diniz, L. G. Soares, M. Viana, L. Kazmerski, and V. Lins, "Comparison and analysis of performance and degradation differences of crystalline-Si photovoltaic modules after 15-years of field operation," *Solar Energy*, 2019. DOI: 10.1016/j.solener.2019.08.051.

[10] M. Kempe, "Encapsulant Materials for PV Modules," in *Photovoltaic Solar Energy*, John Wiley & Sons, Ltd, 2016, ch. 10.2, pp. 478–490, ISBN: 978-1-118-92749-6. DOI: 10.1002/9781118927496.ch43.

[11] A. Omazic, G. Oreski, M. Halwachs, G. C. Eder, C. Hirschl, L. Neumaier, G. Pinter, and M. Erceg, "Relation between degradation of polymeric components in

crystalline silicon PV module and climatic conditions: A literature review," *Solar Energy Materials and Solar Cells*, vol. 192, pp. 123–133, Apr. 2019, ISSN: 0927-0248. DOI: 10.1016/j.solmat.2018.12.027.

[12] M. D. Kempe, G. J. Jorgensen, K. M. Terwilliger, T. J. McMahon, C. E. Kennedy, and T. T. Borek, "Acetic acid production and glass transition concerns with ethylene-vinyl acetate used in photovoltaic devices," *Solar Energy Materials and Solar Cells*, vol. 91, no. 4, pp. 315–329, Feb. 2007, ISSN: 0927-0248. DOI: 10.1016/j.solmat.2006.10.009.

[13] D. C. Miller, F. Alharbi, A. Andreas, J. G. Bokria, D. M. Burns, J. Bushong, X. Chen, D. Dietz, S. Fowler, X. Gu, A. Habte, C. C. Honeker, M. D. Kempe, H. Khonkar, M. Köhl, N. H. Phillips, J. Rivera, K. P. Scott, A. Singh, and A. F. Zielnik, "Degradation in photovoltaic encapsulation strength of attachment: Results of the first PVQAT TG5 artificial weathering study," *Progress in Photovoltaics: Research and Applications*, vol. 28, no. 7, pp. 639–658, 2020, ISSN: 1099-159X. DOI: 10.1002/pip.3255.

[14] B. K. Sharma, U. Desai, A. Singh, and A. Singh, "Effect of vinyl acetate content on the photovoltaic-encapsulation performance of ethylene vinyl acetate under accelerated ultra-violet aging," *Journal of Applied Polymer Science*, vol. 137, no. 2, p. 48 268, 2020, ISSN: 1097-4628. DOI: 10.1002/app.48268.

[15] Q. Wang, "Research on the effect of encapsulation material on anti-PID performance of 1500,V solar module," *Optik*, vol. 202, p. 163 540, Feb. 2020, ISSN: 0030-4026. DOI: 10.1016/j.ijleo.2019.163540.

[16] K. Sporleder, J. Bauer, S. Großer, S. Richter, A. Hähnel, M. Turek, V. Naumann, K. K. Ilse, and C. Hagendorf, "Potential-Induced Degradation of Bifacial PERC Solar Cells Under Illumination," *IEEE Journal of Photovoltaics*, vol. 9, no. 6, pp. 1522–1525, Nov. 2019, ISSN: 2156-3403. DOI: 10.1109/JPHOTOV.2019.2937231.

[17] V. Naumann, D. Lausch, A. Hähnel, J. Bauer, O. Breitenstein, A. Graff, M. Werner, S. Swatek, S. Großer, J. Bagdahn, and C. Hagendorf, "Explanation of potential-induced degradation of the shunting type by Na decoration of stacking faults in Si solar cells," *Solar Energy Materials and Solar Cells*, vol. 120, pp. 383–389, Jan. 2014, ISSN: 0927-0248. DOI: 10.1016/j.solmat.2013.06.015.

[18] D. B. Sulas-Kern, M. Owen-Bellini, P. Ndione, L. Spinella, A. Sinha, S. Uličná, S. Johnston, and L. T. Schelhas, "Electrochemical degradation modes in bifacial silicon photovoltaic modules," *Progress in Photovoltaics: Research and Applications*, vol. n/a, no. n/a, Dec. 2021, ISSN: 1099-159X. DOI: 10.1002/pip.3530.

[19] B. Lin, C. Zheng, Q. Zhu, and F. Xie, "A polyolefin encapsulant material designed for photovoltaic modules: From perspectives of peel strength and transmittance," *Journal of Thermal Analysis and Calorimetry*, vol. 140, no. 5, pp. 2259–2265, Jun. 2020, ISSN: 1588-2926. DOI: 10.1007/s10973-019-09006-w.

[20] G. Oreski, A. Omazic, G. C. Eder, Y. Voronko, L. Neumaier, W. Mühleisen, C. Hirschl, G. Ujvari, R. Ebner, and M. Edler, "Properties and degradation behaviour of polyolefin encapsulants for photovoltaic modules," *Progress in Photovoltaics: Research and Applications*, vol. 28, no. 12, pp. 1277–1288, 2020, ISSN: 1099-159X. DOI: 10.1002/pip.3323.

[21] C. Barretta, G. Oreski, S. Feldbacher, K. Resch-Fauster, and R. Pantani, "Comparison of Degradation Behavior of Newly Developed Encapsulation Materials

for Photovoltaic Applications under Different Artificial Ageing Tests," *Polymers*, vol. 13, no. 2, p. 271, Jan. 2021, ISSN: 2073-4360. DOI: 10.3390/polym13020271.

[22] A. Sinha, D. B. Sulas-Kern, M. Owen-Bellini, L. Spinella, S. Uličná, S. A. Pelaez, S. Johnston, and L. T. Schelhas, "Glass/glass photovoltaic module reliability and degradation: A review," *Journal of Physics D: Applied Physics*, vol. 54, no. 41, p. 413 002, Aug. 2021, ISSN: 0022-3727. DOI: 10.1088/1361-6463/ac1462.

[23] J. Tang, C. Ju, R. Lv, X. Zeng, J. Chen, D. Fu, J.-N. Jaubert, and T. Xu, "The Performance of Double Glass Photovoltaic Modules under Composite Test Conditions," *Energy Procedia*, Proceedings of the SNEC 11th International Photovoltaic Power Generation Conference & Exhibition, SNEC 2017 Scientific Conference, vol. 130, pp. 87–93, Sep. 2017, ISSN: 1876-6102. DOI: 10.1016/j.egypro.2017.09.400.

[24] R. E. Kumar, G. Von Gastrow, N. Theut, A. M. Jeffries, T. Sidawi, A. Ha, F. DePlachett, H. Moctezuma-Andraca, S. Donaldson, M. I. Bertoni, and D. P. Fenning, "Glass vs. Backsheet: Deconvoluting the Role of Moisture in Power Loss in Silicon Photovoltaics With Correlated Imaging During Accelerated Testing," *IEEE Journal of Photovoltaics*, vol. 12, no. 1, pp. 285–292, Jan. 2022, ISSN: 2156-3403. DOI: 10.1109/JPHOTOV.2021.3122878.

[25] Y. Zhang, J. Xu, J. Mao, J. Tao, H. Shen, Y. Chen, Z. Feng, P. J. Verlinden, P. Yang, and J. Chu, "Long-term reliability of silicon wafer-based traditional backsheet modules and double glass modules," *RSC Advances*, vol. 5, no. 81, pp. 65 768–65 774, Jul. 2015, ISSN: 2046-2069. DOI: 10.1039/C5RA11224A.

[26] S. Smith, L. Perry, S. Watson, S. L. Moffitt, S.-J. Shen, S. Mitterhofer, L.-P. Sung, D. Jacobs, and X. Gu, "Transparent backsheets for bifacial photovoltaic (PV) modules: Material characterization and accelerated laboratory testing," *Progress in*

Photovoltaics: Research and Applications, vol. 1, no. 11, Oct. 2021, ISSN: 1099-159X. DOI: 10.1002/pip.3494.

[27] W. Gambogi, M. Demko, B.-L. Yu, S. Kurian, S. MacMaster, K. R. Choudhury, J. Tracy, D. Hu, and H. Hu, "Transparent Backsheets for Bifacial Photovoltaic Modules," in *2020 47th IEEE Photovoltaic Specialists Conference (PVSC)*, Jun. 2020, pp. 1651–1657. DOI: 10.1109/PVSC45281.2020.9300924.

[28] Jinko Solar, "Transparent Backsheet VS Dual Glass—Advantages and Disadvantages," Jinko Solar, White Paper, Dec. 2020.

[29] H. Han, H. Yan, X. Wang, K. Zhang, J. Huang, Y. Sun, J. Liu, P. J. Verlinden, P. Altermatt, Z. Liang, and H. Shen, "Analysis of the degradation of encapsulant materials used in photovoltaic modules exposed to different climates in China," *Solar Energy*, vol. 194, pp. 177–188, Dec. 2019, ISSN: 0038-092X. DOI: 10.1016/j.solener.2019.10.014.

[30] S. Lindig, A. Louwen, D. Moser, and M. Topic, "Outdoor PV System Monitoring—Input Data Quality, Data Imputation and Filtering Approaches," *Energies*, vol. 13, no. 19, p. 5099, Jan. 2020, ISSN: 1996-1073. DOI: 10.3390/en13195099.

[31] M. Theristis, A. Livera, C. B. Jones, G. Makrides, G. E. Georghiou, and J. S. Stein, "Nonlinear Photovoltaic Degradation Rates: Modeling and Comparison Against Conventional Methods," *IEEE Journal of Photovoltaics*, vol. 10, no. 4, pp. 1112–1118, Jul. 2020, ISSN: 2156-3403. DOI: 10.1109/JPHOTOV.2020.2992432.

[32] S. Lindig, I. Kaaya, K.-A. Weiss, D. Moser, and M. Topic, "Review of Statistical and Analytical Degradation Models for Photovoltaic Modules and Systems as Well as Related Improvements," *IEEE Journal of Photovoltaics*, vol. 8, no. 6, pp. 1773–1786, Nov. 2018, ISSN: 2156-3403. DOI: 10.1109/JPHOTOV.2018.2870532.

[33] A. Frick, G. Makrides, M. Schubert, M. Schlecht, and G. E. Georghiou, "Degradation Rate Location Dependency of Photovoltaic Systems," *Energies*, vol. 13, no. 24, p. 6751, Jan. 2020, ISSN: 1996-1073. DOI: 10.3390/en13246751.

[34] K. Kunaifi, A. Reinders, S. Lindig, M. Jaeger, and D. Moser, "Operational Performance and Degradation of PV Systems Consisting of Six Technologies in Three Climates," *Applied Sciences*, vol. 10, no. 16, p. 5412, Jan. 2020, ISSN: 2076-3417. DOI: 10.3390/app10165412.

[35] Roger H. French, Laura S. Bruckman, David Moser, Sascha Lindig, Mike van Iseghem, Björn Müller, Joshua S. Stein, Mauricio Richter, Magnus Herz, Wilfried Van Sark, and Franz Baumgartner, "Assessment of Performance Loss Rate of PV Power Systems," International Energy Agency, Tech. Rep., Apr. 2021.

[36] A. Kyprianou, A. Phinikarides, G. Makrides, and G. E. Georghiou, "Definition and Computation of the Degradation Rates of Photovoltaic Systems of Different Technologies With Robust Principal Component Analysis," *IEEE Journal of Photovoltaics*, vol. 5, no. 6, pp. 1698–1705, Nov. 2015, ISSN: 2156-3403. DOI: 10.1109/JPHOTOV.2015.2478065.

[37] I. Romero-Fiances, A. Livera, M. Theristis, G. Makrides, J. S. Stein, G. Nofuentes, J. de la Casa, and G. E. Georghiou, "Impact of duration and missing data on the long-term photovoltaic degradation rate estimation," *Renewable Energy*, vol. 181, pp. 738–748, Jan. 2022, ISSN: 0960-1481. DOI: 10.1016/j.renene.2021.09.078.

[38] D. C. Jordan, C. Deline, S. R. Kurtz, G. M. Kimball, and M. Anderson, "Robust PV Degradation Methodology and Application," *IEEE Journal of Photovoltaics*, vol. 8, no. 2, pp. 525–531, Mar. 2018, ISSN: 2156-3403. DOI: 10.1109/JPHOTOV.2017.2779779.

[39] D. C. Jordan, M. G. Deceglie, and S. R. Kurtz, “PV degradation methodology comparison — A basis for a standard,” in *2016 IEEE 43rd Photovoltaic Specialists Conference (PVSC)*, Jun. 2016, pp. 0273–0278. DOI: 10.1109/PVSC.2016.7749593.

[40] D. C. Jordan, T. J. Silverman, B. Sekulic, and S. R. Kurtz, “PV degradation curves: Non-linearities and failure modes,” *Progress in Photovoltaics: Research and Applications*, vol. 25, no. 7, pp. 583–591, 2017, ISSN: 1099-159X. DOI: 10.1002/pip.2835.

[41] I. Kaaya, J. Ascencio-Vásquez, K.-A. Weiss, and M. Topič, “Assessment of uncertainties and variations in PV modules degradation rates and lifetime predictions using physical models,” *Solar Energy*, vol. 218, pp. 354–367, Apr. 2021, ISSN: 0038-092X. DOI: 10.1016/j.solener.2021.01.071.

[42] I. Kaaya and K.-A. Weiss, “Physical and Data-driven Hybrid Model for Outdoor Lifetime Prediction of PV Modules,” in *2020 47th IEEE Photovoltaic Specialists Conference (PVSC)*, Jun. 2020, pp. 0460–0464. DOI: 10.1109/PVSC45281.2020.9300526.

[43] D. A. Quansah and M. S. Adaramola, “Assessment of early degradation and performance loss in five co-located solar photovoltaic module technologies installed in Ghana using performance ratio time-series regression,” *Renewable Energy*, vol. 131, pp. 900–910, Feb. 2019, ISSN: 0960-1481. DOI: 10.1016/j.renene.2018.07.117.

[44] I. Kaaya, S. Lindig, K.-A. Weiss, A. Virtuani, M. Sidrach de Cardona Ortin, and D. Moser, “Photovoltaic lifetime forecast model based on degradation patterns,” *Progress in Photovoltaics: Research and Applications*, vol. 28, no. 10, pp. 979–992, 2020, ISSN: 1099-159X. DOI: 10.1002/pip.3280.

[45] A. Livera, M. Theristis, E. Koumpli, S. Theocharides, G. Makrides, J. Sutterlueti, J. S. Stein, and G. E. Georghiou, "Data processing and quality verification for improved photovoltaic performance and reliability analytics," *Progress in Photovoltaics: Research and Applications*, vol. 29, no. 2, pp. 143–158, 2021, ISSN: 1099-159X. DOI: 10.1002/pip.3349.

[46] A. Gok, E. Ozkalay, G. Friesen, and F. Frontini, "Power Loss Modes of Building-Integrated Photovoltaic Modules: An Analytical Approach Using Outdoor $I-V$ Curves," *IEEE Journal of Photovoltaics*, vol. 11, no. 3, pp. 789–796, May 2021, ISSN: 2156-3403. DOI: 10.1109/JPHOTOV.2021.3060719.

[47] X. Sun, R. V. K. Chavali, and M. A. Alam, "Real-time monitoring and diagnosis of photovoltaic system degradation only using maximum power point—the Suns-Vmp method," *Progress in Photovoltaics: Research and Applications*, vol. 27, no. 1, pp. 55–66, 2019, ISSN: 1099-159X. DOI: 10.1002/pip.3043.

[48] M. B. H. Rhouma, A. Gastli, L. Ben Brahim, F. Touati, and M. Benammar, "A simple method for extracting the parameters of the PV cell single-diode model," *Renewable Energy*, vol. 113, pp. 885–894, Dec. 2017, ISSN: 0960-1481. DOI: 10.1016/j.renene.2017.06.064.

[49] W.-H. Huang, Xuan Ma, Jiqi Liu, Menghong Wang, Alan J. Curran, J. S. Fada, Jean-Nicolas Jaubert, Jing Sun, Jennifer L. Braid, Jenny Brynjarsdottir, and Roger H. French, *Ddiv: Data Driven I-v Feature Extraction*, Comprehensive R Archive Network (CRAN), Apr. 2021.

[50] X. Ma, W.-H. Huang, E. Schnabel, M. Köhl, J. Brynjarsdóttir, J. L. Braid, and R. H. French, "Data-Driven \$I\$–\$V\$ Feature Extraction for Photovoltaic Modules," *IEEE Journal of Photovoltaics*, vol. 9, no. 5, pp. 1405–1412, Sep. 2019, ISSN: 2156-3403. DOI: 10.1109/JPHOTOV.2019.2928477.

[51] M. Wang, J. Liu, T. J. Burleyson, E. J. Schneller, K. O. Davis, R. H. French, and J. L. Braid, "Analytic \$I_\textsc\$–\$V_\textoc\$ Method and Power Loss Modes From Outdoor Time-Series \$I\$–\$V\$ Curves," *IEEE Journal of Photovoltaics*, vol. 10, no. 5, pp. 1379–1388, Sep. 2020, ISSN: 2156-3403. DOI: 10.1109/JPHOTOV.2020.2993100.

[52] A. C. Killam, J. F. Karas, A. Augusto, and S. G. Bowden, "Monitoring of Photovoltaic System Performance Using Outdoor Suns-VOC," *Joule*, vol. 5, no. 1, pp. 210–227, Jan. 2021, ISSN: 2542-4351. DOI: 10.1016/j.joule.2020.11.007.

[53] S. Guo, E. Schneller, J. Walters, K. O. Davis, and W. V. Schoenfeld, "Detecting loss mechanisms of c-Si PV modules in-situ *I-V* measurement," in *SPIE Optics + Photonics for Sustainable Energy*, N. G. Dhere, J. H. Wohlgemuth, and K. Sakurai, Eds., San Diego, California, United States, Sep. 2016, 99380N. DOI: 10.1117/12.2236939.

[54] M. Wang, Tyler J. Burleyson, Jiqi Liu, Alan J. Curran, Abdulkerim Gok, Eric J. Schneller, Kristopher O. Davis, Jennifer L. Braid, and Roger H. French, *SunsVoc: Constructing Suns-Voc from Outdoor Time-Series I-V Curves*, Comprehensive R Archive Network (CRAN), Apr. 2021.

[55] V. S. B. Kurukuru, F. Blaabjerg, M. A. Khan, and A. Haque, "A Novel Fault Classification Approach for Photovoltaic Systems," *Energies*, vol. 13, no. 2, p. 308, Jan. 2020, ISSN: 1996-1073. DOI: 10.3390/en13020308.

[56] T. Berghout, M. Benbouzid, X. Ma, S. Djurović, and L. Mouss, "Machine Learning for Photovoltaic Systems Condition Monitoring: A Review," in *IECON 2021 – 47th Annual Conference of the IEEE Industrial Electronics Society*, Oct. 2021, pp. 1–5. DOI: 10.1109/IECON48115.2021.9589423.

[57] J. Fan, S. Rao, G. Muniraju, C. Tepedelenlioglu, and A. Spanias, "Fault Classification in Photovoltaic Arrays Using Graph Signal Processing," in *2020 IEEE Conference on Industrial Cyberphysical Systems (ICPS)*, vol. 1, Jun. 2020, pp. 315–319. DOI: 10.1109/ICPS48405.2020.9274763.

[58] H. P.-C. Hwang, C. C.-Y. Ku, and J. C.-C. Chan, "Detection of Malfunctioning Photovoltaic Modules Based on Machine Learning Algorithms," *IEEE Access*, vol. 9, pp. 37 210–37 219, 2021, ISSN: 2169-3536. DOI: 10.1109/ACCESS.2021.3063461.

[59] R. Pierdicca, E. Malinverni, F. Piccinini, M. Paolanti, A. Felicetti, and P. Zingaretti, "DEEP CONVOLUTIONAL NEURAL NETWORK FOR AUTOMATIC DETECTION OF DAMAGED PHOTOVOLTAIC CELLS," *The International Archives of the Photogrammetry, Remote Sensing and Spatial Information Sciences*, 2018. DOI: 10.5194/ISPRS-ARCHIVES-XLII-2-893-2018.

[60] X. Li, Q. Yang, Z. Lou, and W. Yan, "Deep Learning Based Module Defect Analysis for Large-Scale Photovoltaic Farms," *IEEE Transactions on Energy Conversion*, vol. 34, no. 1, pp. 520–529, Mar. 2019, ISSN: 1558-0059. DOI: 10.1109/TEC.2018.2873358.

[61] M. U. Ali, H. F. Khan, M. Masud, K. D. Kallu, and A. Zafar, "A machine learning framework to identify the hotspot in photovoltaic module using infrared thermography," *Solar Energy*, vol. 208, pp. 643–651, Sep. 2020, ISSN: 0038-092X. DOI: 10.1016/j.solener.2020.08.027.

[62] V. S. B. Kurukuru, A. Haque, M. A. Khan, and A. K. Tripathy, "Fault classification for Photovoltaic Modules Using Thermography and Machine Learning Techniques," in *2019 International Conference on Computer and Information Sciences (ICCIS)*, Apr. 2019, pp. 1–6. DOI: 10.1109/ICCISci.2019.8716442.

[63] R. Fazai, K. Abodayeh, M. Mansouri, M. Trabelsi, H. Nounou, M. Nounou, and G. E. Georghiou, "Machine learning-based statistical testing hypothesis for fault detection in photovoltaic systems," *Solar Energy*, vol. 190, pp. 405–413, Sep. 2019, ISSN: 0038-092X. DOI: 10.1016/j.solener.2019.08.032.

[64] L. Maaløe, O. Winther, S. Spataru, and D. Sera, "Condition Monitoring in Photovoltaic Systems by Semi-Supervised Machine Learning," *Energies*, vol. 13, no. 3, p. 584, Jan. 2020, ISSN: 1996-1073. DOI: 10.3390/en13030584.

[65] A. I. Khalyasmaa, S. A. Eroshenko, V. A. Tashchilin, H. Ramachandran, T. Piepur Chakravarthi, and D. N. Butusov, "Industry Experience of Developing Day-Ahead Photovoltaic Plant Forecasting System Based on Machine Learning," *Remote Sensing*, vol. 12, no. 20, p. 3420, Jan. 2020, ISSN: 2072-4292. DOI: 10.3390/rs12203420.

[66] M. Aslam, J.-M. Lee, and S. Hong, "A multi-layer perceptron based deep learning model to quantify the energy potentials of a thin film a-Si PV system," *Energy Reports*, 2020 The 7th International Conference on Power and Energy Systems Engineering, vol. 6, pp. 1331–1336, Dec. 2020, ISSN: 2352-4847. DOI: 10.1016/j.egyr.2020.11.025.

[67] J. Vicente-Gabriel, A.-B. Gil-González, A. Luis-Reboredo, P. Chamoso, and J. M. Corchado, "LSTM Networks for Overcoming the Challenges Associated with Photovoltaic Module Maintenance in Smart Cities," *Electronics*, vol. 10, no. 1, p. 78, Jan. 2021, ISSN: 2079-9292. DOI: 10.3390/electronics10010078.

[68] A. Sherstinsky, "Fundamentals of Recurrent Neural Network (RNN) and Long Short-Term Memory (LSTM) Network," *Physica D: Nonlinear Phenomena*, vol. 404, p. 132 306, Mar. 2020, Comment: 43 pages, 10 figures, 78 references, ISSN: 01672789. DOI: 10.1016/j.physd.2019.132306. arXiv: 1808.03314.

[69] K. Cho, B. van Merrienboer, D. Bahdanau, and Y. Bengio, "On the Properties of Neural Machine Translation: Encoder-Decoder Approaches," *arXiv:1409.1259 [cs, stat]*, Oct. 2014, Comment: Eighth Workshop on Syntax, Semantics and Structure in Statistical Translation (SSST-8). arXiv: 1409.1259 [cs, stat].

[70] A. M. Karimi, Y. Wu, M. Koyuturk, and R. H. French, "Spatiotemporal Graph Neural Network for Performance Prediction of Photovoltaic Power Systems," *Proceedings of the AAAI Conference on Artificial Intelligence*, vol. 35, no. 17, pp. 15 323–15 330, May 2021, ISSN: 2374-3468.

[71] Rawad Al-Mashhadani, Gamal Alkawsi, Yahia Baashar, Ammar Ahmed Alkahtani, Farah Hani Nordin, Wahidah Hashim, and Tiong Sieh Kiong, "Deep Learning Methods for Solar Fault Detection and Classification: A Review," *Information Sciences Letters*, vol. 10, no. 2, pp. 323–331, May 2021, ISSN: 20909551, 2090956X. DOI: 10.18576/isl/100213.

[72] W. Tang, Q. Yang, K. Xiong, and W. Yan, "Deep learning based automatic defect identification of photovoltaic module using electroluminescence images," *Solar Energy*, vol. 201, pp. 453–460, May 2020, ISSN: 0038-092X. DOI: 10.1016/j.solener.2020.03.049.

[73] A. M. Karimi, J. S. Fada, M. A. Hossain, S. Yang, T. J. Peshek, J. L. Braid, and R. H. French, "Automated Pipeline for Photovoltaic Module Electroluminescence Image Processing and Degradation Feature Classification," *IEEE Journal of Photovoltaics*, vol. 9, no. 5, pp. 1324–1335, Sep. 2019, ISSN: 2156-3403. DOI: 10.1109/JPHOTOV.2019.2920732.

[74] A. Bartler, L. Mauch, B. Yang, M. Reuter, and L. Stoicescu, "Automated Detection of Solar Cell Defects with Deep Learning," in *2018 26th European Signal Processing Conference (EUSIPCO)*, Sep. 2018, pp. 2035–2039. DOI: 10.23919/EUSIPCO.2018.8553025.

[75] S. Deitsch, V. Christlein, S. Berger, C. Buerhop-Lutz, A. Maier, F. Gallwitz, and C. Riess, "Automatic Classification of Defective Photovoltaic Module Cells in Electroluminescence Images," *Solar Energy*, vol. 185, pp. 455–468, Jun. 2019, ISSN: 0038092X. DOI: 10.1016/j.solener.2019.02.067. arXiv: 1807.02894.

[76] B. G. Pierce, A. M. Karimi, J. Liu, R. H. French, and J. L. Braid, "Identifying Degradation Modes of Photovoltaic Modules Using Unsupervised Machine Learning on Electroluminescense Images," in *2020 47th IEEE Photovoltaic Specialists Conference (PVSC)*, Jun. 2020, pp. 1850–1855. DOI: 10.1109/PVSC45281.2020.9301021.

[77] A. M. Karimi, J. S. Fada, N. A. Parrilla, B. G. Pierce, M. Koyutürk, R. H. French, and J. L. Braid, "Generalized and Mechanistic PV Module Performance Prediction

From Computer Vision and Machine Learning on Electroluminescence Images," *IEEE Journal of Photovoltaics*, vol. 10, no. 3, pp. 878–887, May 2020, ISSN: 2156-3403. DOI: 10.1109/JPHOTOV.2020.2973448.

[78] D. Wisniewski, R. Lv, S. V. Nair, J.-N. Jaubert, T. Xu, and H. E. Ruda, "Measurement and modelling of water ingress into double-glass photovoltaic modules," *Progress in Photovoltaics: Research and Applications*, vol. 27, no. 2, pp. 144–151, 2019, ISSN: 1099-159X. DOI: 10.1002/pip.3069.

[79] V. Bheemreddy, J. J. Bill Liu, A. Wills, and C. P. Murcia, "Life Prediction Model Development for Flexible Photovoltaic Modules using Accelerated Damp Heat Testing," in *2018 IEEE 7th World Conference on Photovoltaic Energy Conversion (WCPEC) (A Joint Conference of 45th IEEE PVSC, 28th PVSEC 34th EU PVSEC)*, Jun. 2018, pp. 1249–1251. DOI: 10.1109/PVSC.2018.8547610.

[80] I. Kaaya, M. Koehl, A. P. Mehilli, S. de Cardona Mariano, and K. A. Weiss, "Modeling Outdoor Service Lifetime Prediction of PV Modules: Effects of Combined Climatic Stressors on PV Module Power Degradation," *IEEE Journal of Photovoltaics*, vol. 9, no. 4, pp. 1105–1112, Jul. 2019, ISSN: 2156-3403. DOI: 10.1109/JPHOTOV.2019.2916197.

[81] X. Gu, Y. Pang, C.-C. Lin, K. Liu, T. Nguyen, and J. W. Chin, "Linking accelerated laboratory and outdoor exposure results for PV polymeric materials: A mechanistic study of EVA," in *SPIE Solar Energy + Technology*, N. G. Dhere, J. H. Wohlgemuth, and K. W. Lynn, Eds., San Diego, California, United States, Sep. 2013, p. 88250L. DOI: 10.1117/12.2024532.

[82] F. Kersten, F. Fertig, K. Petter, B. Klöter, E. Herzog, M. B. Strobel, J. Heitmann, and J. W. Müller, "System performance loss due to LeTID," *Energy Procedia*, 7th

International Conference on Silicon Photovoltaics, SiliconPV 2017, 3-5 April 2017, Freiburg, Germany, vol. 124, pp. 540–546, Sep. 2017, ISSN: 1876-6102. DOI: 10.1016/j.egypro.2017.09.260.

[83] P. Hacke, R. Smith, K. Terwilliger, S. Glick, D. Jordan, S. Johnston, M. Kempe, and S. Kurtz, "Acceleration factor determination for potential-induced degradation in crystalline silicon PV modules," in *2013 IEEE International Reliability Physics Symposium (IRPS)*, Apr. 2013, 4B.1.1–4B.1.5. DOI: 10.1109/IRPS.2013.6532009.

[84] J. Liu, A. J. Curran, J. S. Fada, X. Ma, W.-H. Huang, C. B. Jones, E. Schnabel, M. Kohl, J. L. Braid, and R. H. French, "Cross-correlation Analysis of the Indoor Accelerated and Real World Exposed Photovoltaic Systems Across Multiple Climate Zones," in *2018 IEEE 7th World Conference on Photovoltaic Energy Conversion (WCPEC) (A Joint Conference of 45th IEEE PVSC, 28th PVSEC 34th EU PVSEC)*, Jun. 2018, pp. 3949–3954. DOI: 10.1109/PVSC.2018.8547840.

[85] M. Owen-Bellini, P. Hacke, D. C. Miller, M. D. Kempe, S. Spataru, T. Tanahashi, S. Mitterhofer, M. Jankovec, and M. Topič, "Advancing reliability assessments of photovoltaic modules and materials using combined-accelerated stress testing," *Progress in Photovoltaics: Research and Applications*, vol. 29, no. 1, pp. 64–82, 2021, ISSN: 1099-159X. DOI: 10.1002/pip.3342.

[86] R. A. Sinton and A. Cuevas, "A Quasi-Steady-State Open-Circuit Voltage Method for Solar Cell Characterization," in *Proceedings of the 16th European Photovoltaic Solar Energy Conference*, vol. 1152, 2000.

[87] Greg Horner, *PixEL: Versatile Electroluminescence and Photoluminescence System*, May 2022. [Online]. Available: http://tauscience.com/pixel (visited on 05/30/2022).

[88] Jennifer L. Braid, Ahmad Maroof Karimi, Benjamin G. Pierce, Justin S. Fada, Nicholas A. Parrilla, and Roger H. French, *Pvimage: Package for pv image analysis and machine learning modeling*, May 2020.

[89] S. van der Walt, J. L. Schönberger, J. Nunez-Iglesias, F. Boulogne, J. D. Warner, N. Yager, E. Gouillart, T. Yu, and t. scikit-image contributors, "Scikit-image: Image processing in Python," *PeerJ*, vol. 2, e453, Jun. 2014, ISSN: 2167-8359. DOI: 10.7717/peerj.453.

[90] C. Bryant, N. R. Wheeler, F. Rubel, and R. H. French, *Kgc: Koeppen-Geiger Climatic Zones*, Dec. 2017.

[91] R. Fisher, "Statistical Methods and Scientific Induction," *Journal of the Royal Statistical Society. Series B (Methodological)*, vol. 17, no. 1, pp. 69–78, 1955, ISSN: 0035-9246.

[92] S. Wright, "Correlation and Causation," *Journal of Agricultural Research*, vol. 20, no. 7, pp. 557–585, 1921.

[93] K. Pearson, "LIII. On lines and planes of closest fit to systems of points in space," *The London, Edinburgh, and Dublin Philosophical Magazine and Journal of Science*, vol. 2, no. 11, pp. 559–572, Nov. 1901, ISSN: 1941-5982. DOI: 10.1080/14786440109462720.

[94] G. James, D. Witten, T. Hastie, and R. Tibshirani, *An Introduction to Statistical Learning: 2nd Ed., with Applications in R,* 2nd ed. 2021 edition. New York: Springer, Jul. 2021, ISBN: 978-1-07-161417-4.

[95] F. Murtagh and P. Legendre, "Ward's Hierarchical Agglomerative Clustering Method: Which Algorithms Implement Ward's Criterion?" *Journal of Classification*, vol. 31, no. 3, pp. 274–295, Oct. 2014, ISSN: 1432-1343. DOI: 10.1007/s00357-014-9161-z.

[96] G. Cumming and S. Finch, "Inference by eye: Confidence intervals and how to read pictures of data," *American Psychologist*, pp. 170–180, 2005.

[97] A. Hazra, "Using the confidence interval confidently," *Journal of Thoracic Disease*, vol. 9, no. 10, pp. 4124–4129, Oct. 2017, ISSN: 20721439, 20776624. DOI: 10.21037/jtd.2017.09.14. [Online]. Available: http://jtd.amegroups.com/article/view/16406/13455 (visited on 05/30/2022).

[98] J. Leppink, "A Pragmatic Approach to Statistical Testing and Estimation (PASTE)," *Health Professions Education*, vol. 4, no. 4, pp. 329–339, Dec. 2018, ISSN: 2452-3011. DOI: 10.1016/j.hpe.2017.12.009. [Online]. Available: https://www.sciencedirect.com/science/article/pii/S2452301117301487 (visited on 02/20/2021).

[99] F. Rubel, K. Brugger, K. Haslinger, and I. Auer, "The climate of the European Alps: Shift of very high resolution Köppen-Geiger climate zones 1800–2100," *Meteorologische Zeitschrift*, pp. 115–125, Apr. 2017, ISSN: , DOI: 10.1127/metz/2016/0816.

[100] J. W. Tukey, *Exploratory Data Analysis*. Reading, Mass. : Addison-Wesley Pub. Co., 1977, ISBN: 978-0-201-07616-5.

[101] W. S. Cleveland, "Robust Locally Weighted Regression and Smoothing Scatterplots," *Journal of the American Statistical Association*, vol. 74, no. 368, pp. 829–836, Dec. 1979, ISSN: 0162-1459. DOI: 10.1080/01621459.1979.10481038.

[102] Thorsten Trupke, "Photoluminescence and Electroluminescence Characterization in Silicon Photovoltaics," in *Photovoltaic Solar Energy*, John Wiley & Sons, Ltd, 2016, ch. 7.2, pp. 322–338, ISBN: 978-1-118-92749-6. DOI: 10.1002/9781118927496.ch30.

[103] Y. Buratti, Z. Abdullah-Vetter, A. Sowmya, T. Trupke, and Z. Hameiri, "A Deep Learning Approach for Loss-Analysis from Luminescence Images," in *2021 IEEE 48th Photovoltaic Specialists Conference (PVSC)*, Jun. 2021, pp. 0097–0100. DOI: 10.1109/PVSC43889.2021.9518512.

[104] R. Yamashita, M. Nishio, R. K. G. Do, and K. Togashi, "Convolutional neural networks: An overview and application in radiology," *Insights into Imaging*, vol. 9, no. 4, pp. 611–629, Aug. 2018, ISSN: 1869-4101. DOI: 10.1007/s13244-018-0639-9.

[105] M. Abadi, A. Agarwal, P. Barham, E. Brevdo, Z. Chen, C. Citro, G. S. Corrado, A. Davis, J. Dean, M. Devin, S. Ghemawat, I. Goodfellow, A. Harp, G. Irving, M. Isard, Y. Jia, R. Jozefowicz, L. Kaiser, M. Kudlur, J. Levenberg, D. Mané, R. Monga, S. Moore, D. Murray, C. Olah, M. Schuster, J. Shlens, B. Steiner, I. Sutskever, K. Talwar, P. Tucker, V. Vanhoucke, V. Vasudevan, F. Viégas, O. Vinyals, P. Warden, M. Wattenberg, M. Wicke, Y. Yu, and X. Zheng, *TensorFlow: Large-scale machine learning on heterogeneous systems*, Software available from tensorflow.org, 2015.

[106] K. Simonyan and A. Zisserman, "Very Deep Convolutional Networks for Large-Scale Image Recognition," *arXiv:1409.1556 [cs]*, Apr. 2015. arXiv: 1409.1556 [cs].